WORK FUNCTION FLUCTUATION ANALYSIS

OF POLYANILINE FILMS

A Thesis
Presented to
The Academic Faculty

by

Ryan M. West

In Partial Fulfillment
of the Requirements for the Degree
Doctor of Philosophy in the
School of Chemistry and Biochemistry

Georgia Institute of Technology

May 2013

WORK FUNCTION FLUCTUATION ANALYSIS

OF POLYANILINE FILMS

Approved by:

Dr. Jiří Janata, Advisor
School of Chemistry and Biochemistry
Georgia Institute of Technology

Dr. Christine Payne
School of Chemistry and Biochemistry
Georgia Institute of Technology

Dr. Mira Josowicz
School of Chemistry and Biochemistry
Georgia Institute of Technology

Dr. Stephen Harvey
School of Biology
Georgia Institute of Technology

Dr. Lawrence A. Bottomley
School of Chemistry and Biochemistry
Georgia Institute of Technology

Date Approved: March 13, 2013

ACKNOWLEDGEMENTS

Thanking the people who have given me support over the past 5 years is not an easy task. How can I repay even a percentage of the patience, dedication and love I've been fortunate enough to receive? It's difficult enough to recognize all the small things done on my behalf. I fear that I took most of these things for granted and was too busy and preoccupied to acknowledge, much less return, the generosity. So here is a small acknowledgement of those people.

I value all of my friends and family. I appreciate those who have watched me from a distance, asking year after year, "When do you graduate?" or even, "What are you studying?" I cherish those who gave me confidence when my hopes were dashed, my mind saturated and simultaneously depleted, and my experiments going nowhere. I value most those who fought the daily battles with me. Nature fights back. Research is an endurance match and the small victories (the only ones you can hope for) are few and far between.

As much as I've learned about science during this time, I've learned more about relationships. Without the following people, I would not be graduating. First, my mom and dad deserve a PhD of their own. They are amazing parents and fully supportive of my extended stay at "University Inn". They never pushed me to hurry up. They only pushed me to succeed and be happy. By not defining my goals for me they have given me definition as person. Next, I want to thank my advisors Prof. Art Janata and Dr. Mira Josowicz. I would never have started graduate school without their encouragement. I worked in their lab for many months after obtaining my undergraduate degree. I wasn't

sure what I wanted from life and was floating around with no goals. I'll never forget the words Art told me one day while trying to convince me to join his group: "If you don't make your own decisions, someone else will make them for you". Then he told me he could pay me more if I'd be a graduate student. One of those statements convinced me to apply for the graduate program. I don't know who I'd be right now without Art and Mira. Beyond being my advisors in lab, they have been second parents to me. They gave me anything I needed: sweaters, food and a place to live.

I want to give a special thanks to Dr. Janusz Kowalik for being a good friend, mentor and an inspiration. He taught me how to feel comfortable in lab and to use my imagination. I also want to thank my first chemistry teacher, Dr. Todd Deal. I'll never forget "pushing" all those electrons around. I also want to thank Amy Ingles for all we've been through together. You've been a part of my life as long as graduate school has and you've changed me just as much, if not more. Of the many friends who have been there for me, I will mention a few: foremost, my brother, Steven. You came around at the right time and I'm glad we're now best friends. A special thanks to all my friends, including Yatis Dodia, Russ Goggans, Jessica "Pal" Dodd, Jay Kirsch, Thalia Shephard, Jason Wing, Matt Di lorio, Adam Hull, Jason Pritchett, Adam Butler, Justin Peacock, Andrew Welsh, Ryan Cantor, Dr. Jennifer Steeb, Alex Jonke, Ryan Cantor and Linda van Rosmalen. There are many others, and if I've forgotten to mention your name, just know I appreciate you. This thesis is for you all.

TABLE OF CONTENTS

LIST OF FIGURES

SUMMARY

In this thesis, the development of a novel experimental technique for measuring the spontaneous, stochastic work function (WF) fluctuations of conducting polymer films, at equilibrium, is described. Polyaniline (PANI) is studied as a representative conducting polymer. This technique utilizes an insulated-gate field-effect transistor (IGFET) with PANI gate electrode (PANI-IGFET). The fluctuations of PANI WF are transduced into measurable drain current fluctuations. This is the only experimental technique capable of WF fluctuation measurements.

These fluctuations are thermally driven: the charge carriers are randomly hopping, dipoles are changing direction, and even the polymer chains themselves are constantly in motion. These microscopic events, occurring at equilibrium, can produce fluctuations in WF. Using fluctuation-dissipation theorem, kinetic information is extracted from these fluctuations. By analyzing the noise while systematically controlling the temperature, electric field and doping level, a model of WF fluctuations in PANI films is developed.

This thesis is divided into five chapters. The necessary background for noise analysis and IGFET operation is contained in chapter one. The experimental apparatus and protocol is explained in chapter two. Chapters three and four describe various results and conclude with a working hypothesis for PANI WF fluctuations. Chapter five proposes possible future directions and applications of the project.

First, the PANI-IGFET noise was compared to the noise of an identical IGFET with a platinum gate electrode (Pt-IGFET). The power spectral density (PSD) a measure of the noise variance as a function of frequency, of PANI-IGFET was found to have a higher magnitude and a different shape than the PSD of the Pt-IGFET. This indicates that

PANI is responsible for the observed noise. Second, the PANI WF noise was compared to the PANI Johnson noise. The Johnson noise gives no about the film that cannot be obtained by impedance spectroscopy. The Johnson contribution to the overall drain current noise was determined by measuring the impedance of the PANI film and was found to be negligible: the WF fluctuations are the dominant noise contribution to the drain current.

Next, both external parameters, such as temperature and electric field, and internal properties, specifically protonation state and oxidation state of the PANI film, were systematically varied. These results of these experiments suggest the most probable source of WF fluctuations as the exchange of charge carriers, or trapping/detrapping of charge carriers, near the Fermi level (E_F) of the PANI film. This spontaneous, thermally activated process causes instantaneous fluctuations of E_F and fluctuations of the "bulk" component of WF around its mean value at equilibrium.

Furthermore, coherence measurements between two PANI-IGFETs with a common PANI gate electrode suggest that the E_F fluctuations are not correlated across the bulk of the film. While at first puzzling, this "paradox" is resolved by assuming the existence of finite correlation length of WF fluctuations. This correlation length may be the result of disorder and inhomogeneity of the PANI film. Thus, this technique provides detailed information about charge-carrier dynamics in the space-charge region near the PANI-insulator interface, at equilibrium. These results have important implications for organic electronics.

Although WF fluctuation analysis is the main topic of this thesis, three other successful projects are also discussed: (1) the electropolymerization and ion-exchange

behavior of 1-pyrrolyl-10-decanephosphonic acid, (2) a "Bucky Gel" gas sensor for reversible, room temperature detection of chlorine and (3) a portable solid state scintillation calibrator for a beta microirradiator. Although the five projects in this thesis may appear to be unrelated, there are common threads that link them. First, all but the scintillation calibrator project involves organic conductors and/or semiconductors. In each of these, information is obtain about the organic electronic material *via* different experimental techniques, including; electrochemistry, spectroscopy, conductance measurements, and, of course, WF fluctuations. Second, two have applications in sensing or detection.

The most fundamental thread connecting these projects is the presence of fluctuations. Indeed, in all of chemistry, matter is grainy. These grains are the molecules, the atoms, the electrons and the nuclei. They are constantly and randomly moving. The relationships between these stochastic, microscopic events and the deterministic macroscopic measurements are the essence of chemistry. The main topic of this thesis is the study of these relationships from the opposite direction, allowing the noise to tell its own story without being buried under its own average.

CHAPTER 1

INTRODUCTION

In this chapter, the background necessary for developing the work function (WF) fluctuation technique and interpreting these fluctuations is introduced. This includes a review of WF, operation of an insulated gate field-effect transistor (IGFET), physical, chemical and electronic properties of polyaniline (PANI) and an overview of fluctuation analysis. The end of this chapter develops the motivation for the WF fluctuation analysis technique.

1.1 Work Function

WF is a fundamental thermodynamic property of all electronic conductors with practical consequences for interfaces, charge transport and the design and operation of electronic devices, including Schottky diodes, vacuum tubes and field-effect transistors [1]. It is the minimum energy required to remove an electron from the bulk of the material, and place it outside the electrostatic field at the surface [2]. In other words, WF is a measure of how strongly a conducting phase holds onto its electrons; how noble a solid conductor is. For example, the WF of gold is 5.31 – 5.47 eV, whereas copper has a WF of 4.53 – 5.10 eV [3]. Polyaniline's WF can vary between *ca.* 4 – 5 eV depending on the oxidation state, protonation level, degree of disorder and, in general, film preparation [4].

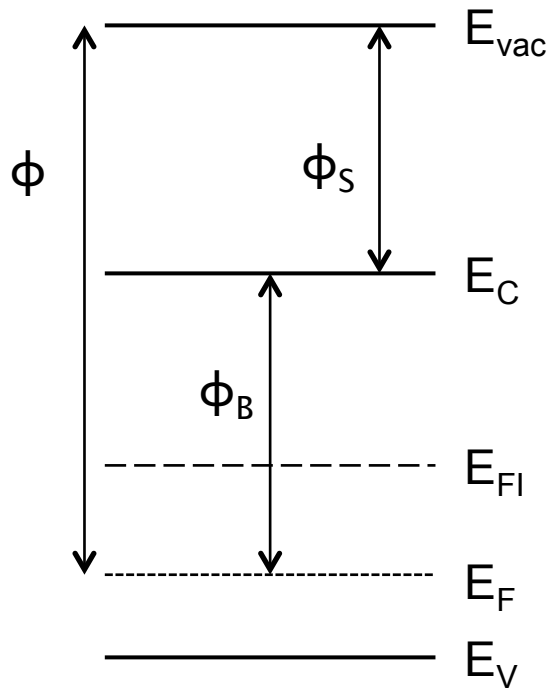

Figure 1: Energy band diagram for an arbitrary p-type semiconductor

More precisely, WF is the energy required to remove an electron from the Fermi level to the vacuum level. The energy level diagram for a p-type semiconductor is shown in figure 1, including the valance band energy, E_V, conductance band energy, E_C, mid-gap or intrinsic Fermi level, E_{FI}, vacuum level energy, E_{vac}, WF, ϕ, and Fermi energy, E_F. WF can be divided into two steps or components: The bulk component, ϕ_B, and the surface component, ϕ_S. The bulk component is the energy required to remove the electron from E_F to the surface of the material. The Fermi level is the chemical potential of the electron in the conducting and is given by the Fermi-Dirac distribution:

$$f = \frac{1}{1 + e^{(\varepsilon_i - E_F)/kT}} \tag{1}$$

where ε_i is the energy of an arbitrary state i, k is Boltzmann's constant and T is the temperature. In general, n-type doping is accompanied by an increase in E_F while p-type

doping is accompanied by a decrease of E_F. The surface component, on the other hand, depends on the particular surface through which the electron is extracted. It is important to note that a dipole exists even at an atomically clean surface: the WF of a monocrystalline material depends on the crystal face through which the electron is removed. For instance, the WF of Ag(110) is 4.37 eV, while the WF for Ag(111) is 5.31 eV [3]. This difference is due only to the surface component. Similar spatial variations in WF have been observed for amorphous conductors, including conducting polymers [5]. These differences are attributed to the disorder and inhomogeneity of the surface. Although in principle WF can be divided into two components, in practice only the total WF can be measured. Furthermore, only differences in WF can be measured.

Common methods for measuring WF include ultraviolet photoemission spectroscopy (UPS), retarding diode method and Kelvin probe (KP). Each measures the difference in WF between the sample material and a reference material. Measurement of WF using UPS is based on the photoelectric effect. In UPS, the velocity of electrons ejected by bombarding the sample with UV light is used to calculate the energy of those electrons in the material. The measurement must be carried out in ultra high vacuum (UHV) and is highly sensitive to the surface due to limited penetration depth. The retarding diode technique is similar to UPS but is based on thermionic emission. The Kelvin probe measures the WF difference between two plates of a capacitor. The two plates are composed of different materials, one being a reference, and are separated by a small air gap. When these two materials are electrically connected, electrons flow out of the material with the lower WF and into the material with higher WF, creating an electric

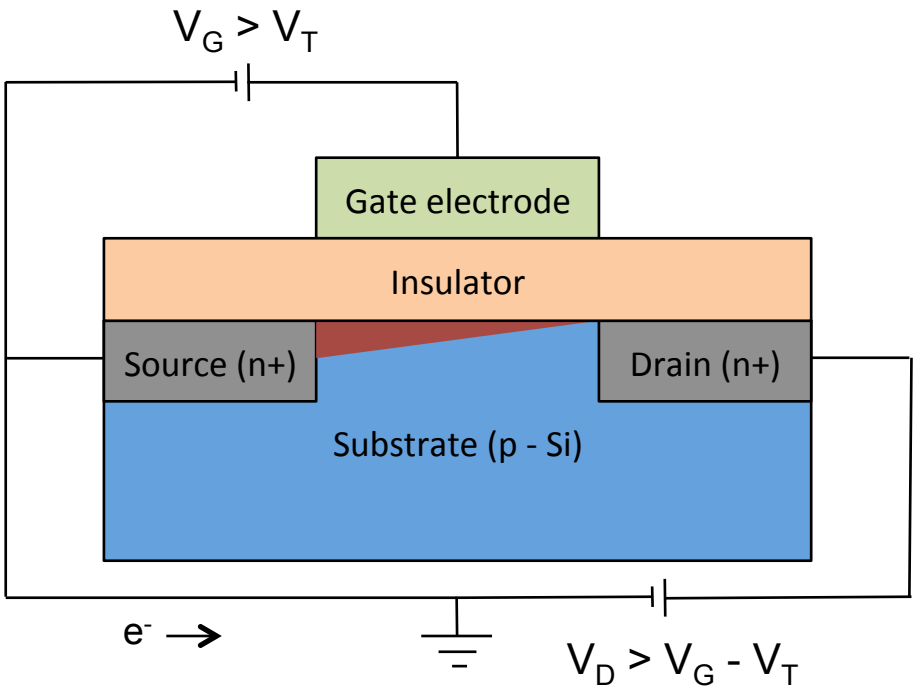

Figure 2: Schematic of n-channel, enhancement-mode IGFET

field across the gap. The two plates of the capacitor are then mechanically vibrated or oscillated, thus periodically varying the distance between them and generating an AC current. The voltage needed to null this AC current, V_{null}, is proportional to the WF difference between the two materials.

While each of these techniques offers unique advantages and disadvantages for measurement of WF, none of them are capable of measuring fluctuations of WF at equilibrium and under atmospheric conditions. On the other hand, such a measurement is possible using an IGFET. The next section will focus on the operation of an IGFET and its application as a WF measurement device.

1.2 IGFET operation

The discussion of IGFET operation in this section will be from the point of view of its role as a WF measurement device. Furthermore, the focus will be on the operation of an enhancement mode, n-channel IGFET in the saturation regime. Like the KP, the core of an IGFET is a capacitor (figure 2). Unlike for the KP, the insulator is typically an oxide such as silicon dioxide and/or silicon oxynitride. One plate of this capacitor, the substrate, is lightly doped p-type silicon while the other plate, the gate, is typically a metal such as Au or highly doped amorphous silicon. In this work, the gate will be a PANI film.

When the substrate and gate are electrically connected, electrons flow from the material with a lower WF to the other material, for instance from the substrate to the gate. This results in an electric field across the insulator. An excess of positive charge, the majority charge carrier for the p-type silicon gate, is concentrated at the substrate-insulator interface and the electronic bands bend downward, away from E_F. An excess of negative charge is formed at the PANI-insulator interface and the electronic bands bend upward, towards E_F. Note that E_F remains constant throughout the film and is the same in both substrate and gate at equilibrium. In order to flatten these bands and obtain so-called flat-band conditions, a positive voltage must be applied from the gate to the substrate. This gate voltage, V_G, essentially returns the electrons back to the substrate. The V_G necessary to do this is called the flat-band voltage, V_{FB}, and is proportional to the difference in WF of the substrate and gate. Essentially, for the IGFET, V_{FB} plays the role that V_{null} plays for the KP.

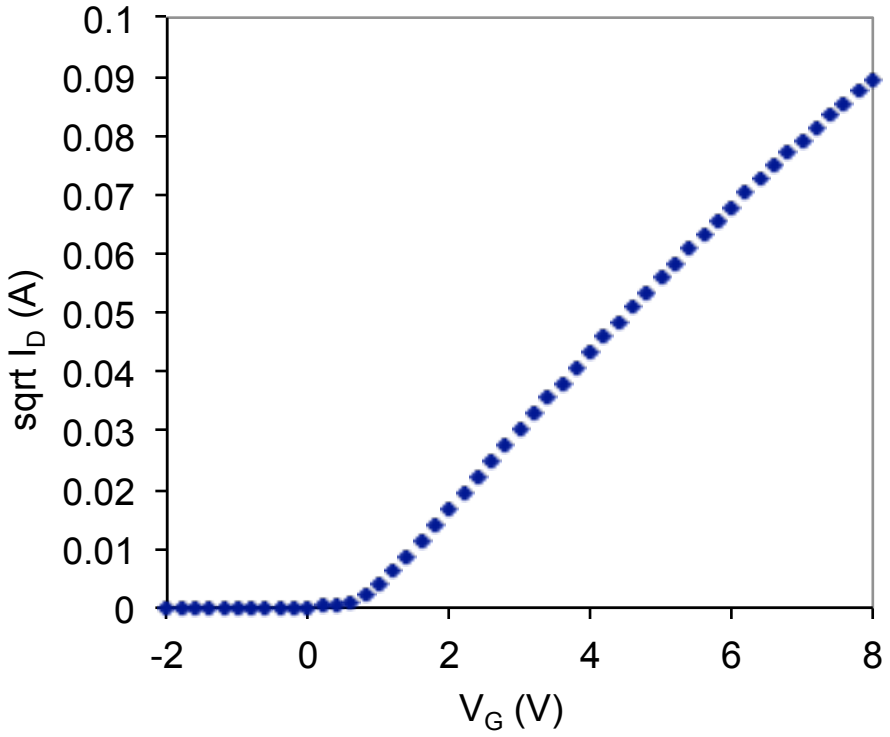

Figure 3: The square root of I_D versus V_G

Unlike the KP, the electrodes cannot oscillate. Another means must be used to interrogate the WF difference. For this, two additional electrodes are introduced: the source electrode and the drain electrode. As shown in figure 2, these electrodes are imbedded in the substrate directly below the insulator on either side of the gate. Both electrodes are n-type semiconductors and pn-junctions exist at the interface between both electrodes and the substrate. If a so-called drain voltage, V_D, is applied from drain to source and V_G is below a particular threshold, no current flows because a reverse biased pn-junction exists at the drain electrode. The square root of drain current, $\sqrt{I_D}$, versus V_G is shown in figure 3. As V_G is increased the majority charge carriers in the p-type substrate are depleted near the insulator-substrate interface. This leaves behind only

immobile negatively charged dopants. Eventually, if V_G is increased enough, an appreciable concentration of electrons accumulate near this interface, creating a thin, conducting, n-type channel. The pn-junctions no longer exist, and a drain current flows between drain and source. The V_G at which the channel is formed is called the threshold voltage, V_T. As V_G is increased beyond V_T, I_D increases. As long as V_D remains above V_G - V_T, and V_G remains above V_T, the IGFET is in the saturation regime and behaves like a variable resistor according to the following expression:

$$I_D = \frac{\mu C_0 W}{2L}(V_G - V_T)^2 \tag{2}$$

where μ is the mobility of carriers in the channel, C_0 is the capacitance of the oxide, W is the width of the gate and L is the length of the gate. These terms are constants for a given IGFET that depend on the geometry of the device, the materials from which the device is made and the fabrication process.

The threshold voltage depends on the difference in WF between the gate and the substrate according to:

$$V_T \; \alpha \; \frac{\phi_{gate} - \phi_{substrate}}{e} \tag{3}$$

where e is the charge of the electron, ϕ_{gate} and $\phi_{substrate}$ are the WF of the gate electrode and substrate, respectively. If the WF of the gate changes or fluctuates, these changes or fluctuations can be detected by measuring I_D. In this way it is possible to utilize an IGFET with PANI gate electrode to study WF fluctuations of a PANI film.

The transconductance, g_m, of an IGFET is the slope of the $I_D - V_G$ curve:

$$\left(\frac{\partial I_D}{\partial V_G}\right)_{V_D} = \frac{\mu C_0 W}{L}(V_G - V_T) = g_m \tag{4}$$

It is a measure of the amplification of the IGFET and has units of amperes per volt or Siemens. It is important to note that g_m is the negative of the partial derivate of equation (2) with respect to V_T.

$$g_m = \left(\frac{\partial I_D}{\partial V_G}\right)_{V_D} = -\left(\frac{\partial I_D}{\partial V_T}\right)_{V_D} \tag{5}$$

Therefore, g_m can be used to convert from drain current to gate voltage and threshold voltage. This will be important later on when converting drain current fluctuations into threshold voltage fluctuations since g_m can be directly measured.

The possibility of using an IGFET to measure WF fluctuations of the gate electrode has been established. The next section will deal with how to analyze these fluctuations to obtain information about the PANI film.

1.3 Fluctuation Analysis

In general, any stationary signal is composed of a mean value and fluctuations around that value. A stationary signal is one with statistical properties that do not vary in time:

$$\langle x(t) \rangle = \langle x \rangle \tag{6}$$

where, $x(t)$ is the signal and the brackets denote the time or ensemble average. For an ergodic system, the time and ensemble averages are the same. In order for information to be obtained from fluctuations, the system responsible for the fluctuations must be stationary and ergodic [6].

The IGFET drain current is the sum of two components:

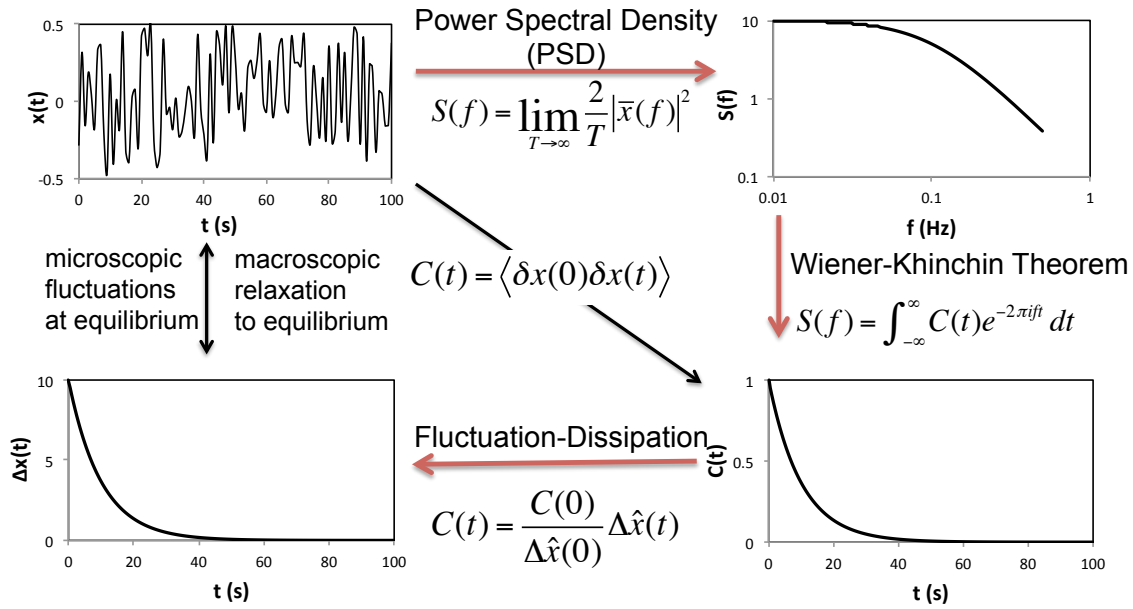

Figure 4: Flow-chart for fluctuation analysis

$$I_D = \langle I \rangle + i(t) \qquad (7)$$

where the DC current, $\langle I \rangle$, is given by the I_D-V_G equation in the saturation regime (see the previous section) and a time dependent fluctuating component, *i(t)*, or drain current noise. In this thesis, information will be obtained by analyzing the noise. While these fluctuations can have many possible sources, including undesirable ones such as electromagnetic interference and electronics noise, the goal will be to operate the IGFET under such conditions that this noise is dominated by WF fluctuations of the PANI gate electrode.

Analysis of this noise will be aided by use of the power spectral density, PSD, which is a measure of the frequency content of a stationary noise signal [7]. Figure 4 shows an overview of the noise analysis process. Much like a prism decomposes a light beam into its component wavelengths and intensities, the PSD decomposes the noisy time

segment into its frequency components. The PSD, $S(f)$, of a stationary signal is given by:

$$S(f) = \lim_{T\to\infty} \frac{1}{T} |\bar{x}(f)|^2 \tag{8}$$

where T is the length of the measurement and $\bar{x}(f)$ is Fourier transform of $x(t)$. The Fourier transform is given by:

$$\bar{x}(f) = \int_{-\infty}^{\infty} x(t) e^{-i\omega t} dt \tag{9}$$

Here, $x(t)$ is the inverse Fourier transform of $\bar{x}(f)$, $i = \sqrt{-1}$ and the angular frequency ω is 2πf. The ease of computing the Fourier transform using digital filters, *i.e.* the fast Fourier Transform (FFT), makes the PSD a powerful and practical tool for studying fluctuating signals.

Although the PSD will be used to analyze the WF fluctuations in this thesis there is another tool for studying fluctuating signals: the time correlation function. For an arbitrary fluctuating signal, $x(t)$, the time correlation function, $C_x(\Delta t)$, is given by:

$$C_x(\Delta t) = \langle \delta x(t) \delta x(t + \Delta t) \rangle = \int_{-\infty}^{\infty} \delta x(t) \delta x(t + \Delta t) dt \tag{10}$$

where $\delta x(t) = x(t) - \langle x \rangle$ is the instantaneous deviation of $x(t)$ from the average $\langle x \rangle$. The time correlation function provides information about the correlations of a noisy signal at different time differences, *Δt*. A signal with quick fluctuations will only be correlated at short times, whereas slower fluctuations are correlated over longer times. When $\Delta t = 0$, $C_x(\Delta t)$ equals the variance of the noise:

$$C_x(\Delta t) = \langle \delta x(t) \delta x(t) \rangle = \langle (\delta x)^2 \rangle \tag{11}$$

On the other hand, when $\Delta t \to \infty$, $C_x(\Delta t) \to 0$: the correlations regress to zero. The functional form of $C_x(\Delta t)$ depends on the source of the fluctuations and is typically exponential.

The PSD and the time correlation function are related to each other through the Weiner-Khinchin Theorem, which states that the PSD of a stationary signal is the Fourier transform of the time correlation function of that same signal [8]:

$$S_x(f) = \int_{-\infty}^{\infty} C_x(\Delta t) e^{-i\omega\Delta t} d(\Delta t) \tag{12}$$

The time correlation function and the PSD contain the same information but represent that information in the time and frequency domains, respectively.

The final step of extracting information from the PSD is provided by the Fluctuation-Dissipation theorem. The Fluctuation-Dissipation (F-D) theorem states that the response of a system to an applied force, *i.e.* the way it relaxes to equilibrium, is the same as its response to a spontaneous fluctuation. While there are a number of ways the F-D theorem can be stated mathematically, one of the simplest is:

$$D = kTM \tag{13}$$

where *D* is the magnitude of the fluctuations, *k* is Boltzmann's constant, *T* is temperature and *M* is the dissipative force that characterizes the relaxation, *e.g.* resistance, viscosity, etc. Another way of expressing F-D is with Onsager's Regression Hypothesis. For a system with a relaxation function, $\Delta\hat{x}(t)$, given by

$$\Delta\hat{x}(t) = \hat{x}(t) - \langle x \rangle \tag{14}$$

where $\hat{x}(t)$ is the non-equilibrium average of $x(t)$, the time correlation function at equilibrium is given by:

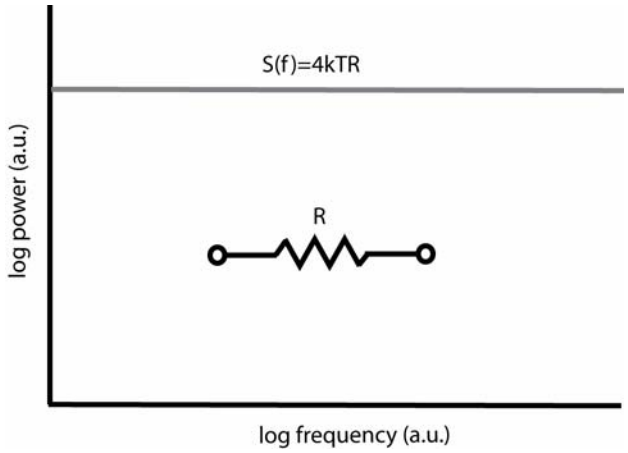

Figure 5: PSD of the Johnson noise of a resistor

$$C(t) = \frac{C(0)}{\Delta\hat{x}(0)}\Delta\hat{x}(t) \tag{15}$$

Notice that the functional form for both is the same but the (constant) prefactor differs.

The concept of noise analysis can be introduced by considering the thermal noise of a resistor. If a low noise, high input impedance voltmeter is connected to the terminals of a resistor, the measured voltage, *V(t)*, will fluctuate around zero. Assuming the resistor and leads are properly shielded, this noise is caused by thermal fluctuations of charge-carrier density within the resistor.

The PSD of the thermal fluctuations in the resistor is flat (figure 5). Noise with a flat PSD is often called white noise in analogy to the spectrum of white light. In 1926, J. B. Johnson was the first to measure this thermal noise [7]. The magnitude of this PSD, known as Johnson noise, is given by the Nyquist equation:

$$S_V(f) = 4kTZ_{re}(f) \tag{16}$$

Here, k is Boltzman's constant, T is temperature, and $Z_{re}(f)$ is the real component of the impedance. For a resistor, $Z_{re}(f)$ is just the resistance and has no frequency dependence.

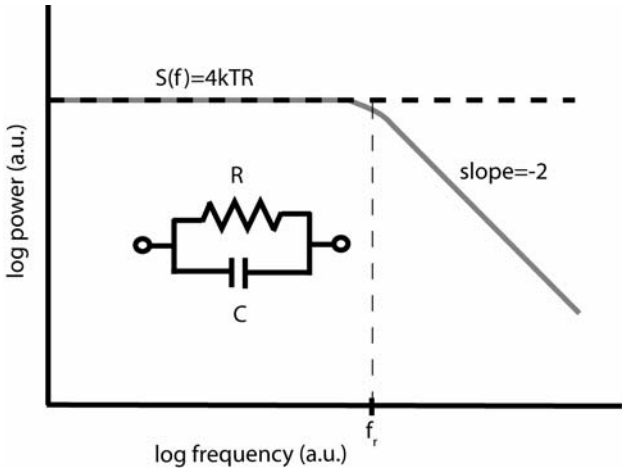

Figure 6: PSD of the Johnson noise of a RC circuit

In deriving this equation, Nyquist separated the real resistor into an ideal (noiseless) resistor in series with a fluctuating AC voltage source, *e(t)*. In principle, the Johnson noise of any circuit can be determined by replacing each real resistor in the circuit with an ideal resistor in series with a fluctuating voltage source with a PSD given by the Nyquist equation. For instance, a parallel RC circuit has an output voltage in the frequency domain given by

$$\bar{V}(f) = \frac{\bar{e}(f)}{1 + i\omega\tau} \tag{17}$$

where $\bar{e}(f)$ is the Fourier transform of the randomly fluctuating white noise source, $i = \sqrt{-1}$, and $\tau = RC$ is the time constant. The PSD is obtained by taking the square modulus of both sides, multiplying through by *1/T* and taking the limit of large T:

$$S_V(f) = \frac{S_e(f)}{1 + (\omega\tau)^2} \tag{18}$$

The PSD is flat at low frequencies and decreases as f^2 at high frequencies (figure 6). Note that the PSD is plotted in a log-log format. This spectral shape is characteristic of

noise of a Lorentzian process with an exponential time correlation function. From this plot, the values of R, C, and the time constant of the circuit can be determined. Note that capacitance C is a noiseless element and enters into equation only as a time constant RC. R is given by the magnitude of the low frequency spectral density according to the Nyquist equation. The time constant is given by the corner frequency, f_τ , according to

$$f_\tau = \frac{1}{2\pi\tau} \tag{19}$$

The capacitance can be determined from $\tau = RC$. Of course, this same information could have been obtained by other methods such as impedance spectroscopy but here the system has not been perturbed at all during the measurement: the system is at true thermodynamic equilibrium.

To use noise analysis to investigate a chemical or electrochemical system we could represent the system of interest with an equivalent electrical circuit. Equivalent electrical circuits are widely used in electrochemical impedance spectroscopy as a way of fitting the measured frequency response of a system to the frequency response of a circuit representing the system. As a simple example, consider a platinum electrode immersed in an electrolyte solution containing a redox active compound [9]. If we ignore the reference electrode and solution resistance, a parallel RC circuit can represent the electrode-solution interface. Here, the resistance represents the charge transfer resistance, R_{CT}, and the capacitance represents the double-layer capacitance, C_{DL}. The charge-transfer resistance is related to the exchange current, i_0, at equilibrium by

$$R_{CT} = \frac{RT}{nFi_0} \tag{20}$$

where R is the gas constant, T is the temperature, n is the number of electrons transferred per reaction, and F is Faraday's constant. From this analysis, the double layer capacitance, exchange current and time-constant of the reaction can be determined without perturbing the system during measurement. If the equilibrium constant can be determined by measurement of open cell potential then the time constant can be used to determine values of forward and backward rate constants.

In principle, this approach can be used to study any system for which thermal fluctuations can be measured, including WF fluctuations. The difficult part is assigning an equivalent circuit that not only accurately models the noise but also one that can be understood in terms of physical processes responsible for the fluctuations. There have been many equivalent circuits of conducting polymers developed but none of them is universal and the particular circuit used often depends on the specific conducting polymer and application. Furthermore, none of these represents the fluctuations of WF. It is also important to note that PANI, like all conductors, possesses a Johnson noise. This Johnson noise is distinct from the WF fluctuations. The equivalent circuit method is not the only way to understand and analyze noise spectra. As a matter of fact, it may be more intuitive to look at the specific chemical or kinetic sources of noise.

To derive the shape of the PSD from a chemical perspective, consider a simple two-state model [7]:

$$A \underset{k_b}{\overset{k_f}{\rightleftarrows}} B \tag{21}$$

where A and B are the reactant and product, respectively, k_f is the forward rate constant, and k_b is the backwards rate-constant. The total number of particles, N_T, is constant so that

$$N_T = N_A(t) + N_B(t) \tag{22}$$

where $N_A(t)$ and $N_B(t)$ are the total number of A and B particles at any given time, respectively. The number of B particles changes in time according to the differential equation:

$$\frac{dB}{dt} = k_f N_A - k_b N_B = k_f(N_T - N_B) - k_b N_B \tag{23}$$

This equation describes the average time dependence of N_A, not the instantaneous behavior. Integration of this equation between t and $t+\Delta t$ gives the change in the average value of N_B in the time interval Δt:

$$N_B(t + \Delta t) = N_B(t)e^{-\Delta t/\tau} + k_f N_T \tau\left(1 - e^{-\Delta t/\tau}\right) \tag{24}$$

where the time constant, τ, is given by $1/(k_f+k_b)$. When Δt goes to infinity, N_B goes to $\tau k_f N_T$, which is the average thermodynamic value at long times. Rearrangement leads to:

$$N_B(t + \Delta t) - k_f N_T \tau = \left(N_B(t) + k_f N_T \tau\right)e^{-\Delta t/\tau} \tag{25}$$

The correlation function, $C_B(\Delta t)$, is given by multiplication of both sides by $\left(N_B(t) + k_f N_T \tau\right)$:

$$C_B(\Delta t) = C(0)e^{-\Delta t/\tau} \tag{26}$$

where $C_B(0)$ is the variance of the number of B particles. The variance, $C(0)$, can be determined by examining the statistics describing the population of total particles. The average number of A particles, $\langle N_A \rangle$, is given by:

$$\langle N_A \rangle = pN_T \tag{27}$$

and the average number of *B* particles, $\langle N_B \rangle$, is given by:

$$\langle N_B \rangle = qN_T \tag{28}$$

where p and q are the fractions of *A* and *B* particles, respectively. Since the number of sites is constant

$$p + q = 1 \tag{29}$$

The probability of there being exactly N_B particles is given by the Bernoulli distribution:

$$P_N(N_B) = \frac{N!}{N_B!\,(N - N_B)!} q^{N_B} p^{N_T - N_B} \tag{30}$$

The variance is of this distribution is given by:

$$\sigma^2 = N_T pq \tag{31}$$

The probabilities in terms of the rate constants are:

$$p = \frac{k_f}{k_f + k_b} = k_f \tau \tag{32}$$

$$q = \frac{k_b}{k_f + k_b} = k_b \tau \tag{33}$$

Plugging these last three equations into the correlation function gives:

$$C_B(\Delta t) = N_T k_f k_b \tau^2 e^{-\Delta t/\tau} \tag{34}$$

The PSD can be derived directly from the time correlation function by the Wiener-Khinchin theorem. Taking the Fourier transform of $C_B(\Delta t)$ gives:

$$S_B(f) = \frac{4N_T k_f k_b \tau}{1 + (\omega\tau)^2} \tag{35}$$

The similarity to the PSD derived earlier for the parallel RC circuit: both are of the Lorentzian-type. In this case the physical origin of the noise source is a bit more obvious.

The magnitude of the random fluctuations is a function of the total number of particles and the forward and backward rate constants. A simple model has been used to derive the noise spectrum in a more physically intuitive way. In general, a Lorentzian PSD of noise indicates that the underlying process is governed by exponential kinetics.

It is important to note that a noise measurement only gives statistical information about the system being studied, *e.g.* the time constant of a chemical reaction or an electrical circuit. It does not give information about the rate of the individual reactions, *i.e.* how long the transition from *A* to *B* takes, in other words, how long it takes to cross the activation barrier. This time is much shorter that the rate of reaction and is assumed instantaneous.

1.4 Polyaniline

Since the discovery, in 1977, that doping the intrinsically insulating polymer polyacetylene increases its conductivity up to eight orders of magnitude [10], conducting polymers, such as polypyrrole, polythiophene and polyaniline, have been an area of active research with applications in electronic devices [11], chemical sensors [12], mechanical actuators [13], etc. Unlike in inorganic semiconductors, the charges formed when conducting polymer films are doped are localized polarons: a cation radical associated with a geometry relaxation [10].

Polyaniline is unique amongst the conducting polymers in that it can be doped by changing its oxidation state and protonation level [14]. Polyaniline exists in three oxidation states: leucoemeraldine, emeraldine and pernigranaline. Each of these states

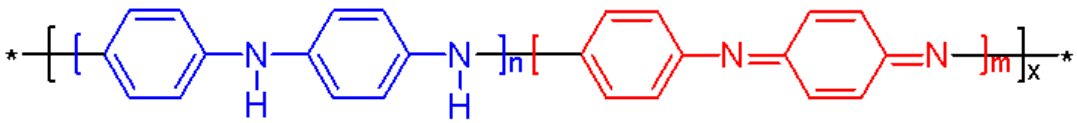

Figure 7: Chemical structure of emeraldine base (EB-PANI)

exists in the unprotonated base form or the protonated salt form. The emeraldine form is the most interesting because upon protonation it becomes highly conducting (figure 7, m = n). Upon exposure to an acidic medium, *e.g.* 1 M HCl, the imine nitrogens are protonated followed by an internal, spontaneous redox reaction creating two radical cations, *i.e.* polarons. This is accompanied by an increase in conductivity and a change in color from dark blue to green.

Like other conducting/semiconducting polymers, disorder and inhomogeneity play a large a role in the conductivity and electronic properties. Typically, a large amount of disorder causes localization of the polarons [15]. Because disorder usually increases with decreasing doping level, charge transport in a lightly doped PANI film is dominated by hopping between localized electronic states, or traps. On the other hand, band-like conductivity through delocalized extended electronic bands is possible in highly doped films. Between these two extremes, the highly protonated, ordered segments of the film tend to phase segregate from the disordered, lightly protonated areas, leading to islands of highly conducting, ordered regions separated by amorphous, resistive regions [16]. The bulk conductivity is still limited by hopping between the ordered regions unless a percolation path is formed, connecting the conducting regions from one end of the material to the other.

1.5 Motivation

Here we introduce a new and unique method for measurement of equilibrium and dynamic properties of conducting polymers under atmospheric conditions. Our approach is based on fluctuation analysis of the drain current noise in an IGFET in which the gate conductor is the material under study. A similar approach was used for fluctuation analysis of ion-selective field-effect transistors [9a], corrosion of silicon oxynitride [17] and potassium ferro/ferricyanide redox system on platinum disc microelectrodes [9b]. The fundamental difference between the previous IGFET fluctuation analysis and this work is that WF fluctuations are responsible for the drain current fluctuations, not Johnson noise.

For the first time, a technique for measuring WF fluctuations of an organic semiconductor is demonstrated. These fluctuations are stochastic, spontaneous and the outcome of thermal energy. Because of the important role of the WF in characterization and applications of organic semiconductors, this technique provides a unique opportunity to measure the dynamic properties of thin films at true equilibrium. Analysis of WF fluctuations can provide new insight about these films, which is complementary to other techniques such as conductance, impedance, UV-Vis absorption spectroscopy, etc.

Much of this thesis is devoted to altering the equilibrium state of the PANI film by changing the electric field, the temperature, the protonation state and the oxidation state. Each of these parameters affects the WF fluctuations. By examining these correlations, a model is proposed for the origin of WF fluctuations in PANI films.

CHAPTER 2

EXPERIMENTAL

This chapter describes the experimental set-up for the noise measurements including the IGFET circuit, electromagnetic shielding, low-noise amplification, analog-to-digital conversion and the details of the power spectral density calculations. Also included in this chapter is information pertaining to the chemicals, film casting protocol and the IGFET chips.

2.1 IGFET Noise Measurement

A diagram of the circuit used for IGFET operation and drain current measurement along with a photograph of the experimental set-up is shown in figure 8a and 8b, respectively. A 12 V lead-acid battery supplied the gate voltage. This voltage source was applied across a variable 10 kΩ resistor followed by a low-pass filter composed of a 200 kΩ resistor and a 1 μF capacitor in parallel to give a low-pass cut-off frequency, f_{LP}, of 1.59 Hz. The variable 10 kΩ resistor was used as a voltage divider to control the voltage applied to the gate electrodes. The low-pass filter removed any high frequency noise (above 1.59 Hz) noise that was generated by the battery and, in particular, the variable 10 kΩ resistor, ensuring a clean gate voltage source. A 6 V lead-acid battery provided the drain voltage, which was divided between the IGFET channel and a high precision, low

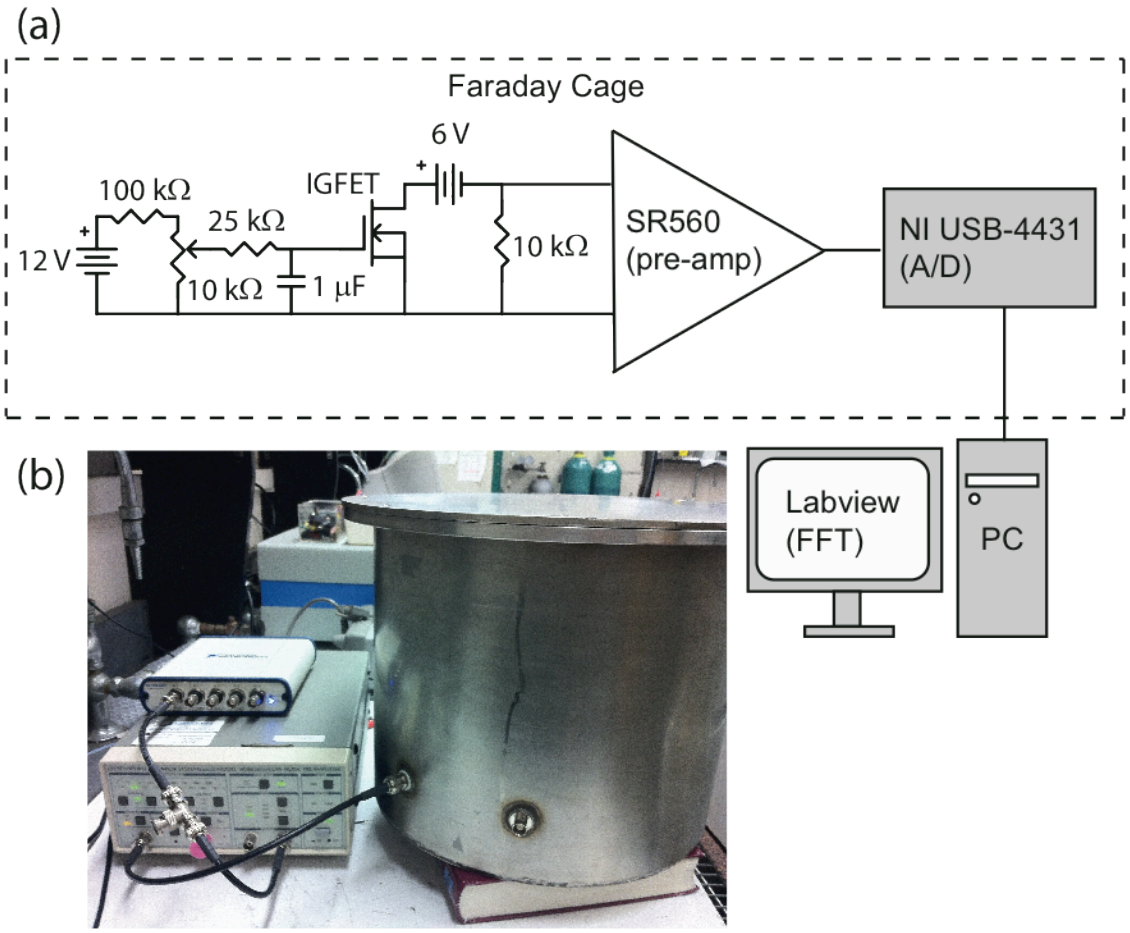

Figure 8: (a) Circuit used for noise measurements and (b) Photograph of measurement set-up

noise 10 kΩ (0.01%) measurement resistor (Mills MR102T 0829). A low noise resistor has negligible noise in excess to the intrinsic Johnson noise. Excess noise in this resistor could mask the signal, *i.e.* the WF fluctuations of the PANI film and, therefore, must be avoided. Batteries were used as voltage sources to avoid AC line noise, which could also mask the signal. Electromagnetic shielding was provided by a 1/4" thick stainless steel, grounded faraday cage. Bayonet Neill–Concelman (BNC) connectors provided outputs.

The drain current was measured across the measurement resistor and AC coupled into a low-noise pre-amplifier (SR560) and amplified 1000x. The AC coupling removed all

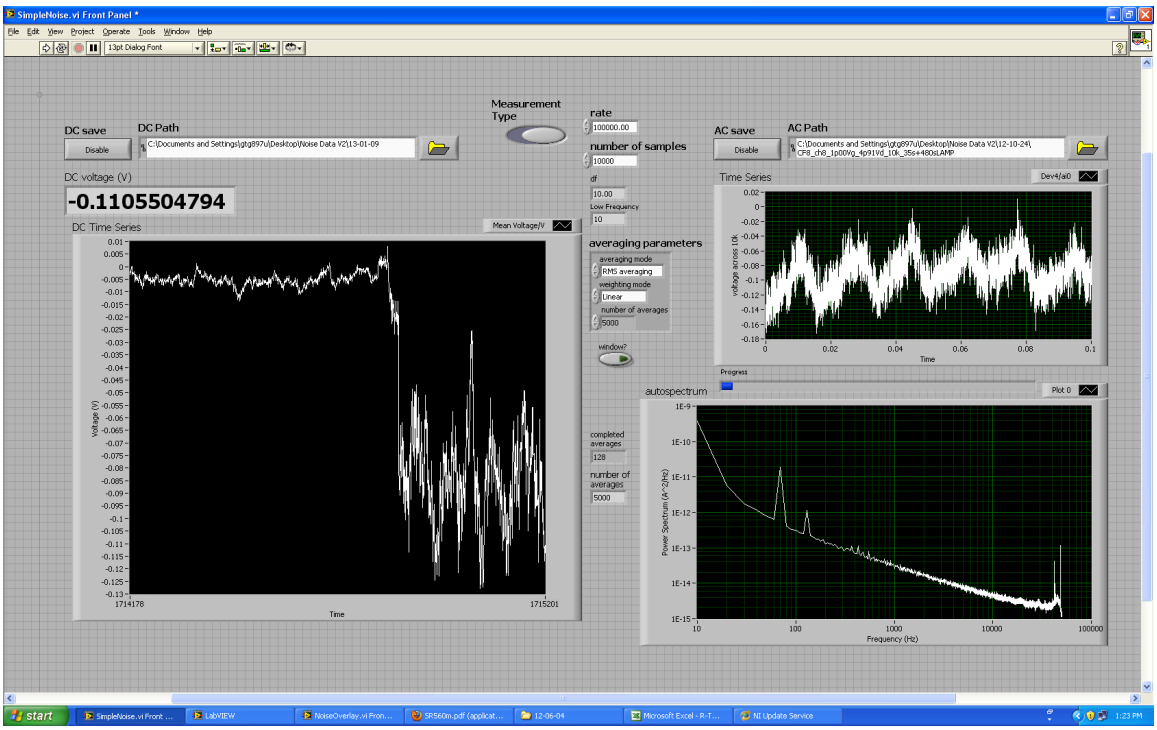

Figure 9: Screenshot of Labview program used for noise measurements

frequencies below 0.03 Hz, thus removing the DC component of the drain current. The amplifier was AC powered, not battery powered, after it was determined that this did not introduced significant noise. The output was then fed into a 24-bit data acquisition card (National Instruments USB-4431) at a sampling rate of up to 102.4 kS/s. Antialiasing filters were automatically employed using a method of analog-to-digital conversion known as sigma-delta, which utilizes built-in antialiasing filters that automatically adjust to the sampling frequency.

A Labview program controlled the number of data points, sample rate and averaging. A screen shot is shown in figure 9. This program has two functionalities: (1) measuring the DC signal to ensure the system is at equilibrium and (2) computing the PSD of the AC coupled signal. A flowchart of the basic measurement protocol for fluctuation

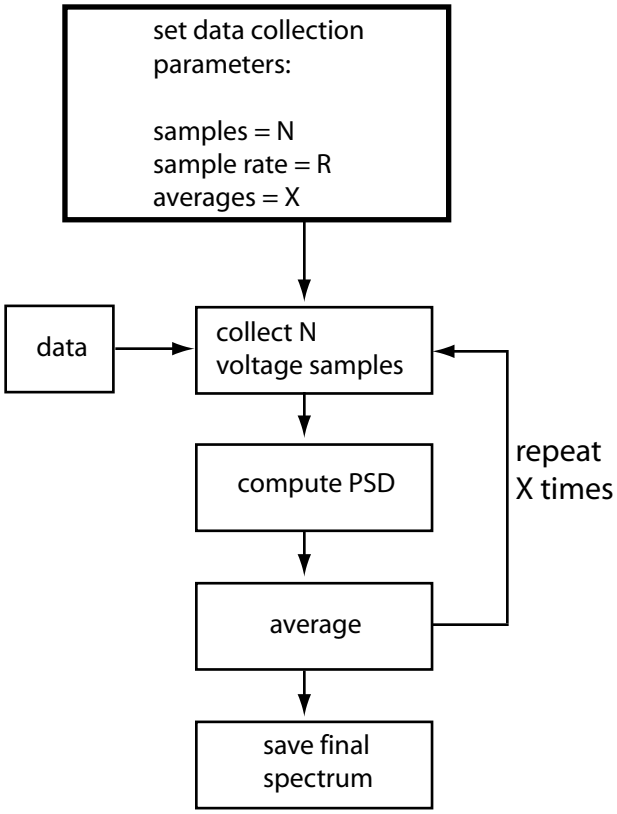

Figure 10: Flow-chart of experimental routine

measurements is shown in figure 10. Typically, spectral densities were computed from 100 ms segments of data at a sampling rate of 100 kS/s (10,000 data points) to give a frequency bandwidth of 10 – 100,000 Hz. Each spectrum was averaged 5000 times for increased resolution.

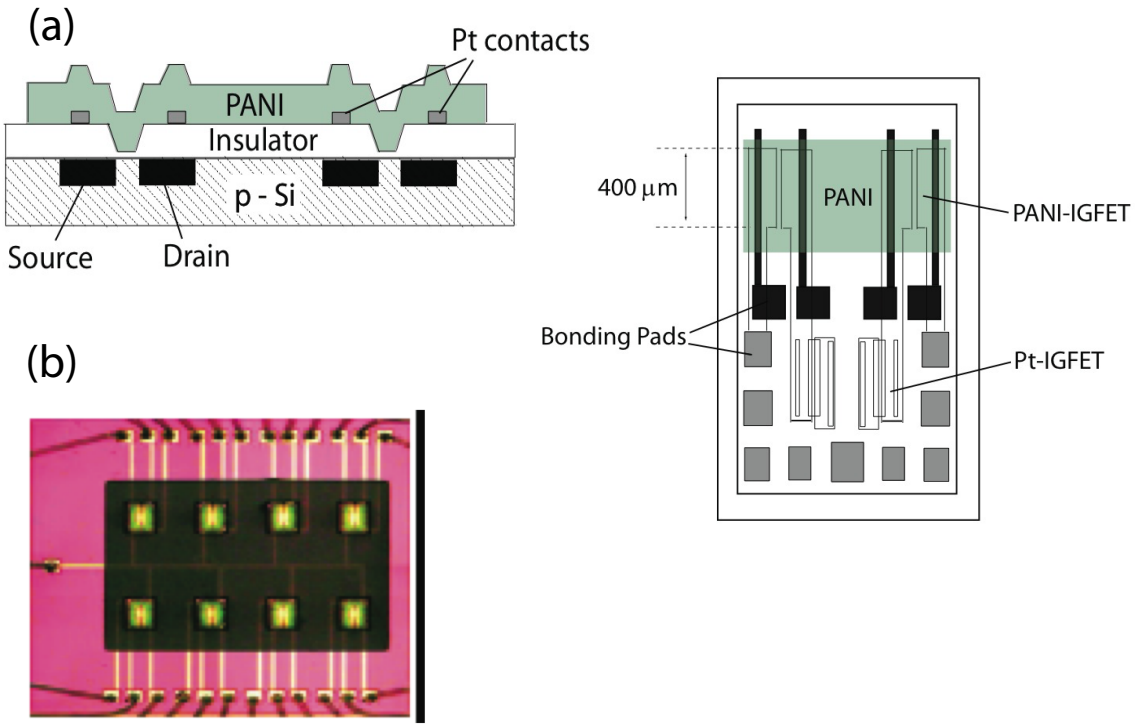

Figure 11: (a) Schematic of Utah chip and (b) Picture of GT-03 chip

2.2 IGFET Chips

Two different IGFET chips were used in this work. All IGFETs were n-channel, enhancement mode devices and all measurements were conducted in the saturation regime. The first chip, the "Utah" chip, contains four IGFET channels [18]. Figure 11a shows a top view and cross-section of the chip. The bottom two IGEFTs have platinum metal gate electrodes (Pt-IGFET) while the top two have open gate insulators with Pt metal contacts on either side of each channel over which a continuous PANI film was cast. The films were doped by exposure to the vapor of 1 M HCl. The second chip, GT-

03, contains eight IGFETs with gold metal contacts on either side of each channel (figure 11b). PANI films were drop cast on each channel individually. Fabrication of the GT-03 chips can be found in ref [19]. The chips were cleaned with isopropanol and mounted on 28-pin headers with silver epoxy and wire-bonded for electrical contact. Before drop-casting PANI, the chips were plasma cleaned for 1 minute and placed in the oven at 150 $^{\circ}$C overnight.

Before noise measurements, PANI-IGFET chip characterization (I_D-V_G and leakage tests) was carried out on an HP 4155A semiconductor parameter analyzer. All chips had I_D-V_G curves typical of standard MOSFET equations with well-defined V_T. The gate-to-substrate resistances were also measured and confirmed there was no leakage current. Leakage current from gate to substrate would generate an additional Johnson noise in the drain current and interfere with the WF noise measurement.

2.3 Chemicals and Film Preparation

Polyaniline emeraldine base (EB-PANI) (Aldrich, M_W *ca.* 20,000) was purified by first stirring in NaOH overnight to fully deprotonate the polymer, then filtered and washed with methanol and water. The resulting blue powder was dried overnight in air and dissolved in DMF and then filtered through a 0.2 μm syringe filter. Dimethylamine (DMA) (Aldrich, anhydrous 99+%), triphenylsulfonium trifluoromethanesulfonate (PhT) (Aldrich), *N,N*-dimethylamine (DMF) (Aldrich, 99.9+% HPLC grade), Ammonia (NH_3) (Airgas, 5% in air), and air (Airgas, ultra zero grade) were used as received.

The PANI-PhT (1:10 by weight) solution was prepared by combining 8 mg EB-PANI and 80 mg PhT in 1 mL DMF. The solution was kept in the dark and stirred overnight. Films were drop-cast on the open gate of the GT-03 IGFET and allowed to dry overnight in a desiccator, in the dark. UV-dosing of the films was carried out by exposure to a 5 W deuterium lamp (Hamamatsu Photonics K. K., Japan). Secondary doping of HCl doped films on the Utah chips, by either NH_3 or DMA, was carried out by mounting the IGFET in a flow cell, which was filled with the gas mixture and then sealed. All measurements were carried out without flow. Gas mixing was performed using an Environics S4000.

CHAPTER 3

ELECTRIC FIELD AND TEMPERATURE DEPENDENCE

In this chapter, it is shown that PANI WF fluctuations are in excess to all other noise sources present in the measurement set-up. Additionally, the shape of this noise will be examined, coherence of the noise between two IGFET channels will be interpreted and the field and temperature dependence will be evaluated.

3.1 Isolating PANI WF Fluctuations

A typical PSD of PANI-IGFET drain current noise is shown in Figure 12a (green curve). This particular PSD was measured on a Utah chip. The inset in Figure 12 shows a 100 ms time segment of drain current noise from which the PSD was calculated. The AC coupling into the preamplifier has already removed the DC component of this signal. It is apparent that this signal is random. But the PSD of this signal (green curve) provides insight into the underlying process. In order to determine if this is WF noise of the PANI gate, a comparison to the PSD of the background is necessary.

The intrinsic noise of the 10 kΩ measurement resistor was measured at zero current (blue curve). This resistor has a Johnson noise give by the Nyquist equation (see chapter 1). According to the Nyquist equation, the Johnson noise for an ideal 10 kΩ resistor is white with a magnitude of $1.656\times10^{-24}\ A^2/Hz$. Ohm's law was used to convert the voltage fluctuations across the resistor to current fluctuations for comparison

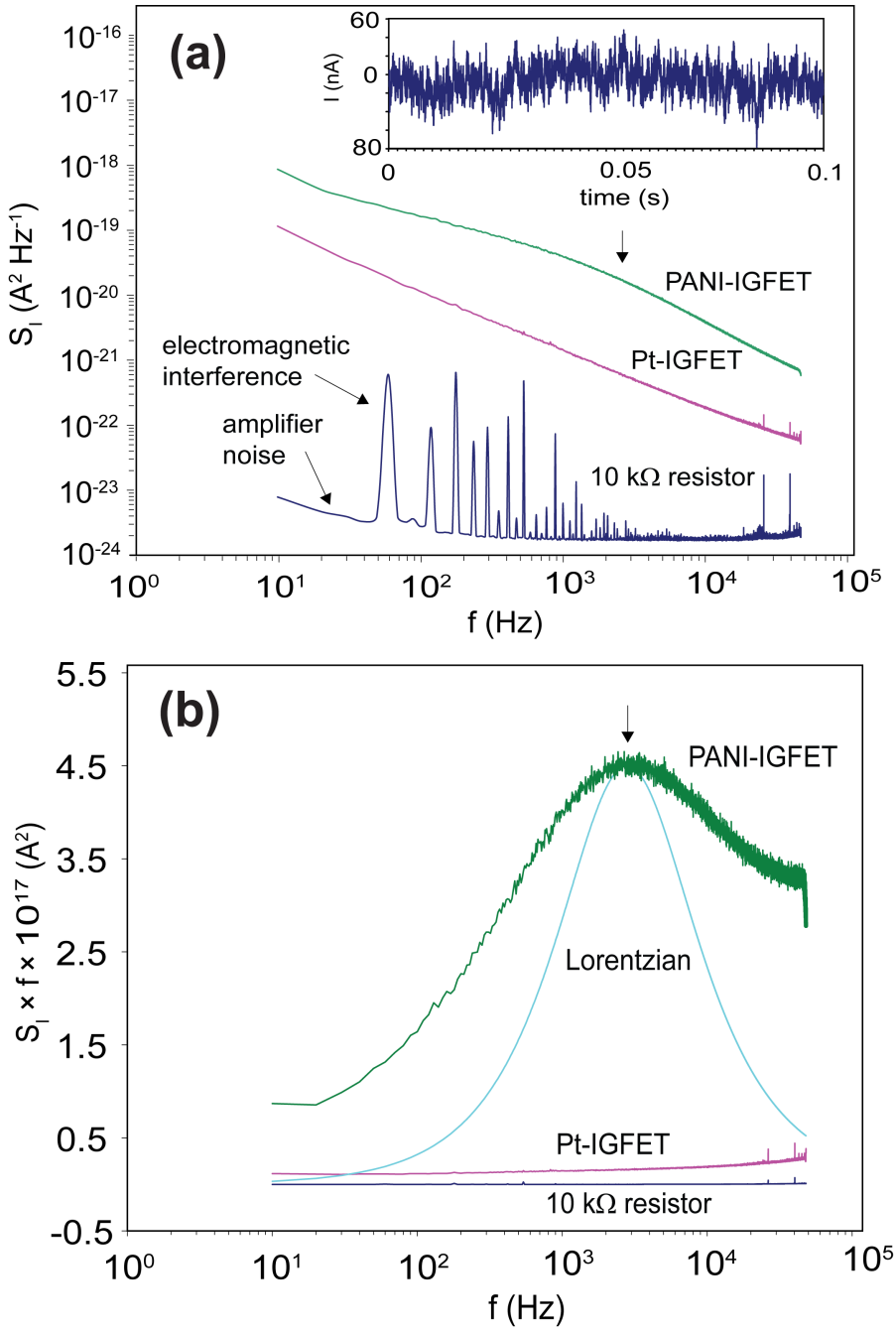

Figure 12: PSD of drain-current fluctuations for PANI-IGFET (green) and Pt-IGFET (red). Both (a) and (b) show the same data in different representations. The arrow around 3000 Hz points to the average corner frequency. The Inset in (a) is one segment of the raw time record collected over 100 ms interval. 5000 of such segments were collected for Fourier analysis. For comparison, equivalent Nyquist noise from the 10 kΩ resistor is presented on the same scale (dark blue). The spikes are due to line noise and the slight upward slope at low frequencies is caused by amplifier noise. The light blue curve in (b) is a theoretical Lorentzian.

to the PANI-IGFET noise. The measured noise baseline above ~1000 Hz is in agreement with this value. In addition to the Johnson noise, two other contributions are present. The sharp spikes are caused by electromagnetic interference (EMI), which includes the 60 Hz noise from the power lines and noises from various electronics in the lab. Note that these noises have sources that oscillate at a particular frequency. These oscillating voltages enter the signal by capacitive coupling through the Faraday cage and coaxial cables. Without the Faraday cage, the contribution from these noise sources is much higher. The increase of the noise floor at low frequencies is called *1/f* noise, or flicker noise, and is given by:

$$S(f) = \frac{A}{f^{\propto}} \tag{36}$$

where A is the magnitude, f is the frequency and α is a constant typically close to one. This is a common type of noise produced when current is flows through a conductor. It is in excess to the Nyquist noise. The values of A and α depend on the applied voltage, current and material from which the conductor is made. As already mentioned, the 10 kΩ resistor is a low noise resistor that does not produce excess flicker noise: the flicker noise here originates in the preamplifier.

Next, the noise of the IGFET was measured. Using the Pt-IGFET on the same chip and under the same operating conditions, the drain current noise was measured and the PSD was computed (pink curve). The PSD is dominated by flicker noise. This is expected for an IGFET. The flicker noise originates in resistance fluctuations of the channel, which induce current fluctuations [20]. As can be seen in figure 12, the PANI-IGFET noise is *ca.* one order of magnitude above this channel noise and has a slightly

different shape. There is broad shoulder in the PANI-IGFET PSD that is not present for the Pt-IGFET PSD.

The same data is shown in figure 12b except that PSD has been multiplied by the frequency. In this representation the corner frequency is easily identified as a peak. The arrows in both representations point to the corner frequency at ~3000 Hz. This spectral shape is characteristic of a kinetic process with smeared exponential relaxation. As such it could not be fit by a single Lorentzian (light blue curve in figure 12). However, it retains a characteristic Lorentzian shape. The shape of the noise PSD will be discussed below.

It has been determined that the drain current noise of the PANI-IGFET is in excess to all other noise sources present in the measurement set-up. This does not necessarily mean that these are WF fluctuations. Because PANI is a conductor it has Johnson noise that contributes to gate voltage fluctuations. In order to determine the extent of this contribution, the equivalent drain current spectral density, $S_{I,Ny}$, was calculated according to

$$S_{I,Ny} = 4kTZ_{re}(f)g_m^2 \qquad (37)$$

In order to display the two spectral densities on the same scale, the Nyquist noise was converted to drain current noise using the transconductance, g_m. The impedance was measured from the PANI gate to the source (*i.e.* to the ground) with a DC bias of 1.5 V and AC amplitude of 10 mV. This DC bias corresponds to the gate voltage applied during the noise measurements. As seen in figure 13, the Johnson component is negligible. The real component of impedance, Z_{re}, was also measured independently between the two Pt gate contacts at the top of the gate. The noise contribution calculated from this

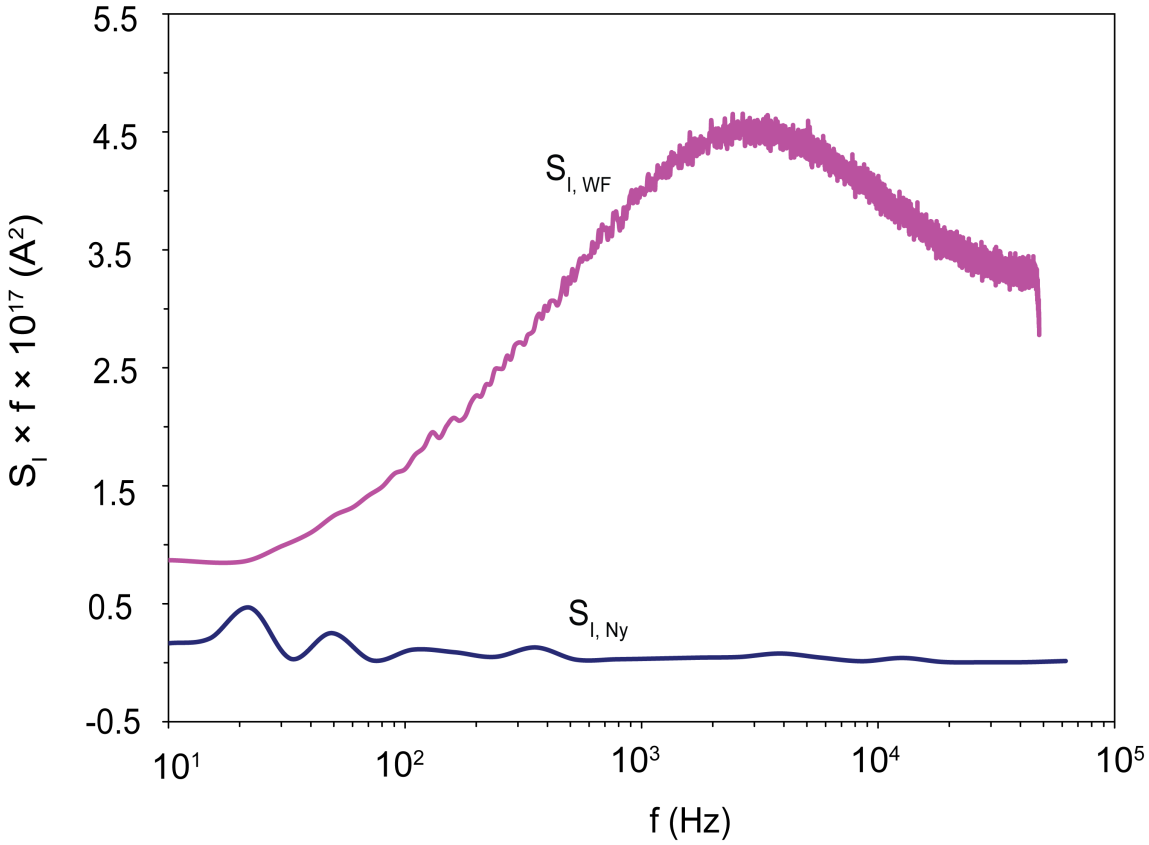

Figure 13: Two contributions to the drain current spectral density S_I of a PANI-IGFET. $S_{I,WF}$ fluctuation (red) and equivalent Nyquist noise $S_{I,Ny}$ (blue) originating from the resistance Z_{Re} of PANI. Both contributions were measured at V_G = 1.5 V.

was also negligible compared to the contribution from WF fluctuations. Therefore, it is concluded that observed fluctuations in PANI-IGFET drain current are caused by threshold voltage fluctuations, which, in turn, can be attributed to thermally induced, spontaneous, and stochastic fluctuations of WF of the PANI gate conductor. The possibility of separating the Nyquist noise and the WF fluctuations of the PANI film is possible with the IGFET platform and is probably the most valuable methodological aspect of this work.

3.2 Shape of the WF Fluctuations

It's already been mentioned that the WF fluctuations are not purely Lorentzian. Instead they appear to have a smeared Lorentzian character. The best fit is shown in figure 14 (squares and triangles) and is given by the sum of a "smeared" Lorentzian noise and a *1/f* component:

$$f \times S(f) = \left(\frac{A \times f/f_\tau}{1 + (f/f_\tau)^2} \right)^C + B \tag{38}$$

where A is the magnitude of the smeared Lorentzian which is related to the variance of the noise, f_τ is the corner frequency, C is an adjustable parameter between 0 and 1 determining the width of the peak, and B is the magnitude of the *1/f* noise. When $C = 1$, equation (38) represents a Lorentzian process with a single time constant, while smaller values of C indicate an increasing spread in time constants. A form of equation (38) with $C = 0.5$ has been used to describe noise originating from charge trapping in the channel of field-effect transistors [21]. We attribute the spread in time constants to the well-known disorder and inhomogeneity of conducting polymer films, and will refer to C as the broadness exponent. Note that broadness of the peak increases with decreasing broadness exponent. The *1/f* noise is attributed to the channel noise of the IGFET although inherent *1/f* WF fluctuations can't be ruled out.

3.3 Coherence Between Two IGFETs

Drain current fluctuations were measured, simultaneously, on two PANI-IGFETs, *A* and *B*, sharing a common PANI gate conductor (see figure 14). The coherence between

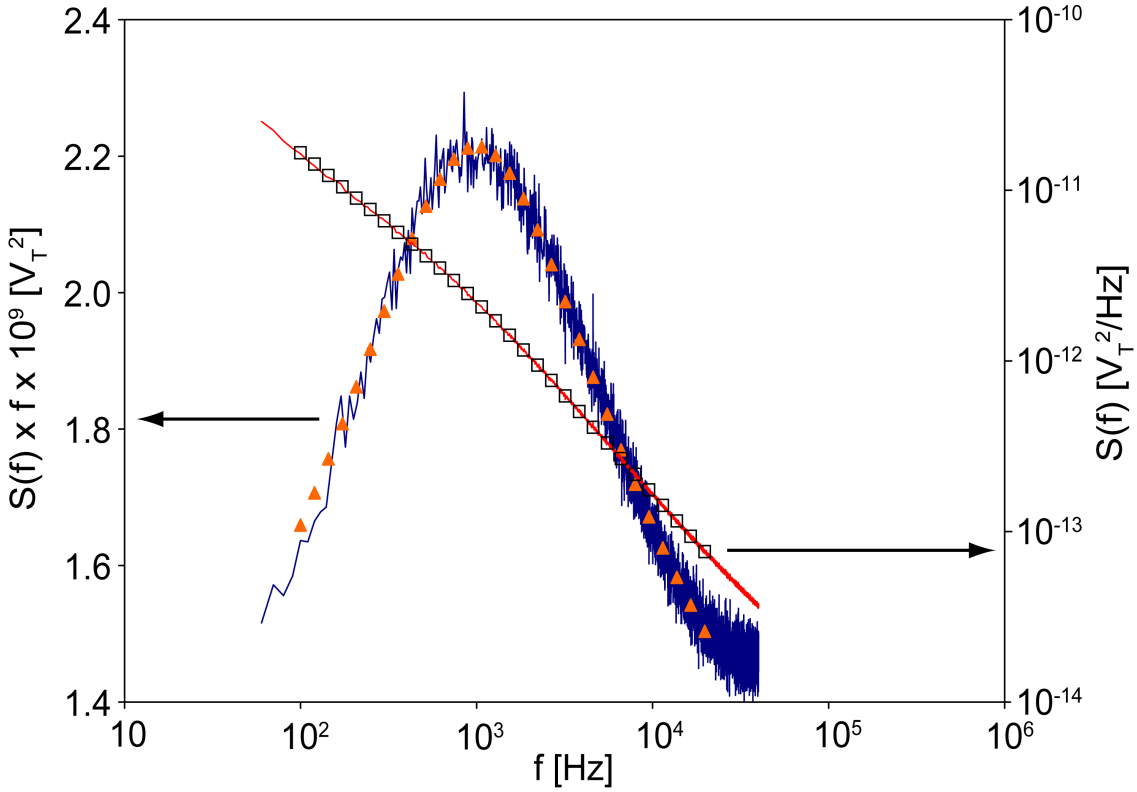

Figure 14: Smeared Lorentzian fit of PANI WF noise. The smeared Lorentzian fit is shown as squares and triangles in two representations of measured noise. The threshold, gate, and drain voltages are 0.56 V, 1.0 V and 4.95 V, respectively. The transconductance is 136.9 µA/V.

those two IGFETs was calculated from the cross- and auto-spectral densities according to [8].

$$coherence = \frac{|S_{AB}(f)|^2}{S_A(f)S_B(f)} \tag{39}$$

where $S_A(f)$ and $S_B(f)$ are the PSDs of channel *A* and *B*, respectively, and $S_{AB}(f)$ is the cross spectral density given by:

$$S_{AB}(f) = \lim_{T\to\infty} \frac{1}{T}\{[\bar{x}_A(f)]^* \bar{x}_B(f)\} \tag{40}$$

where the * indicates the complex conjugate. According to the Weiner-Khinchin Theorem, the inverse Fourier transform of the cross-spectral density is the cross covariance function. The coherence between two IGFET channels is a normalized

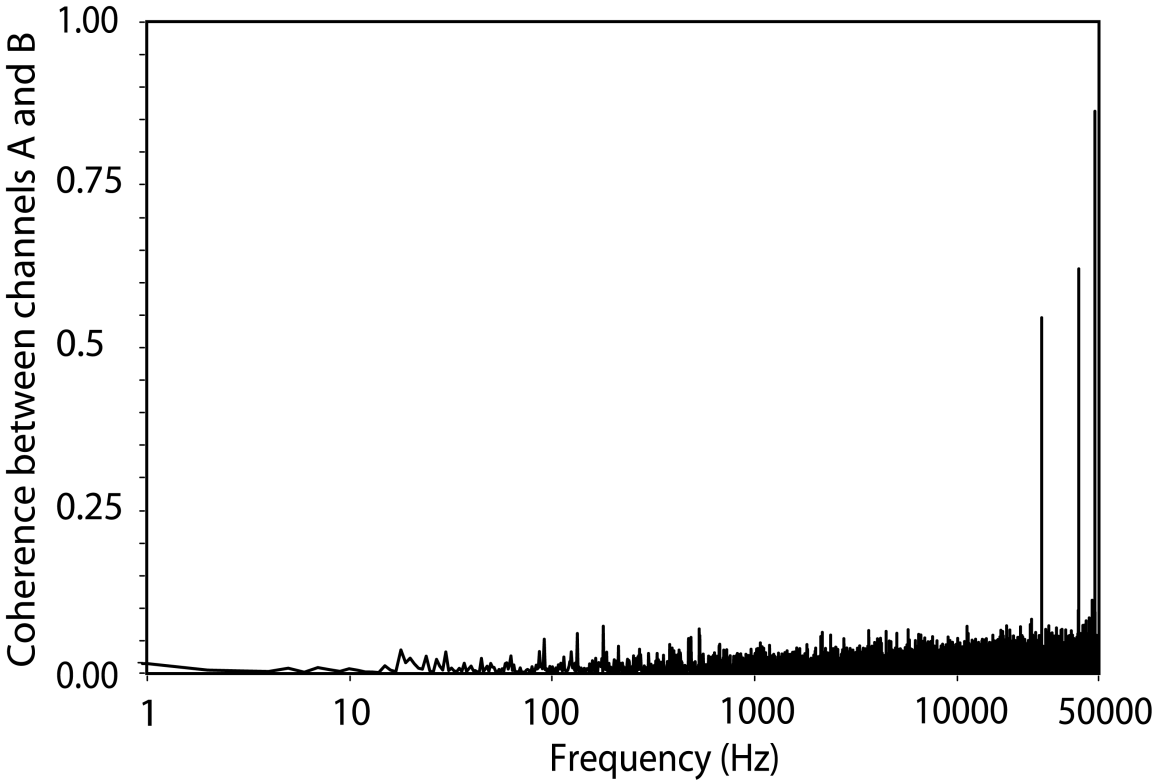

Figure 15: Coherence between two IGFETs with shared PANI gate operated at V_G = 1.5 V. The signals were a amplified and converted to a digital signal separately.

measure of the common signal between the two IGFETs [9b]. Figure 15 shows the typical coherence between two IGFETs with a common PANI gate: the coherence is zero. The

fluctuations are not spatially correlated within the bulk of the film. There are many possible explanations for this lack of coherence, including a finite correlation length of the fluctuations. Therefore, the observed noise must originate at the region that couples with the channel through the electric field, *i.e.* the space charge at the interface between the insulator and the PANI layer. Work function fluctuations in the rest of the film are very likely but at present time lie outside the observation window of this measurement technique.

3.4 Gate Voltage Dependence

In order to elucidate the effect of electric field on WF fluctuations, the PSDs were obtained at V_G = 1.0, 1.25, 1.5, and 2.0 V (figure 16). The drain current fluctuations are expressed as fluctuations of threshold voltage so that the magnitudes can be compared. Two trends are immediately evident. First, the time constant decreases with increasing gate voltage. This may be a result of the increasing electric field or the increase in charge carrier density. Secondly, the magnitudes of the peaks decrease with increasing gate voltage. The magnitude is proportional to the overall variance of the noise. In general, the variance of any thermodynamic fluctuation is proportional to the size of the system for extensive quantities, while the opposite is true for intensive quantities [22]. Since WF is an intensive quantity, the decrease in magnitude may indicate that the system size is increasing. Obviously, the thickness of the PANI film does not change. However, coherence measurements have confirmed that the measured noise originates only in a subsection of the film near the insulator. The dependence of noise magnitude on V_G

suggests that as V_G increases, the size of the subsection of the film from where the fluctuations originate increases.

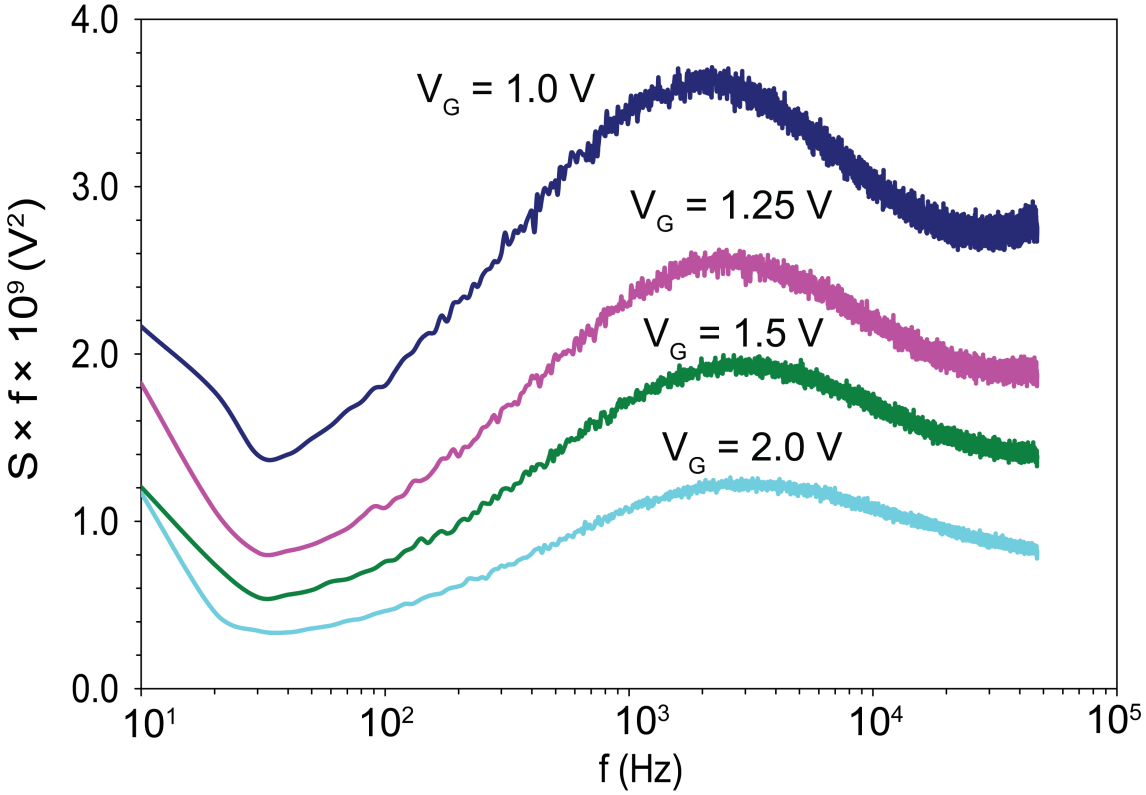

Figure 16: Dependence of PSD on V_G for Utah chips with HCl doped PANI at room temperature.

3.5 Temperature Dependence

To further probe the origin of WF fluctuations in the PANI gate conductor, the kinetics were studied as a function of temperature at constant V_G of 1.5 V (figure 17). The inset clearly shows that both the magnitude and the corner frequency are increasing with increasing temperature. Increase of the magnitude is attributed to the thermodynamically driven dependence of noise variance on the thermal energy; as temperature increases, the system fluctuates more. The evolution of the corner frequency suggests that the time

constant of the underlying process decreases with increasing temperature. Note that the PSD appears to be temperature independent at *ca.* 600 Hz. This apparent isosbestic point

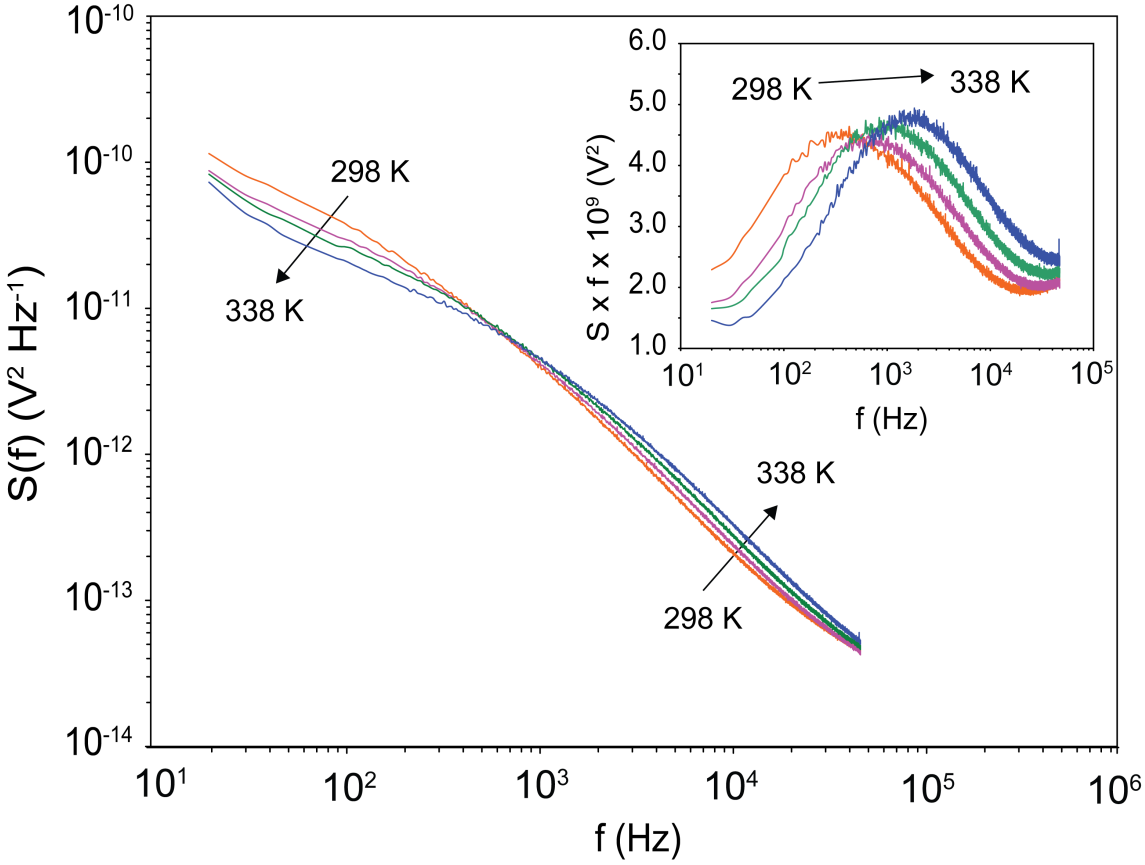

Figure 17: Dependence of PSD on Temperature for Utah chips with HCl doped PANI. The "isosbestic point" at ~ 700 Hz is more clearly visible in the PSD representation while the shift of the corner frequency is more visible in the inset. All measurements were done at V_G = 1.5 V.

is also present when the temperature dependence is probed at other gate voltages. We propose that this isosbestic point, which changes its location with gate voltage, is a consequence of the continuously distributed, field-dependent time constant of the Lorentzian noise [23]. As the temperature increases, the distribution is shifted to higher frequencies. Such as isosbestic point would not be present in the temperature-dependence of a pure Lorentzian noise.

The dependence of the corner frequency on temperature was investigated at gate voltages of 0.75, 1.0, 1.5, and 2.0 V (figure 18). The corner frequency follows the Arrhenius temperature dependence ($R^2 > 0.99$):

$$f_\tau = f_0 e^{-E_a/kT} \tag{41}$$

where E_a is the activation energy, k is Boltzmann's constant, T temperature and f_0 is a frequency prefactor. This confirms that a thermally activated process causes the WF fluctuations. The activation energies at each gate voltage were calculated from the slope of the Arrhenius plot (see inset). The activation energy decreases with increasing gate voltage from 350 meV at 0.75 V to 320 meV at 2.0 V. This suggests that either the increasing electric field or the increasing charge carrier density lowers the activation energy. The temperature dependence of the variance was also investigated at the same four gate voltages (data not shown). The increase in noise variance with temperature is nearly linear. Interestingly, the variance is more susceptible to temperature changes as the gate voltage decreases. This can be understood in terms of the size-dependence argument as already mentioned above: as gate voltage is increased, the size of the region coupling to the transistor channel also increases, and the variance decreases. Thus, the slope of the variance with respect to temperature decreases with increasing gate voltage.

3.6 Conclusions and Preliminary Model

It has been shown that the "excess noise" observed in the drain current of a PANI-IGFET can be attributed to the equilibrium thermal fluctuations of the WF of the PANI gate electrode. Using the fluctuation-dissipation theorem the kinetic properties can be

evaluated from the PSD of the fluctuations of drain current in the IGFET. In the temperature range 298 to 338 K a clearly distinguishable, yet broad, characteristic frequency is observed around 3000 Hz for films doped in the vapor phase by 1 M HCl.

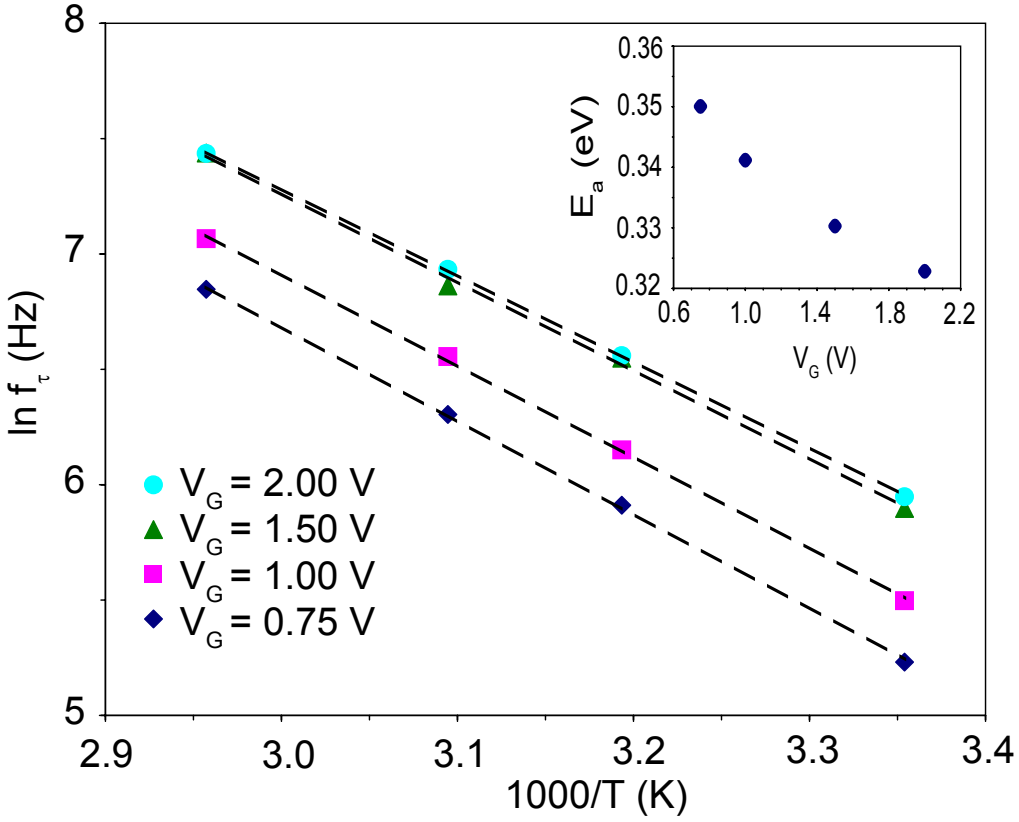

Figure 18: Arrhenius plots of corner WF fluctuation corner frequency for HCl doped PANI on Utah chip. Inset: plot of activation energy E_a (eV) as the function of applied gate voltage

The origin of these fluctuations is unclear at this point but it can be associated with fluctuations of the charge carrier density, with the thermal motion of the polymer chains, with the kinetics of mobile charge trapping/de-trapping, or stochastic fluctuations of the dipoles at the OS–insulator interface. It is an activated process, with activation energy in the range 320–350 meV. It is interesting to note that this activation energy

depends on the electric field at the PANI-insulator interface. It is decreasing with increasing electric field, as is the magnitude of the fluctuations. A similar trend of activation energy with gate voltage has been observed from drain current measurements of OFETs. The activation energy in that case was due to trapping at single grain boundaries of sexithiophene [24]. It should be noted that while the measured quantity in this work is different from the DC measurements in the OFET case, similar processes might be responsible.

We can deduce from the field dependence of the magnitude, as well as the absence of coherence between channels *A* and *B*, that the fluctuations have a finite correlation length. A useful analogy is that of local concentration fluctuations in an electrolyte solution. Macroscopically, the solution has a mean conductivity and ionic strength, but in any small volume element these properties fluctuate. Furthermore, the fluctuations in two different volume elements, while statistically the same, are not correlated: they are not fluctuating "in sync". Likewise, the WF of the PANI film, while having an average macroscopic value, can fluctuate locally within the film. Because of the direct coupling to the channel through the electric field, the WF fluctuations within a correlation length of the OS–insulator interface may be the only ones detectable with this approach.

On the basis of the experimental evidence presented in this chapter we propose a model of silicon–insulator–PANI junction, as it exists in the gate of a field-effect transistor with PANI gate conductor. It should be noted that unlike in the so-called "organic field-effect transistors" (OFET) no current passes through the conducting polymer. Therefore, the material is in true thermal equilibrium and the silicon part of the

device represents the "observation tool". The physical representation of this model is shown in figure 19. In the saturation regime, a space charge, of equal but opposite charge, is formed on each side of the insulator as shown in figure 19a. The charge neutrality condition is satisfied in the bulk. Because the WF fluctuations have a finite correlation length, the drain current is only affected by fluctuations near the PANI–insulator interface. The energy diagram, under flat-band conditions, is shown in figure 19b. The flat-band condition implies no band bending, *i.e.* no space charge, and a flat vacuum level across the insulator. This condition is used here only as an aid to illustrate how fluctuations in WF, σ_{WF}, result in measurable fluctuations in flat-band voltage, σ_V, *i.e.* threshold voltage fluctuations. Although we believe that the WF fluctuations occur independently of space charge formation, we cannot rule out that the presence of the space charge at the insulator is necessary for the measurement of the fluctuations, much like the passage of current is necessary for the measurement of resistance.

To our knowledge the equilibrium fluctuation analysis of IGFET with conducting polymer gate is the only feasible experimental approach for obtaining kinetic information about WF fluctuations and its spatial origin. It is interesting to note that the calculation of the impedance of the PANI from the observed noise would yield an unrealistically high value of approximately 10 GΩ. It would contradict the value of impedance directly obtained from AC impedance measurement across the film. It further underscores the unique advantage of this technique to yield information about dynamics of WF fluctuations in the space charge region, as opposed to Johnson noise. Thus it provides direct, unique information about the equilibrium surface field-effect in conducting polymers.

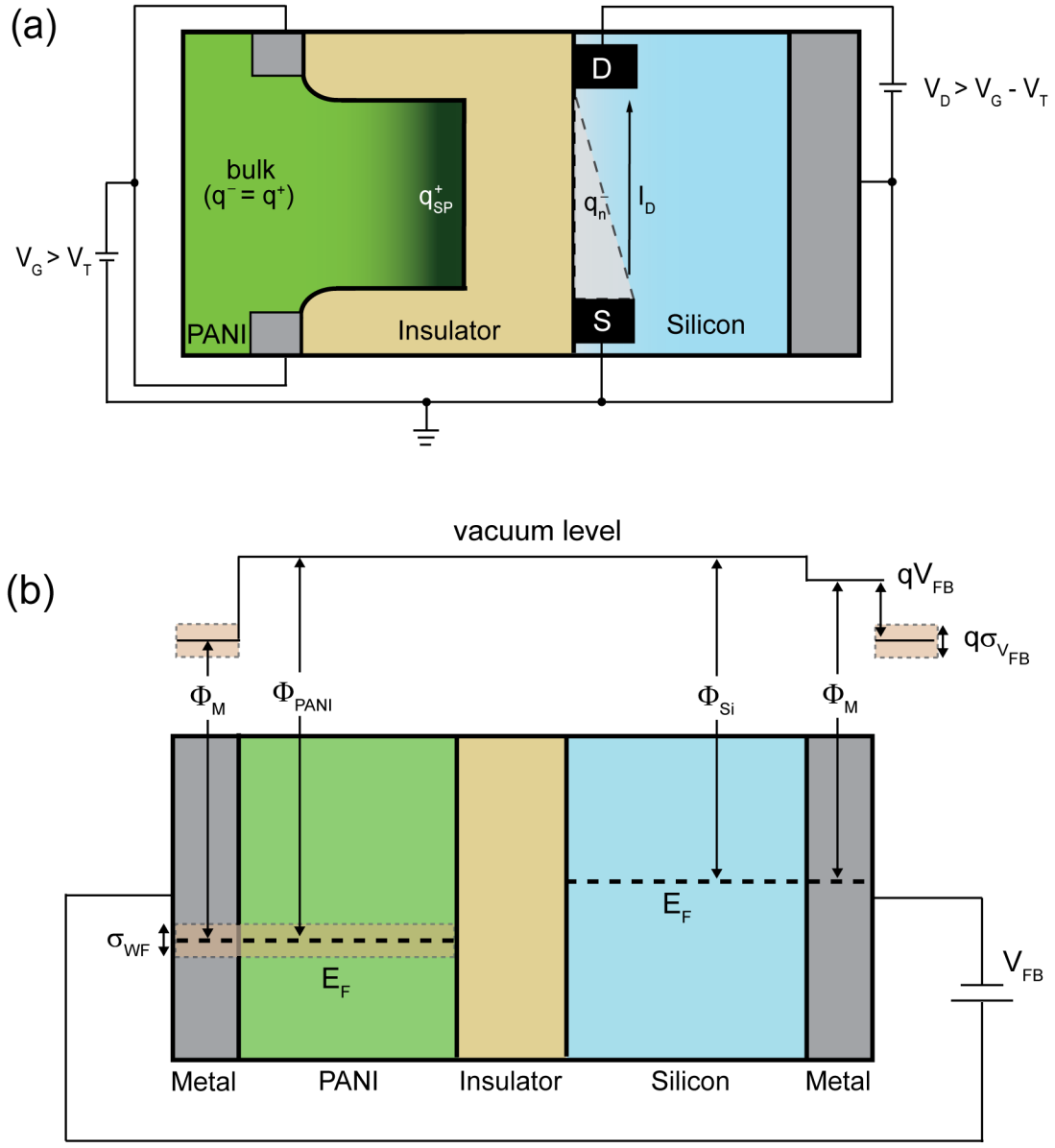

Figure 19: Conceptual model of WF fluctuations on an IGFET gate electrode. The space charge in the OS, $q_{SP}+$ is coupled to the channel in the silicon, q_n^-, through the electric field. Fluctuations of q_n^- result in fluctuations of drain current I_D. (b) Energy band diagram of the silicon – insulator – organic semiconductor junction under flat-band conditions. Here, the flat-band voltage, V_{FB}, is applied so that no electric field is present in the insulator, *i.e.* the vacuum level is flat across the silicon – insulator – OS interface. Fluctuations of OS work function are depicted by the small band around the OS Fermi level.

CHAPTER 4

PROTONATION AND DOPING DEPENDENCE

In this chapter, the PANI WF fluctuations are examined as a function of protonation and charge-transfer doping. The protonation state of PANI is systematically varied by UV irradiation of films containing triphenylsulfonium trifluoromethanesulfonate (PhT). Upon irradiation of the PANI-PhT films, triflic acid is formed which protonates PANI in the solid state. Exposing PANI films to the electron donor gases ammonia (NH_3) and dimethylamine (DMA) facilitates charge-transfer doping. Like chapter 3, temperature and gate voltage will be systematically varied to obtain information. The chapter will end with a description of the working hypothesis.

4.1 Gate Voltage Dependence of PANI-PhT

Typical PSDs of an IGFET with PANI-PhT gate electrode at various gate voltages, before illumination, is shown in figure 20. As already discussed, the peak is the result of spontaneous WF fluctuations of the PANI gate, whose contribution to the drain current noise is in excess to device noise, electromagnetic interference, Johnson noise, and amplifier noise. A thermally-activated kinetic process with a distribution of time constants induces these WF fluctuations. The application of a positive V_G results in accumulation of positive charges at the PANI-insulator interface, leading to formation of a space-charge region and upward band bending. This is accompanied by an increase of f_τ

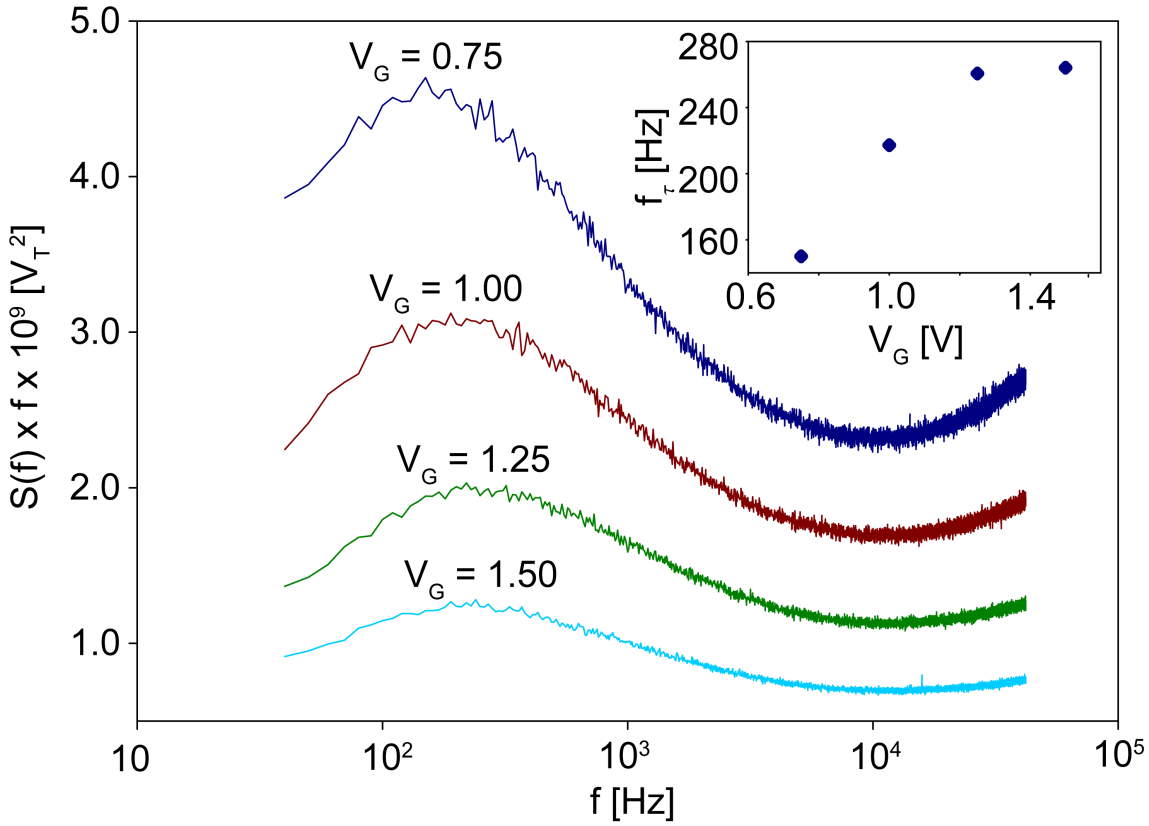

Figure 20: Dependence of PSD V_G for GT-03 chip with PANI-PhT. Magnitude decreases and f_τ increases with increasing V_G (inset). These trends have been observed in lightly-doped PANI films regardless of doping level, dopant type, or film preparation in general. The transconductance at 0.75 V, 1.00 V, 1.25 V, and 1.50 V is 85.5 μA/V, 136.9 μA/V, 199.6 μA/V, and 266.1 μA/V.

(inset) and a decrease of the magnitude. These trends are in qualitative agreement with our previous study of WF fluctuations of PANI films doped with HCl (chapter 3). In fact, this behavior is a general property of WF fluctuations for all PANI films studied, independent of film preparation, casting solvent, dopant, molecular weight and the device on which the films were cast.

For a fluctuating extensive thermodynamic variable, *i.e.* E_F, the magnitude decreases as the size of the system decreases [22]. The decreased magnitude, which is

proportional to the variance of the noise, is attributed to an increase in system size. Obviously, the PANI film does not grow or shrink with changes in V_G, but coherence

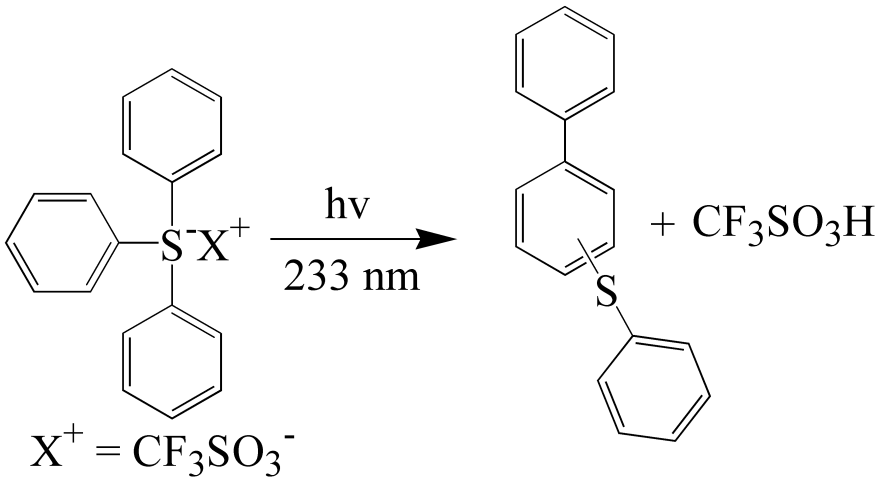

Figure 21: Photolysis of PhT to form triflic acid

measurements have confirmed that this technique can only penetrate to a finite distance above the insulator. As discussed in the previous chapter, the size of this slice of the film may be changing. In order to determine what defines the thickness, further experiments are needed. These results will be discussed below.

4.2 Irradiation of PANI-PhT

Next, PANI-PhT was doped *in situ* by irradiating the film at 233 nm from a 5 W deuterium lamp for up to 480 s. The PhT undergoes irreversible photolysis and generates a proton that can dope PANI in the solid state (figure 21) [25]. The I_D-V_G curves are shown in figure 22 along with the changes in both V_T and g_m at a V_G of 1.0 V (inset). The increase in V_T can be attributed to a decrease in E_F along with possible changes in the surface component of WF. Protonation increases the WF and introduces delocalized

charge carriers in the film as verified by Kelvin probe and UV-Vis experiments, respectively [25b]. Furthermore, the resistance steadily decreases with increasing

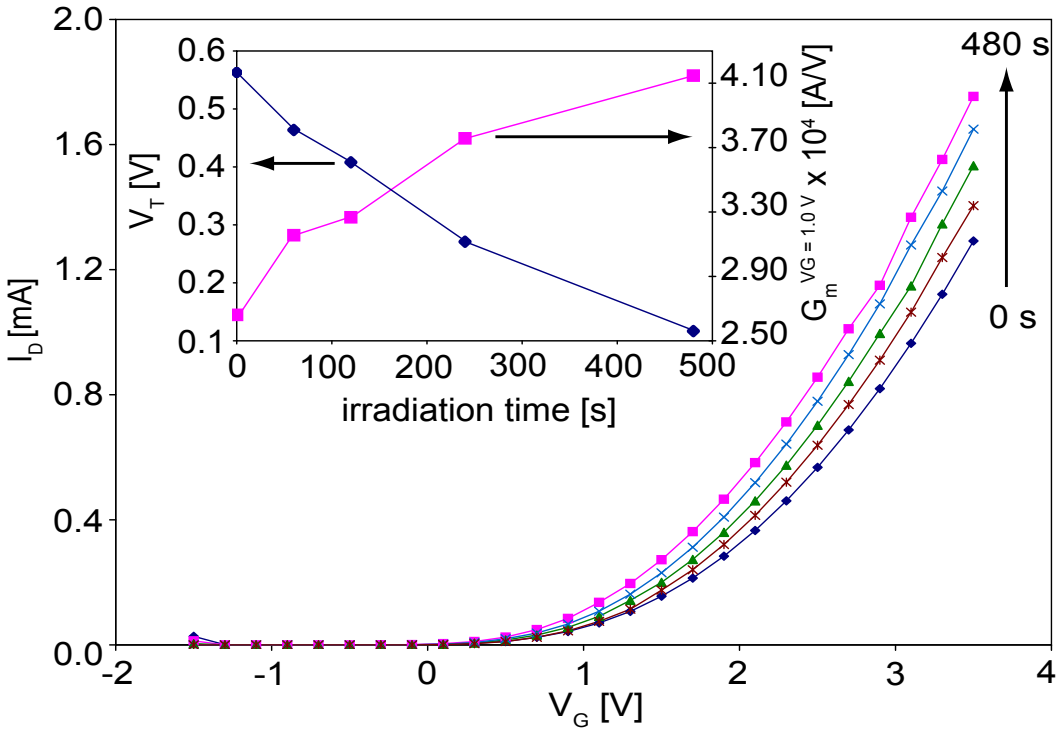

Figure 22: Changes of IGFET parameters with irradiation time (protonation). The I_D-V_G characteristics for 0 s, 60 s, 120 s, 240 s, and 480 s irradiation of PANI-PhT (1:10) from a 5 W deuterium lamp is shown. The inset shows the change in V_T and g_m at a V_G of 1.0 V. The film was allowed to equilibrate overnight after each irradiation.

irradiation time (not shown) and the films change color from blue to green. No changes were observed for PANI films without PhT, confirming that the changes in electronic and optical properties are, indeed, caused by photolysis of PhT and subsequent protonation of PANI.

Protonation also affects the WF fluctuations of the PANI-IGFET. In figure 23, the progression of the WF noise with irradiation time is shown for a gate voltage of 1.0 V. Two trends are immediately apparent: f_τ increases and the magnitude decreases with increasing doping. Furthermore, f_τ becomes more sensitive to V_G as doping increases (inset). Due to the peak shifting above the highest frequency of our measurement, data

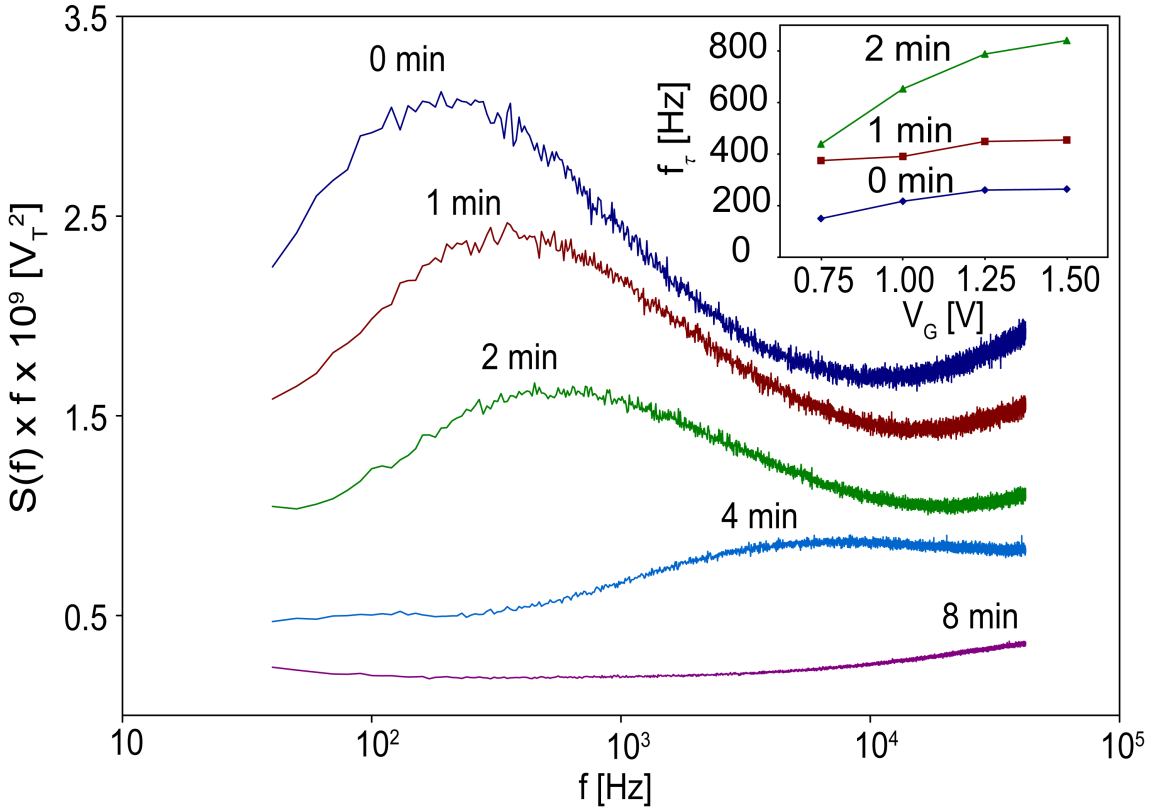

Figure 23: Effect of irradiation of PANI-PhT (1:10) on the PSD at V_G = 1.0 V. The inset shows the increase of f_τ as a function of gate voltage for 0 min, 1 min, and 2 min irradiation time. The film was allowed to equilibrate overnight after each irradiation.

fitting could only be carried out on the first three spectra (0, 1 and 2 minutes of irradiation). These results suggest that the WF fluctuations become more rapid, *i.e.* the activation energy is lowered, at higher doping levels. Indeed, a fully doped PANI film shows a purely *1/f* noise due to the peak being at higher frequency than our system is

capable of measuring. On the other hand, lightly doped films of PANI in the emeraldine base form show a low f_τ, sometimes below the frequency range of our measurement set-up. The decrease in magnitude suggests that the size of the observed slice of the film grows with increasing protonation and, therefore, increasing conductivity. It is important

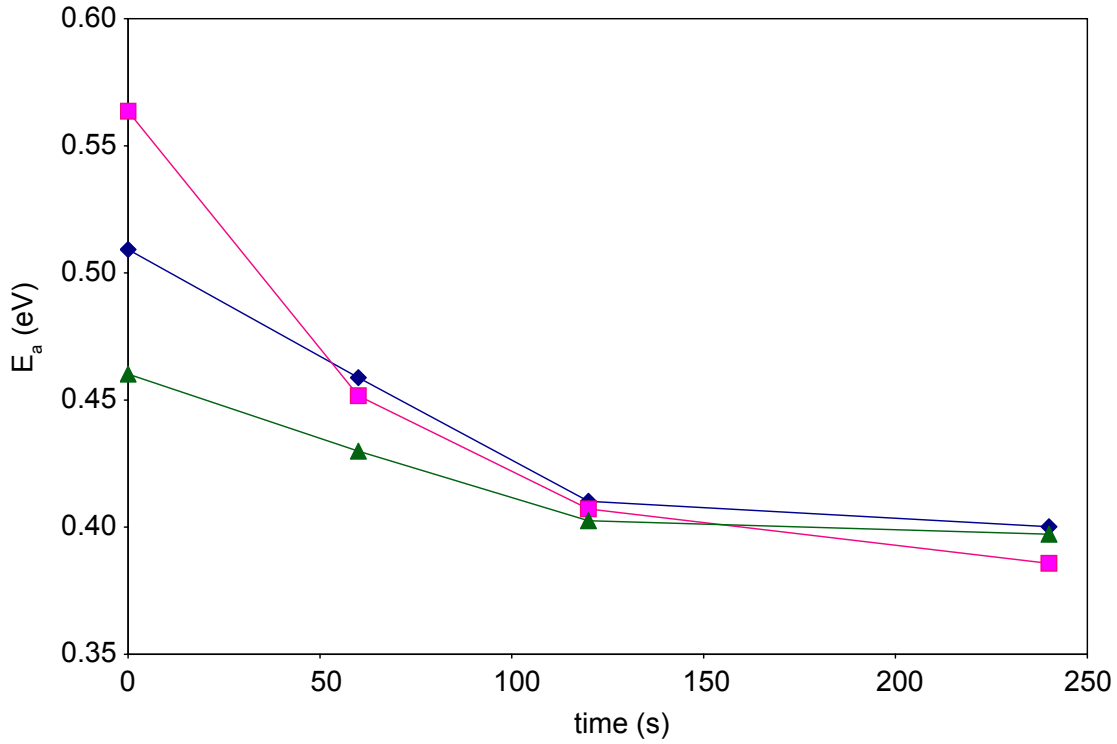

Figure 24: Change of the activation energy with irradiation time for three IGFETs with PANI-PhT (1:10) gate electrodes. The activation energy was calculated from temperature dependence of f_τ at constant $V_G = 2.0$ V.

to note that the size also increases with increasing V_G, which is also accompanied by an increase in conductivity near the PANI-insulator interface.

To confirm that the activation energy is decreasing with protonation, the PSD was measured at 298 K, 313 K, 323 K and 338 K after 0 s, 60 s, 120 s and 240 s of irradiation. At each irradiation time, the corner frequency followed Arrhenius temperature dependence as was discussed in chapter 3. The changes in activation energy with irradiation time are shown in figure 24. As expected, the activation energy decreases with increasing irradiation time: doping PANI increases the rate of fluctuations by lowering the activation energy for the underlying process.

4.3 Charge-Transfer Doping

Charge-transfer doping of PANI by an electron donor results in a decrease of WF and conductivity [12a]. Exposing PANI to ammonia gas and dimethylamine up to 1000 ppm and 100,000 ppm, respectively, was carried out. The higher concentrations of DMA are presumably due to a weaker charge-transfer interaction and the bulkier nature of the DMA molecule. As seen in figures 25a and 25b, doping with these electron donors results in a decrease of f_τ and an increase of the magnitude. These trends are in agreement with the PhT doping results, albeit in the opposite direction. The change of f_τ with concentration for two different PANI films is shown in the insets. Both follow a logarithmic dependence but with slightly different slopes and y-intercepts. The WF noise is sensitive to small differences in the average values, *i.e.* V_T, resulting from the random packing of the polymer and the random dopant distribution in the measured slice of the film as reflected in small differences in the insets.

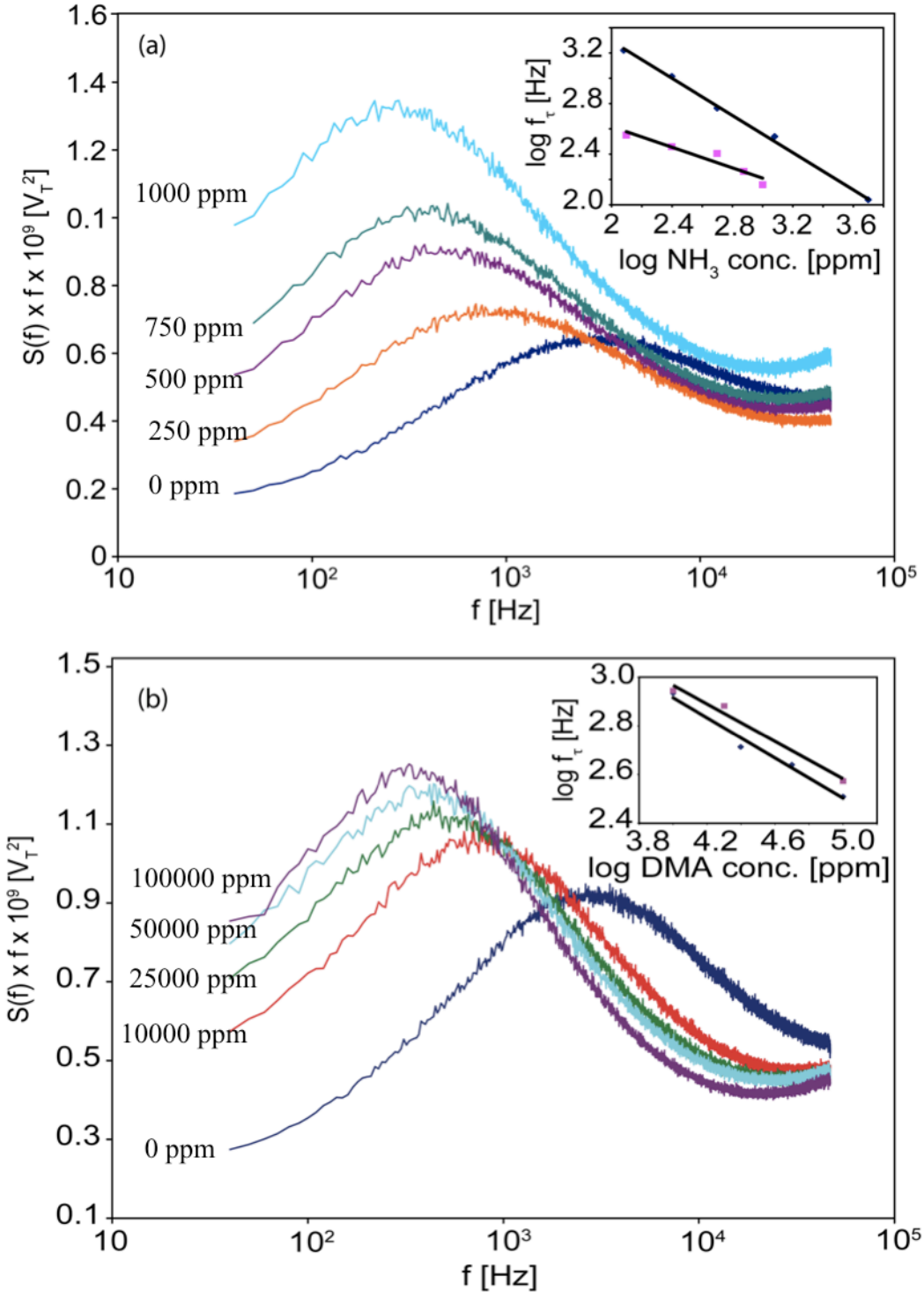

Figure 25: (a) Response of PSD upon exposure to 0, 250, 500, 750 and 1000 ppm of NH_3 in air at a V_G of 1.5 V. (b) Response of spectral density upon exposure to 0, 10,000, 25,000, 50,000 and 100,000 ppm of DMA in air on at a V_G of 1.5 V. Insets shows the decrease of f_τ with increasing gas concentration for two PANI films.

In general, all three doping scenarios (PhT, NH_3 and DMA) shift V_T, the magnitude and the broadness exponent, but the relationship between V_T and the noise parameters depend on the dopant. These relationships are shown in figures 26a and 26b for C and f_τ, respectively. In each case V_T, f_τ and C have been normalized to their initial values. The dependence of f_τ on V_T is approximately linear on a log-log representation for all three dopants within the doping ranges studied. In each case, f_τ increases with decreasing E_F. The change in f_τ mirrors the expected change in conductivity upon p- and n-type doping of PANI films. The slopes and y-intercepts differ for each dopant presumably due to differences in the interactions between the dopants and the PANI film.

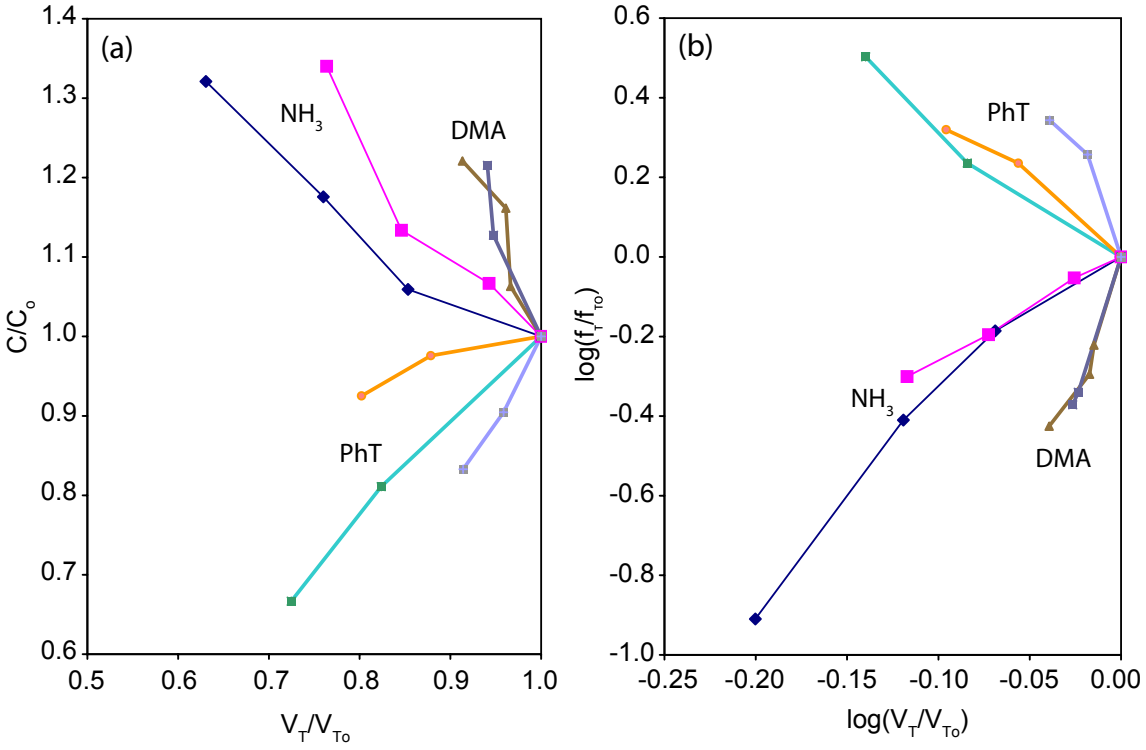

Figure 26: (a) Relationship between f_τ and V_T for three dopants and (b) relationship between C and V_T for three dopants.

The changes in C with V_T follow similar behavior between the three dopants but in each case the relationship is linear. Increasing the conductivity and work function results in a broader spectrum. Again, the exact slope depends on the particular dopant.

4.4 Working Hypothesis of PANI WF Fluctuations

Based on these results, we propose that the WF fluctuations are the consequence of spontaneous and stochastic trapping/detrapping of charge carriers near the PANI-insulator interface as shown in figure 27a. The activation energies measured are within the ranges found for charge hopping in emeraldine salts by Zuo *et al.* [26] and in polypyrrole by Dalas *et al.* [27]. We propose that fluctuations in the distribution of occupied energy levels induce corresponding fluctuations of E_F. This hypothesis is underscored by the following observations:

1. Increasing V_G increases f_τ. As positive charge carriers are concentrated in PANI near the interface, energy levels bend upward towards E_F (figure 27b). Reversible hopping between traps occurs in trap states positioned around the E_F. An exponential density of states (DOS) is assumed in the gap, *i.e.* the number of traps at an energy around E_F increases as the bands bend upward. The density of these traps also increases, which decreases the activation barrier needed for hopping between sites.
2. Increasing the protonation level increases f_τ and n-doping decreases f_τ. Upon protonation, the E_F of PANI shifts downward toward the valence band. Again, the

DOS increases close to the valence band; more trap states are fluctuating between empty and occupied states and they are located closer together (figure 27c). On the other hand, secondary doping by electron donors shifts E_F up, decreasing the number of available traps and the density of these traps (figure 27d).

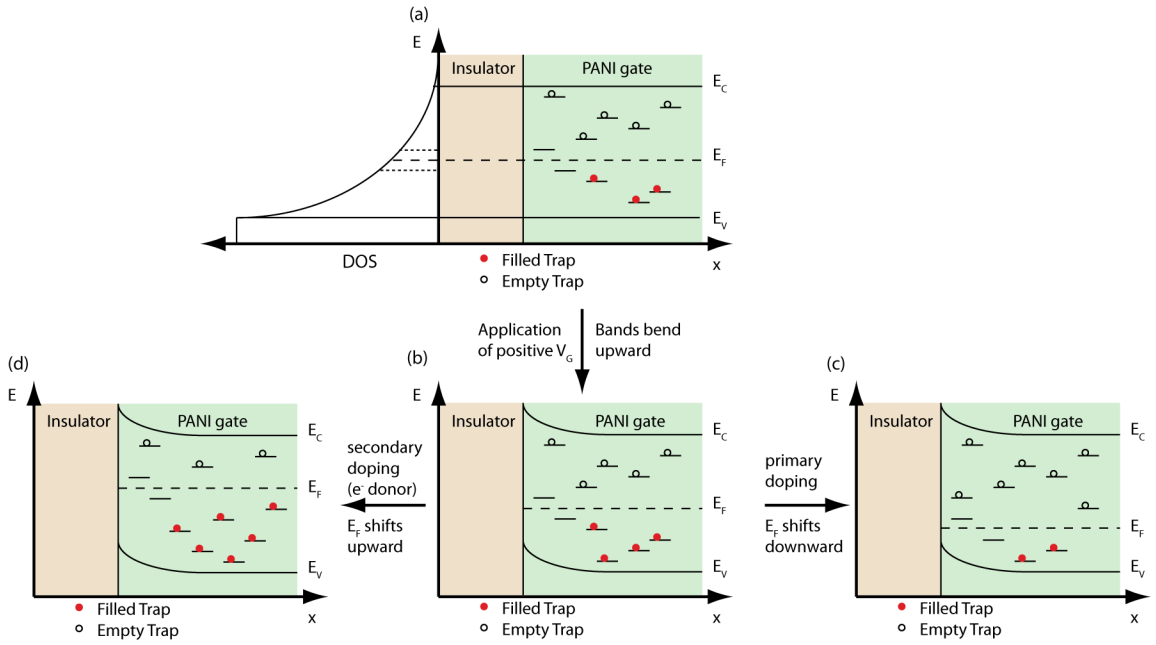

Figure 27: Charge-hopping model of WF fluctuations. Energy band diagrams at the PANI-Insulator interface. (a) Under flat band condition the conduction and valance band edges (solid lines) are flat. Localized traps are shown as short lines between E_C and E_V. The density of traps increases towards the band edges. Traps below E_F are occupied with electrons (red circles) and traps above E_F are empty (hollow circles). Traps around E_F are constantly and spontaneously exchanging electrons, resulting in fluctuations of E_F. The rate of this exchange (at a constant temperature) depends on the number of fluctuating traps and the distance between fluctuating traps, which depends on the density of traps around E_F. (b) Upon application of a positive gate voltage, positive charges accumulate near the PANI-insulator interface and the energy levels bend upward towards E_F. The number and density of traps with energy near E_F increase. (c) N-type doping shifts E_F upward, decreasing the number and density of traps near E_F. (d) P-type doping shifts E_F downward and increases the number and density of traps around E_F.

In order to understand the changes in magnitude, the inhomogeneity of the PANI film must also be taken into account. The phase segregation of organic semiconductors into conducting phases separated by amorphous phases is well known [28]. In particular, the phase segregation of PANI has been confirmed using magnetic susceptibility measurements [29] and current sensing atomic force microscopy [16, 30]. Furthermore, using scanning tunneling spectroscopy, Yau *et. al* have shown that the size of these crystalline domains in the fully-doped, emeraldine salt form of PANI are up to 80 nm while deprotonation reduces the size of these domains to approximately 30 nm [31]. Originally, we speculated that the slice observed with this method could be defined either by the space-charge region in PANI or by the characteristic length over which WF fluctuations are correlated, *i.e.* the correlation length. In the first case, the fluctuations would essentially be of the surface component of WF only. In the latter, the bulk WF would be the fluctuating quantity but, due to the inherent disorder and low conductivity of the PANI film, only fluctuations within a correlation length of the interface can be measured. If the space-charge region defined the system size then p-doping would result in a smaller system, leading to larger noise magnitude, but the opposite trend was observed. Furthermore, impedance measurements would presumably give analogous information, *i.e.* space-charge fluctuations would be part of the Johnson noise. Our data suggests that the correlation length of WF fluctuations defines the system size. This correlation length depends on the extent of charge carrier delocalization. We speculate that fluctuations are only correlated within the ordered, crystalline domains, outside of which the correlation drops off rapidly. It is the changes in the sizes of these domains and the E_F values within them, as well as the distribution of these quantities between neighboring domains, that

cause the V_T fluctuations. For instance, the high carrier density that results from the application of a positive V_G has been associated with an insulator-to-metal transition in FET devices based on poly(3-hexylthiophene) [32]. Increasing the doping level can also lead to band-like conductivity in organic semiconductors, including PANI. In fact, the ordering of PANI chains, a prerequisite for extended electronic states, has been found to increase with doping [33]. For these reasons, we postulate that the WF fluctuations are only measureable within a correlation length from the insulator interface, and that the correlation length is defined by the average size of the crystalline domains near this interface.

This observation leads to an interesting question: is E_F a bulk property of disordered conductors? The disorder of conducting polymer films leads to the absence of extended electronic states and the presence of localized charge carriers. The Fermi level in such a system, defined in a general way, as the average chemical potential of the electron, will vary from place to place within the film depending on the local morphology and charge density. The absence of a bulk extended electronic state does not preclude the presence of limited, isolated delocalized states within the crystalline domains. Therefore, it is natural to assume that each of these ordered regions each have a unique E_F and each

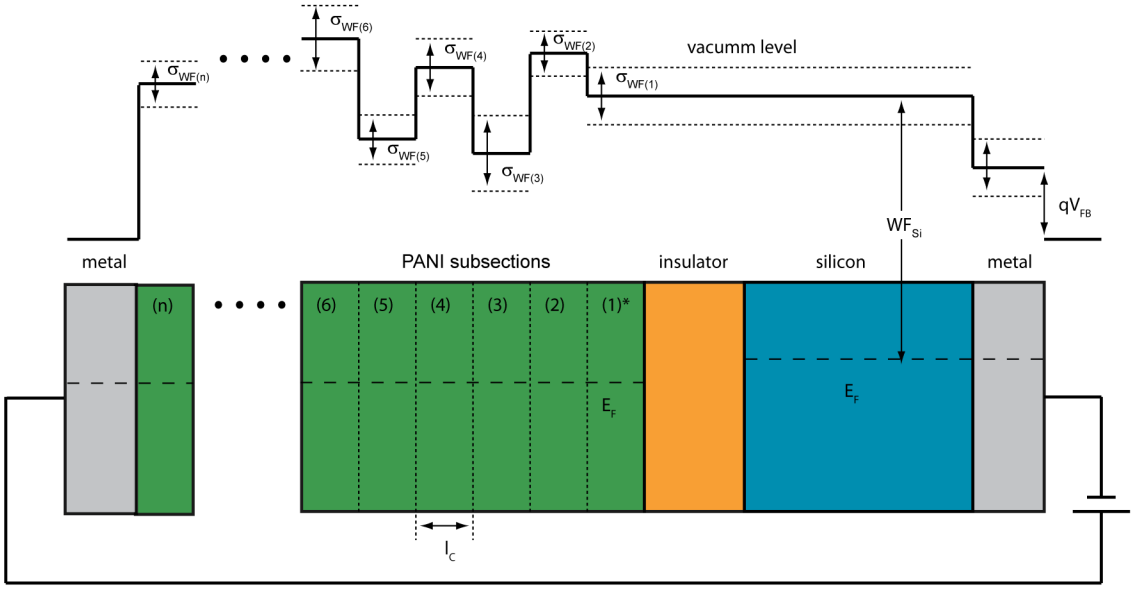

Figure 28: Localization length of WF fluctuations for PANI-IGFET. Energy level diagram for PANI-insulator-silicon junction of an IGFET under flat-band conditions, *i.e.* no band-bending. The Fermi level is shown as a dashed line and fluctuations are shown as a dotted line around the vacuum level. The disorder-induced correlation length of E_F requires the segmentation of the PANI film into n subsections, or "virtual films" each with a thickness given by the correlation length, L_c. Although E_F the same for each segment, the WF of each may differ, as shown by the variation in vacuum levels. This variation has been exaggerated to illustrate this point. Fluctuations of E_F in any subsection except the first one will not affect the drain current since these fluctuations will cancel out at the "interface" with its two nearest neighbors. The thickness, L_C, of each layer depends on the conductivity, disorder, and electric field.

one extends to fill a volume determined by the doping, charge density and polymer chain packing. It is important to note that since these conducting regions are in thermal equilibrium and in electrical contact, their Fermi levels are aligned and a contact potential exists between them. Furthermore, since only changes in the WF of the conductor directly on the gate insulator affect V_T, only the conducting domains near the insulator affect the IGFET drain current.

The fundamental difference between a PANI-IGFET and a MOSFET is not in the device physics but in the physics of the gate conductor itself. Figure 28 shows the

disordered PANI film as an equivalent stack of "virtual" PANI films, each as thick as its correlation length. Note that the changes in WF between virtual layers and the size of the fluctuations around the vacuum level are exaggerated to clearly show the concept. Furthermore, the demarcations between the virtual layers aren't as definite as shown since the correlations typically decay exponentially. Only fluctuations of the bottom "virtual" film are transduced into drain current fluctuations: fluctuations in any of the other layers cancel out [2]. The size of this layer can change with doping and electric field, *i.e.,* V_G. This observation has important consequences for gas sensing applications and other device applications utilizing disordered organic semiconductors, in particular when the interfaces between organic semiconductors and other conductors or insulators play a key role in device operation.

Chapter 5

CONCLUSIONS AND FUTURE WORK

5.1 Conclusions

WF fluctuations provide unique information about the dynamics of the space charge region in conducting polymer films at equilibrium. In the preceding chapters, the proof-of-concept of this new measurement technique has been demonstrated. PANI was used as a representative conducting polymer and, by systematically varying the electric field, temperature and doping (by protonation or charge-transfer doping), a simple model for the origin of these WF fluctuations was proposed. This model involves the spontaneous hopping of charge carriers near the Fermi level. Furthermore, coherence measurements were used to determine that these fluctuations are localized to a thin region near the PANI-insulator interface. This localized dynamic behavior of conducting polymers should be of interest to furthering our understanding of conducting polymers and advancing their applications in organic electronics.

The WF fluctuations of PANI were found to have an underlying kinetic process with a distribution of time constants. This process was thermally activated with an activation energy of *ca.* 350 meV, which depends on the electric field and the doping of the film. The activation energy decreased with increasing gate voltage. Generally, it was found that increasing the conductivity near the space-charge region increased the rate of the underlying process. Since Fermi level is a measure of the distribution of charge

carriers within a conducting phase, fluctuations in this distribution, most likely by hopping between localized states, is likely responsible for fluctuations of the Fermi level.

Furthermore, increasing the space-charge conductivity decreases the magnitude of these fluctuations. Since magnitude and system size are inversely related for intrinsic thermodynamic properties, this suggests that the slice of the film from which the fluctuations are measured, increases with increasing conductivity. It is well known that the threshold voltage of an IGFET only depends on the WF difference between the layers directly adjacent to the gate insulator. The inhomogeneity and phase segregation of PANI most likely results in a PANI-IGFET in which only the layer of PANI directly on top of the insulator contributes to the threshold voltage. This observation has important consequences for the use of conducting polymers in organic electronics.

The dispersion in time constants, characterized by the parameter *C*, was found to decrease with decreasing conductivity. The proposed model can also explain this trend: as conductivity decreases, the probing depth decreases, as evidenced by the changes in magnitude. As this slice of the film becomes thinner, the fluctuations originate from what is, presumably, a more homogenous subsection of the film. The morphology of the film must vary with thickness and distance from the insulator due to differences in solvent evaporation rates and the influence of the insulator surface. This difference in morphology influences the electronic properties of the film, including the density of states within the band gap and the location of Fermi level. As the work function fluctuations include thicker slices of this film, these inhomogeneities are manifested as an increased broadness of the Lorentzian PSD.

5.2 Future Work

The next step for this project is to fabricate new chips that are optimized for noise measurements. Specifically, the channel noise should be reduced as much as possible. Secondly, the channel should be shorter to facilitate faster response time. This coupled with a wider bandwidth low-noise preamplifier and analog-to-digital converter with higher sample rate will enable WF fluctuations above 50 kHz to be measured. The limiting factor for bandwidth limitation is currently the preamplifier. The importance of increasing the bandwidth can be appreciating by considering that in the present measurement set-up, the WF fluctuations of highly doped PANI are above the 50 kHz bandwidth currently obtainable. For this reason, the results in this thesis are focused on lightly doped films. Will fully doped films behave the same way? Furthermore, even for the PSDs of lightly doped films in this thesis, *e.g.* figure 20, there appears to be another process present at frequencies above 50 kHz. The presence of multiple Lorentzians is intriguing but currently out of range for the measurement set-up.

Gate materials other than PANI can be studied using this technique. While PANI has the advantages of a highly tunable conductivity (and work function), high solubility and stability, its inherent disorder makes interpretation difficult. Do WF fluctuations in other conducting polymers, such as polypyrrole and polythiophene, behave similarly? On the other hand, amorphous silicon would be a model system in which doping and disorder can be systematically controlled. Amorphous silicon is a common IGFET gate material for IGFETs. Another model gate conductor would be a granular metal. The working hypothesis for the WF correlation length is based on the phase segregation of PANI.

These phases are inhomogeneous in size and conductivity. A granular metal gate electrode, in which the size of the grains and their identity can be systematically controlled, could test this hypothesis.

APPENDIX A

ELECTROPOLYMERIZATION OF PyDPA and PyDP

A.1 Introduction

Electrochemical methods allow for precise control and monitoring of the electropolymerization of conducting polymers. The electronic conductivity, morphology, and ion-exchange properties of the conducting polymer can be precisely tuned through choice of solvent, dopant ion, applied potential, etc. This work is focused on the controlled electropolymerization and characterization of phosphonate-bearing polypyrrole and its potential application in electrochemical DNA hybridization detection (figure 29).

In this scheme a platinum electrode is coated with a conducting polymer bilayer. The inner layer is a relatively thick, highly conducting polypyrrole film. Cycling the potential of this polypyrrole layer (or any conducting polymer film) leads to oxidation and reduction of the film: creation and removal of polarons, respectively. This process is accompanied by insertion of counter ions from the electrolyte solution to maintain charge neutrality. The ingress and egress of these ions lead to a cyclic voltammogram with characteristic position and shape. On top of the polypyrrole a thin layer with pedant phosphonate groups is electropolymerized. The phosphonate group exists mainly in its monoanionic form in neutral pH (for *n*-propylphosphonic acid, pK_1=2.49 and pK_2=8.18 [34]). The electrostatic binding of Mg^{2+} ions by dipping the electrode in an aqueous

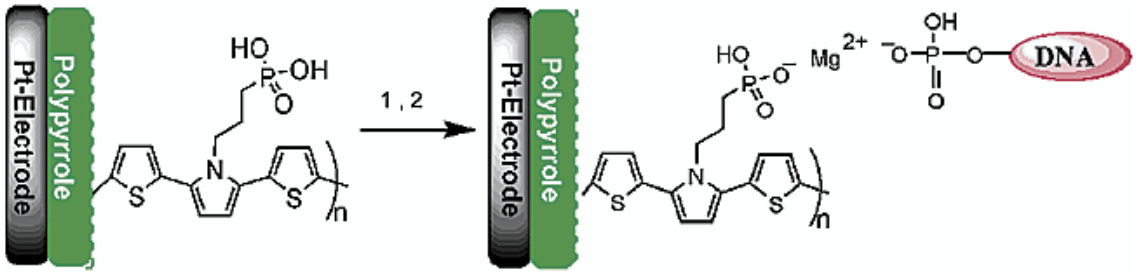

Figure 29: Electrochemical DNA hybridization detection scheme

solution of $MgCl_2$ leads to the availability of positive charges on the electrode surface, which can electrostatically bind the phosphate backbone of single-stranded DNA oligomers. The sequence of the oligomer is such that it selectively hybridizes with a target sequence when placed in a solution of DNA. If the electrode with hybridized DNA is cycled in an aqueous background electrolyte containing no DNA the immobile negative charge density due to the DNA phosphate backbone impedes the exchange of cations to and from the polypyrrole layer. The output is shrinkage and change in shape of the cyclic voltammogram after hybridization. This method has been applied successfully in the detection of DNA oligomers and hepatitis C virus [35].

Interest in conducting polymers bearing pendant phosphonate groups extends beyond DNA sensing applications and biomolecule immobilization. The presence of immobile charges on the polymer backbone in neutral aqueous solution leads to the possibility of self-doping. Self-doped polymers have increased solubility and improved rates of doping/dedoping [36]. Understanding the mechanism of doping is an area of active research contributing to the overall understanding of electrochemistry of conducting polymer coated electrodes. Polypyrrole films, particularly overoxidized polypyrrole and polypyrrole with pendant carboxylic acid groups, have been shown to act

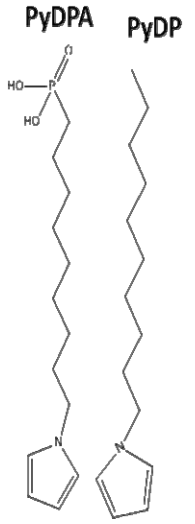

Figure 30: Chemical structure of PyDPA and PyDP

as anion-excluding films [37]. The presence of phosphonate groups should also provide permselectivity leading to potential applications in ion-selective electrodes and ion-separation membranes. The electrochemistry of phosphonate-bearing conducting polymers has not been studied extensively.

The outer layer used in the previous DNA sensor studies was polymerized from 2,5-dithienyl-(*N*-3-phosphorylpropyl)pyrrole, TPTC3. This molecule has the disadvantage of being unstable in the monomer form. Furthermore, the morphology and conductivity of the poly(TPTC3) layers proved difficult to control. The chemical structure of 1-pyrrolyl-10-decanephosphonic acid (PyDPA) is shown in figure 30. PyDPA provides a phosphonate group like TPTC3 but is stable in the monomer form. Furthermore, we have recently obtained a derivative of PyDPA that does not contain the phosphonate group, PyDP. The polyPyDP can be used as a reference polymer and the copolymerization of the PyDPA and PyDP can allow controlled phosphonate density

within the film. Full details of the polymerization of polyPyDPA and behavior of film in aqueous solutions have been published in ref [38]. Some of the results will be highlighted below along with some preliminary results concerning polyPyDP, poly(PyDPA-co-PyDP), and the polypyrrole-polyPyDPA bilayer.

A.2 Experimental

Materials and methods. 1-(N-pyrrolyl)-10-decanephosphonic acid was synthesized as outlined below. All reagents used for the synthesis were purchased from Aldrich Chemical Co: pyrrole (98%), 1,10-dibromodecane (95%), sodium hydride dry (95%), triethyl phosphite (98%), bromotrimethylsilane (97%), petroleum ether, diethylether, acetonitrile, acetone and dimethylformamide (DMF). Pyrrole (Pyr) was distilled under nitrogen; the other reagents and solvents were used without further purification. Tetrabutylammonium perchlorate (Alfa Aesar) was recrystallized from methanol. Potassium nitrate was recrystallized from boiling water. Tetrabutylammonium Iodide (Eastman) was recrystallized from 1:3 methanol/acetonitrile. Methylene chloride (MC) and benzonitrile were purchased from J.T. Baker and Eastman, respectively. Ferrocene (Fc/Fc^{+}) was purchased from Aldrich and sublimed at $1x10^{-3}$ mmHg and 70 $^{\circ}$C.

Synthesis of 1-pyrrolyl-10-decanephosphonic acid. PyDPA was synthesized from pyrrole by a slight modification of a recently published procedure [39]

Synthesis of 1-(10'-bromodecyl) pyrrole. A 250 ml two-necked flask fitted with a septum and a reflux condenser was charged with a solution of sodium hydride (1.8g; 75 mM) in 50 ml of anhydrous DMF. At 0 °C, a solution of pyrrole in 25 ml of DMF

(3.37g; 50 mM) was added dropwise and the mixture was stirred for 1 hour followed by the dropwise addition of a solution of $Br(CH_2)_{10}Br$ (37.5g; 125 mM) in 50 ml of anhydrous DMF at this temperature. The mixture was then stirred for 3 hours at room temperature. After that, 10 ml of water was added and the mixture was stirred for 30 minutes. Then, 50 ml of diethyl ether was added to the mixture which was washed three times with 50 ml of aqueous citric acid solution (3M) and with 50 ml of water. The organic phase was dried over $MgSO_4$, filtered and the solvent was evaporated under reduced pressure. The crude product was purified by column chromatography (silica gel; eluent petroleum ether/diethyl ether; (9/1); (v/v)) to give 4.98 g (71 %) of the title Pyr-$(CH_2)_{10}$-Br **1** as a yellowish liquid. ^{1}H NMR ($CDCl_3$, 400 MHz, δ, ppm from TMS): 1.2-1.6 (m, 16H, Pyr-$CH_2(\underline{CH_2})_8$-CH_2-Br); 3.4 (t, 2H, $\underline{CH_2}$Br; J = 6.93 Hz); 3.9 (t, 2H, $\underline{CH_2}$-Pyr; J = 7.26 Hz); 6.1 (t, 2H, $\underline{CH}N\underline{CH}$, J = 1.98 Hz); 6.6 (t, 2H, $\underline{HC}CHNCH\underline{CH}$; J = 2.20 Hz)).

Synthesis of phosphonate ester. A 250 ml two-necked flask fitted with a septum and a reflux condenser was charged with a solution of 1-pyrrole-10-bromo-undecane (4.98g ; 17.7 mmol) and triethyl phosphite (29.41g ; 0.17mol). The mixture was stirred at 165 °C for 15 hours. The excess of triethyl phosphite was removed by vacuum distillation (30-35 °C at $4x10^{-2}$ mmHg). The 10-(1H-pyroll-1-yl)decyl-1-diethylphosphonate ester was obtained in pure state in 97 % yield (5.93g) as a yellowish liquid. ^{1}H NMR ($CDCl_3$, 400 MHz, δ, ppm from TMS): 1.2-1.6 (m, 16H, Pyr-$CH_2(\underline{CH_2})_8$-CH_2-Br); 1.6-1.9 (m, 8H, $\underline{CH_2}$-P and P-(OCH_2-$\underline{CH_3}$)); 3.9 (t, 2H, $\underline{CH_2}$-Pyr; J = 7.26 Hz); 4.1 (m, 4H, P-($O\underline{CH_2}$-CH_3); 6.1 (t, 2H, $\underline{CH}N\underline{CH}$, J = 1.98 Hz); 6.6 (t, 2H, $\underline{HC}CHNCH\underline{CH}$; J = 2.20 Hz)). ^{32}P NMR (400 MHz): δ(ppm): 39 (s, 1P, CH_2-$\underline{P}$).

Synthesis of phosphonic acid. To a dry 100ml two-necked flask fitted with a septum and a reflux condenser was added 5.93g (17.1mmol) of phosphonate ester followed by the dropwise addition of bromotrimethylsilane (7.85g, 51.5mmol). The mixture was stirred at room temperature for 2 hours. Then, 10 ml of a mixture of acetone/water (2/1, v/v) was added and the mixture was stirred during 1 hour. The excess of reagent was removed under reduced pressure and the crude product was freed from water by azeotropic distillation using acetonitrile. The target phosphonic acid was obtained in pure state in 59% yield as a white solid (2.89g) after crystallisation from a mixture of ether and pentane. m.p. 65 °C. ^{1}H NMR ($CDCl_3$, 400 MHz, δ, ppm from TMS): 1.2-1.7 (m, 16H, Pyr-CH_2($\underline{CH_2}$)$_8$-CH_2-Br); 1.7-1.9 (m, 2H, $\underline{CH_2}$-P); 3.9 (t, 2H, $\underline{CH_2}$-Pyr; J = 7.26 Hz); 6.1 (t, 2H, $\underline{CH}N\underline{CH}$, J = 1.98 Hz); 6.6 (t, 2H, $\underline{HC}CHNCH\underline{CH}$; J = 2.20 Hz)). IR (KBr pellet, cm^{-1}): 3500-2500 (broad), 2925, 2853, 1502, 1466, 1403, 1283, 1229, 1087, 997, 952, 790, 723, 609, 529. ^{32}P NMR (400 MHz): δ(ppm): 33 (s, 1P, CH_2-$\underline{P}$). MS (Chemical ionisation, CI): 288 (M+1), 270, 237, 151, 133, 105, 79, 77.

Electrochemical experiments. All electrochemical measurements were performed on CH 660 or CH401 workstations in a standard three-electrode cell. The working electrode was a platinum disc electrode of A = 0.02 cm^2 (Bioanalytical Systems, inc.) or platinum microelectrode of A = 4.9x10^{-6} cm^2 (fabricated in-house), chemically cleaned with piranha solution (must be handled with care and not stored in closed container) and cycled in 1 M H_2SO_4 before use. Platinum foil of A = 1 cm^2 was used as the counter electrode. The reference electrode used in methylene chloride was Ag/AgI in MC with 0.1 M TBAI || 0.1 M TBAP in MC (-0.95 V versus Fc/Fc^+). The reference electrode used in aqueous solutions was Ag/AgCl in 1 M KCl aq. || 0.1 M KNO_3 aq.

Electropolymerization. Films were deposited under potentiodynamic and potentiostatic control from 2.5 mM PyDPA in 0.1 M TBAP in CH_2Cl_2. After polymerization, the film was rinsed with copious amounts of CH_2Cl_2 in order to remove excess monomer, oligomers, and electrolyte.

Scanning Electron Microscopy. Scanning electron microscopy was used to examine the surface morphology of films deposited on gold substrates. All measurements were performed with a Zeiss SEM Ultra60 (Carl Zeiss SMT AG, Germany).

Fourier Transform Infrared Spectroscopy. The compositions of the deposited films on Pt disc electrodes were analyzed with Fourier Transform Infrared Spectroscopy (FTIR). Measurements were made in reflectance mode using a Biorad FTS-6000 Fourier transform infrared (FTIR) spectrometer attached to a UMA-500 infrared microscope.

Electrochemical Characterization. Films were cycled in 2.5 mM hexaammineruthenium(III) chloride ($Ru(NH_3)_4^{2+}$/ $Ru(NH_3)_4^{3+}$) and 2.5 mM potassium ferricyanide(III) ($Fe(CN)_6^{3-}$/ $Fe(CN)_6^{2-}$) in 1 M KCl in order to determine the redox activity of the films.

Profilometry measurements. Films deposited on platinum-plated quartz crystals were characterized by profilometry using a Dektak^{3}ST surface profiler (Sloan).

Electrochemical Quartz Crystal Microbalance. Depositions were carried out on platinum-coated 10 MHz crystals (electrode area, A = 0.204 cm^2) using a CH401 workstation. Films were rinsed and dried under vacuum for 24 hours before the frequencies were measured on a PLO-10i Phase Lock Oscillator (Maxtek, inc.). Mass (Δm in ng) was calculated from Δf (Hz) using the relationship [40]:

$$\Delta m = 0.223/(\Delta f \times A) \qquad (42)$$

Where A is the area of the electrode.

A.3 Results and Discussion

The electropolymerization of PyDPA has been successfully carried out from methylene chloride containing 0.1 M tetrabutylammonium perchlorate (TBAP) under potentiostatic and potentiodynamic conditions. Figure 31 shows the polymerization in the potential window 0.65 V – 1.7 V. Oxidation of the monomer occurs at 1.65 V. Repeated cycling up to 25 cycles results in deposition of a conducting polymer film with broad oxidation and reduction waves between 1.0 V – 1.4 V (figure 31a). The current densities of all three processes, *i.e.* monomer oxidation, polymer reduction, and polymer oxidation, increase with each cycle indicating the growth of a conducting polymer. Furthermore, the entire cyclic voltammogram shifts positive by around 100 mV resulting from an increased resistivity of the film. The same trend has been reported during the electropolymerization of 3-((ω-bromododecyloxy)methyl)thiophene and the authors attributed the shift to disruption of planarity by the long alkyl side-chain [41]. The alkyl chains in polyPyDPA are expected to cause similar disruption of conjugation and increase of resistivity. The polymerization of polyPD undergoes the same shift. This result enforces the hypothesis that the cause of the shift is the bulkiness of the alkyl chains and not the phosphonate group (data not shown).

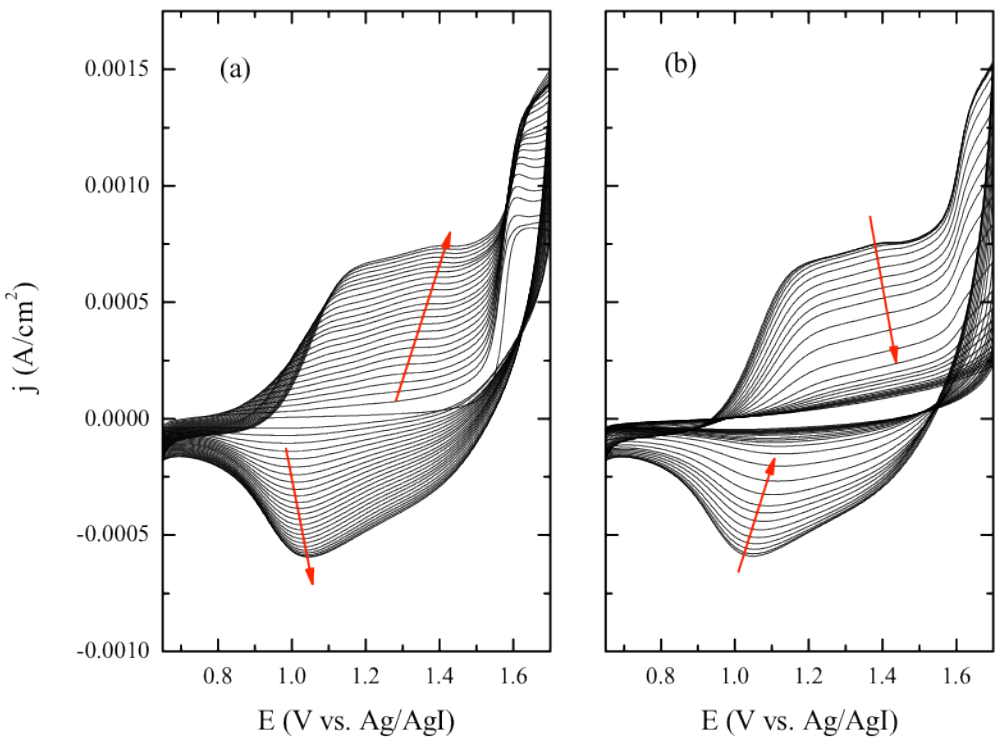

Figure 31: Potentiodynamic polymerization of PyDPA part 1

The continued potentiodynamic polymerization beyond 25 cycles results in a gradual decrease in current densities corresponding to a decrease in conductivity (figure 31b). The exact number of cycles before this growth-to-passivation transition is dependent on anodic switching potential, monomer concentration, and the age of the deposition solution. The age of the solution and monomer concentration were kept constant; for all polymerizations carried out in this study the monomer concentration was 2.5 mM and fresh solutions were used. In general, the passivation was found to occur sooner for higher anodic switching potentials up to 1.8 V. Beyond 1.8 V the passivation is immediate and characterized by a much larger monomer oxidation peak similar to what is observed during overoxidation of polypyrrole. Interestingly, electropolymerization of

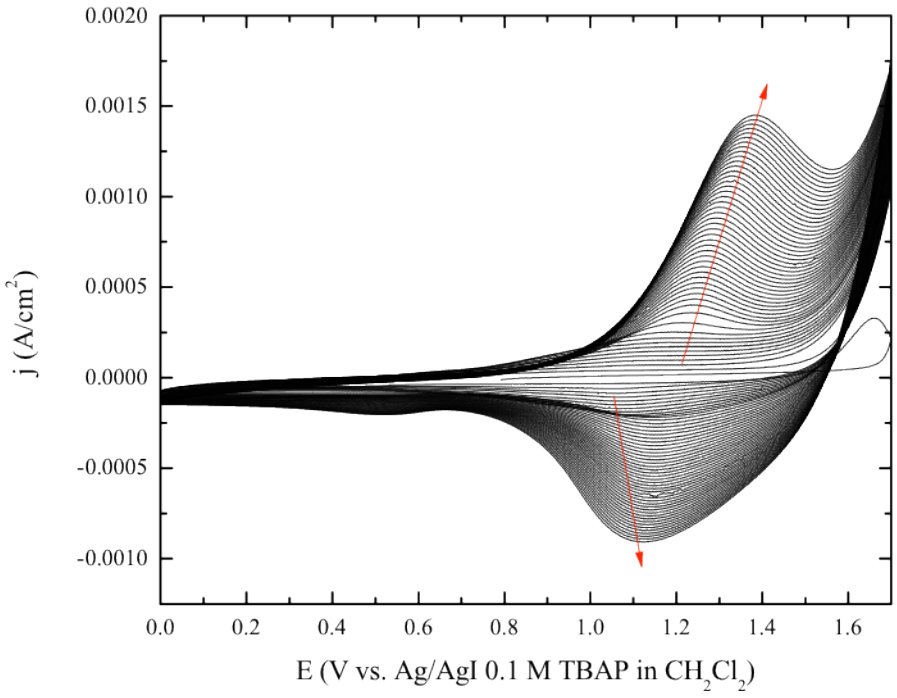

Figure 32: Potentiodynamic polymerization of PyDP

polyPyDP does not undergo the same transition unless very high potentials are applied, *i.e.* the film is overoxidized (figure 32). This suggests that the phosphonate groups may play a role in the growth-to-passivation transition.

Similar trends are observed during the potentiodynamic deposition of PyDPA in the potential window 0.0 V – 1.7 V (figure 33) with the exception of an additional reduction peak at ca. 0.4 V. This peak shifts to lower potentials with each cycle. No corresponding oxidation peak is observed indicating either an irreversible electrochemical process or a reversible electrochemical process followed by an irreversible chemical process. A similar process has been observed in the electropolymerization of oligovinylthiophenes and is attributed to σ-bond formation in the film, *i.e.* cross-linking [42]. The cause of the reduction peak in the case of

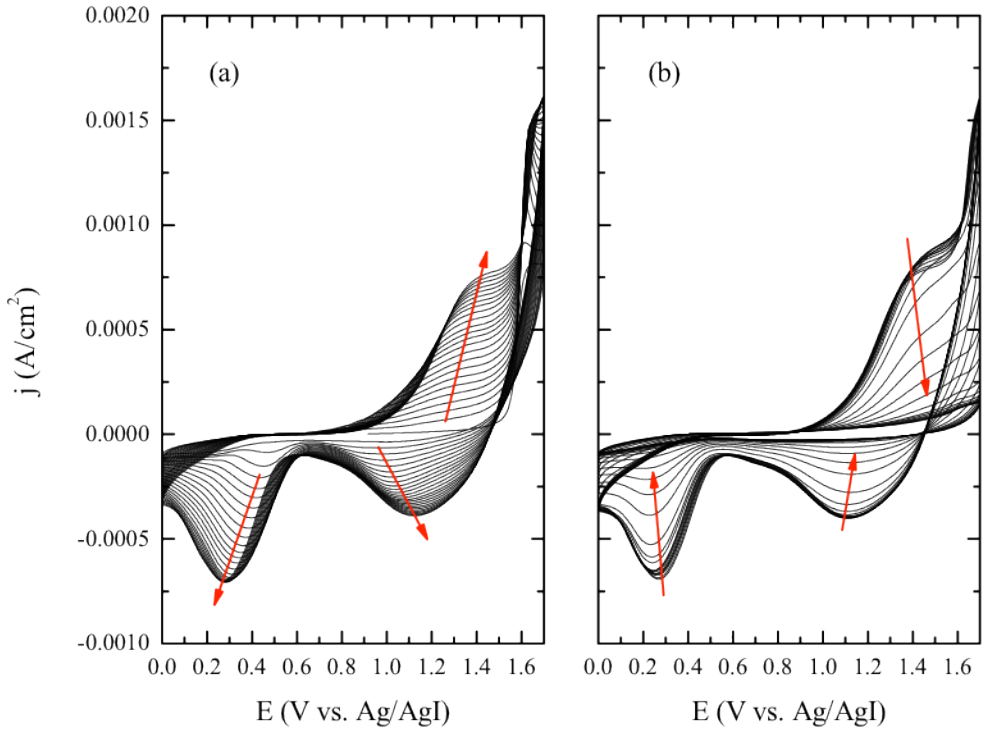

Figure 33: Potentiodynamic polymerization of PyDPA part 2

polyPyDPA is currently unknown. The peak is only observed after oxidation of the polymer at potentials of at least 1.6 V and the magnitude decreases with decreasing scan-rate indicating the reduction of long-lived intermediates formed during polymer and/or monomer oxidation. Accompanying this reduction is a change in shape of the polymer oxidation and reduction peaks (figure 34). In general, the peaks again shift to more positive potentials indicating increased resistivity of the polymer. Continued polymerization leads to the growth-to-passivation transition as already observed (figure 33b). The polymerization of PyDP in the same potential range (figure 32) shows only minor presence of the reduction process at low potentials. This finding suggests that the phosphonate groups may stabilize some intermediates formed during the oxidation of the monomer and/or polymer.

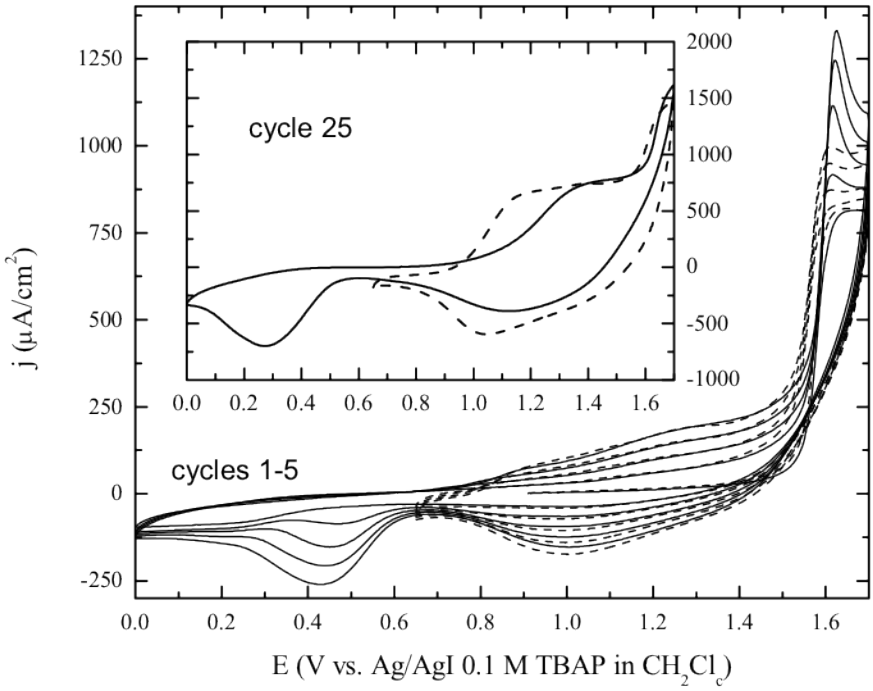

Figure 34: Comparison of polyPyDPA in two potential ranges

Cycling conducting polyPyDPA in background electrolyte (0.1 TBAP in CH_2Cl_2) after deposition results in the same characteristically broad redox wave seen during deposition (figure 35, red curve). The shape and intensity of the cyclic voltammogram is more or less the same as the shape observed in the last cycle during the polymerization. If cycled down to 0.0 V the reduction peak at *ca.* 400 mV appears smaller than on the last cycle of the deposition and sometimes does not appear at all. Upon continued cycling, this peak disappears resulting in minor changes in the shape of the polymer redox wave as discussed above. If the anodic switching potential is then increased to 1.8 V or greater a large current increase occurs near 1.8 V and the reduction peak at 400 mV appears intensified. Repeated cycling in this range leads quickly to electrode passivation (data not shown). As expected, insulating films showed no response in background electrolyte.

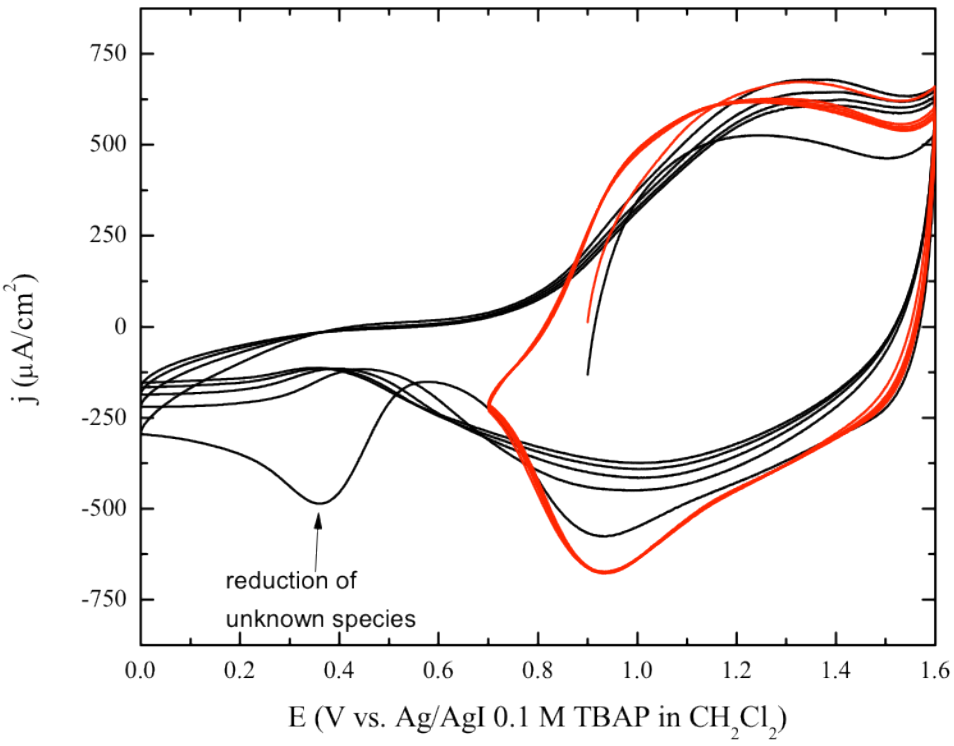

Figure 35: Behavior of polyPyDPA cycled in 0.1 M TBAP

Electronically insulating films (figure 36) and conducting films (figure 37), grown potentiodynamically in the potential range 0.65 — 1.7 V, were cycled in aqueous solutions containing either $Ru(NH_3)_6^{2+}$ / $Ru(NH_3)_6^{3+}$ or $Fe(CN)_6^{3-}$ / $Fe(CN)_6^{4-}$ in order to probe the permselectivity. The films showed no response to the negatively charged $Fe(CN)_6^{3-}$ / $Fe(CN)_6^{4-}$ while responding to the positively charged $Ru(NH_3)_6^{2+}$ / $Ru(NH_3)_6^{3+}$. The response to $Ru(NH_3)_6^{2+}$ / $Ru(NH_3)_6^{3+}$ for both conducting and insulating films suggests that at least some of the electron transfer is occurring at the platinum electrode. It is believed that the polymers behave as porous membranes with the pores lined by negatively charged phosphonate groups. The polyPyDP films showed no

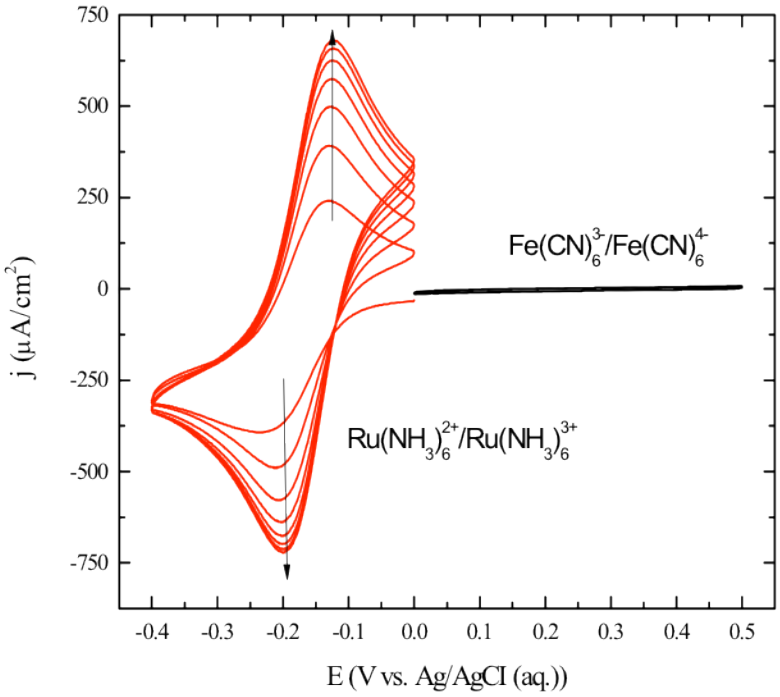

Figure 36: Permselectivity of insulating polyPyDPA

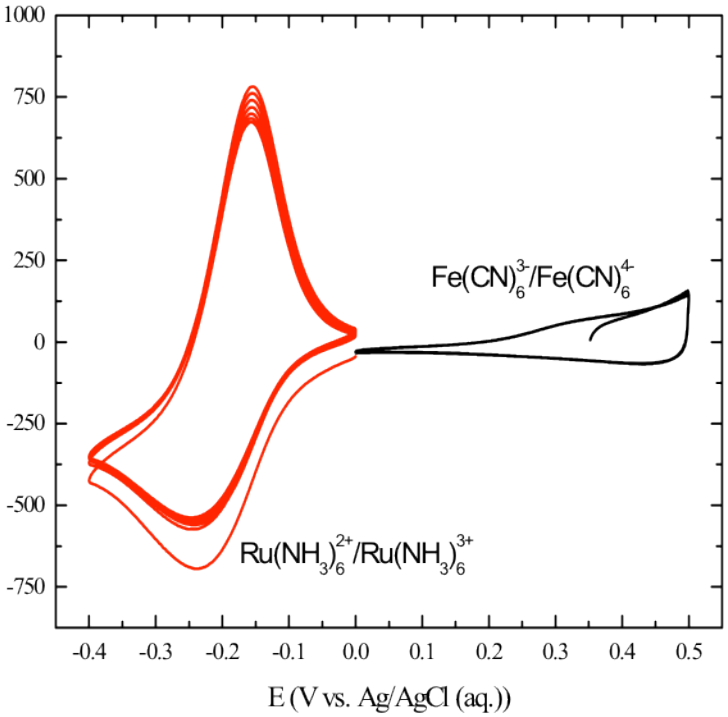

Figure 37: Permselectivity of conducting polyPyDPA

permeability to either redox couple. This is presumably due to the hydrophobic nature of the polymer.

A.4 Future Work

The polymerization of PyDPA has been demonstrated above. The presence of the phosphonate groups have been verified directly by FTIR (data not shown). The films should bind Mg^{2+} and therefore can be used as the second (outer) layer in the DNA hybridization sensor discussed in the introduction. Initial studies have verified the possibility of polymerizing polyPyDPA on top of a polypyrrole-coated electrode (figure 38). Interestingly, the reduction peak at *ca.* 400 mV observed for deposition on clean platinum electrodes is not observed. Further studies will attempt to determine the reason for this and hopefully the identity of the species being reduced. The effect the polymerization of polyPyDPA has on the polypyrrole conductivity and ion-exchange properties needs further study. Ideally, there should be little or no effect. The behavior of polypyrrole when cycled in methylene chloride needs to be fully characterized. Care must also be taken not to overoxidize the polypyrrole film when applying potentials necessary to oxidize the PyDPA monomer. Oxidation of PyDPA occurs only around 100 mV higher than the potentials applied to polymerize pyrrole (~750 mV vs. Ag/Ag^+ in 0.1 M $AgNO_3$). Applying this potential to polypyrrole should not and does not appear to damage the films.

Exposure of the polymer bilayer to $MgCl_2$ at pH 7 should lead to binding of Mg^{2+}. The presence of magnesium can be verified indirectly by monitoring the shift in phosphonate peaks by FTIR. A more direct and quantitative analysis is provided by X-ray

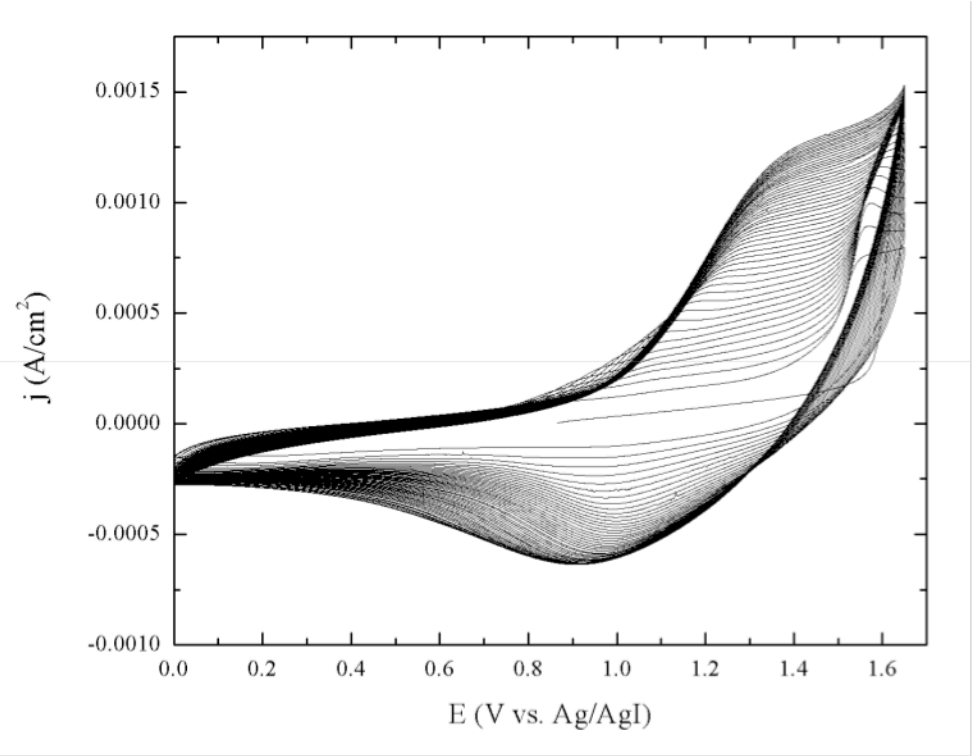

Figure 38: Polymerization of PyDPA on polypyrrole

photoelectron spectroscopy. Once verified, the magnesium-bearing bilayer can be exposed to the single-stranded DNA oligomers and the response after hybridization examined. The copolymerization of PyDPA and PyDP will be utilized as a means of controlling the density of phosphonate groups on the surface. If the density of phosphonate groups is too high then Mg^{2+} may be bound to two oxygens, leaving no positive charge for the attachment of DNA. If the density is too low there may not be enough coverage for the bound DNA to efficiently impede the ion flow.

Examination of figure 36 reveals a "loading" period during the first few cycles of the polymer in $Ru(NH_3)_6^{2+}$ / $Ru(NH_3)_6^{3+}$ as indicated by the arrows. This effect has been observed in the cycling of various polymer-coated electrodes with immobile negatively-charged groups in positively-charged redox couples, *e.g.* Nafion coated electrodes in

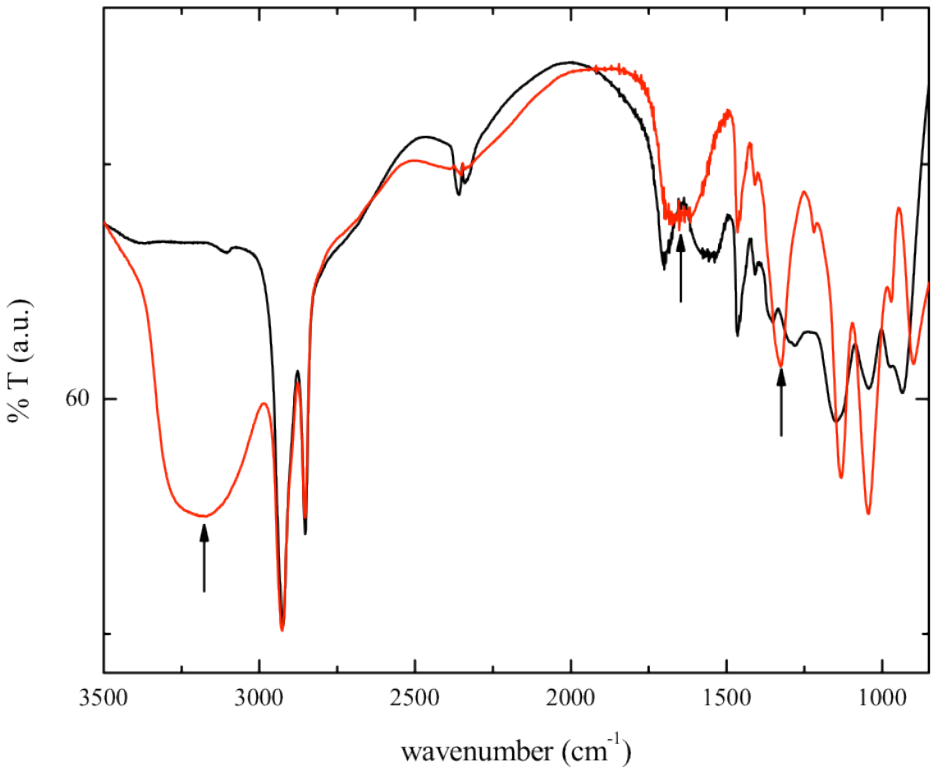

Figure 39: FTIR of polyPyDPA before/after exposure to $Ru(NH_3)_6^{2+}$/ $Ru(NH_3)_6^{3+}$

$[Os(bpy)_3]^{2+}$ [43]. This behavior indicates the interaction and immobilization of the redox couple with the charged groups. The FTIR spectra of polyPyDPA before and after cycling in 0.1 M KCl (aq.) containing 2.5 mM $Ru(NH_3)_6^{2+}$ / $Ru(NH_3)_6^{3+}$ are shown in figure 39. The presence of the broad peak around 3200 cm^{-1} is due to the N-H stretches in $Ru(NH_3)_6^{2+}$ / $Ru(NH_3)_6^{3+}$. The peaks corresponding to the phosphonate group at 1138 cm^{-1} and 943 cm^{-1} are shifted to lower energies. These shifts are due to interactions with the ruthenium complex. In order to test this hypothesis polyPyDPA film was cycled in 0.1 M KCl (aq.) after incorporation of the ruthenium complex (figure 40). If the redox couple was immobilized in the films and still redox active then the film would essentially behave like a redox polymer with electron transport facilitated by hopping from site to site.

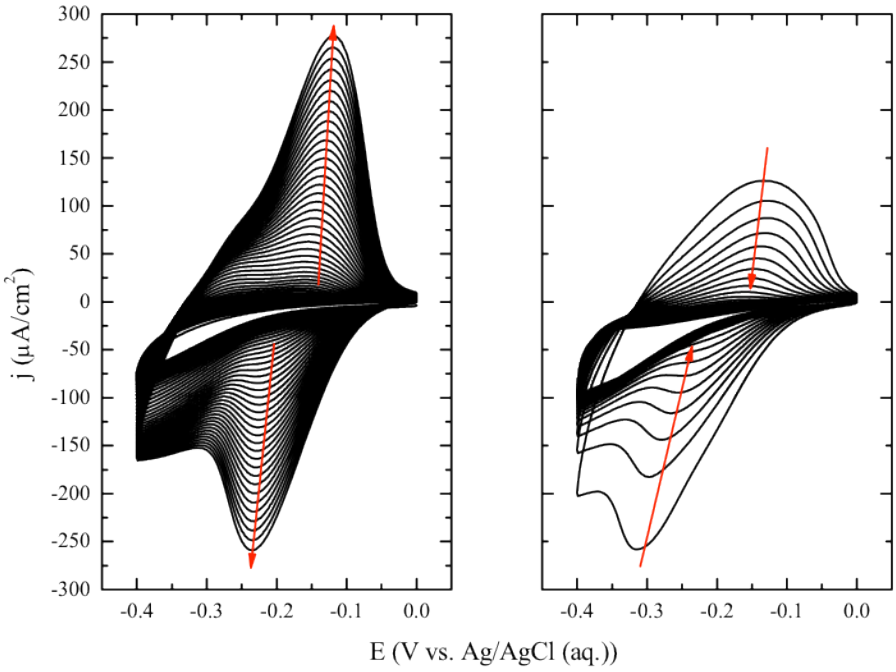

Figure 40: Incorporation of $Ru(NH_3)_6^{2+}$/ $Ru(NH_3)_6^{3+}$ by cycling

Unfortunately, the ruthenium slowly leaves the film upon cycling indicating the interactions are too weak to provide permanent immobilization and creation of a redox polymer.

The strength of the $Ru(NH_3)_6^{2+}$ / $Ru(NH_3)_6^{3+}$- phosphonate interaction appears to be too weak to result in permanent immobilization of the redox couple in the film. The ability to polymerize an electronically conducting or insulating film and then transform this film into a redox-active film would be of interest for two reasons: (1) for studying the general properties of polymers with both redox and intrinsic conductivity, (2) and the redox polymer may provide a more reproducible and stable substrate for the inner layer of the DNA hybridization sensor. Generally, the conductivity of a conducting polymer can be characterized based on the mechanism of charge transport within the film. In

intrinsically conducting polymers, such as polypyrrole, mobile charge carriers are formed upon oxidation, *i.e.* polarons and bipolarons. These charge carriers are really no more than mobile cations spread across multiple conjugated rings of the polymer backbone associated with a structural rearrangement. Charge movement is facilitated by movement of the polarons and/or bipolarons along the chains and hopping between chains. Redox polymers, on the other hand, contain a fixed number of immobile redox active sites and current is conducted solely via hopping between these sites. Polymers with both mobile polaron sites and immobile redox sites may show interesting electrochemical properties. Furthermore, the stability of redox polymers is not prone to the same oxidative deterioration as conducting polymers.

APPENDIX B

REVERSIBLE CHLORINE GAS SENSING WITH BUCKY GEL CHEMIRESISTOR

B.1 Introduction

Single-walled carbon nanotubes (SWCNTs) are effective selective layers for conductometric detection of various gases and organic vapors [44]. Unfortunately, SWCNTs display poor reversibility for many gases, including chlorine [45]. In these cases, recovery of the base resistance is only facilitated by heating or exposure to UV light. While these approaches to reversibility are feasible, they require additional electronics and power supply, which for some applications is not possible. A preferable way to achieve reversibility is through chemical modification of the SWCNTs or the addition of secondary components, particularly polymers [45-46].

Recently, it was found that SWCNTs form gels when grinded or sonicated in the presence of room temperature ionic liquids (RTILs) containing imidazolium cations [47]. These so-called "Bucky gels" are electronically conducting and have been studied for a variety of applications including actuators, coated electrodes, and conductive ink [48]. In this paper, we explore a Bucky gel composed of the RTIL [BMIM][BF_4] as the sensing layer of a chemiresistor. In particular, we examine its reversible and irreversible reaction with chlorine gas.

B.2 Experimental

The Bucky gels were made by grinding 13.5 mg [BMIM][BF_4] and 4.5 mg SWCNT with mortar and pestle for 45 minutes. The SWCNTs were 99% pure. The gel was then dispersed in 10 mL of DMF by sonication for 45 minutes. The SWCNT and SWCNT/IL films were cast from sonicated dispersions in DMF using a micropipette. The samples were annealed under vacuum at 80 °C to remove solvent.

Gas sensing measurements were carried out on a printed circuit board (PCB) chip containing 16 interdigitated electrodes (IDEs). The electrodes have a width of 80 μm and the gaps between electrodes are 115 μm. Gas dilutions were provided by an Environics 2040.

The compositions of the deposited films on Pt disc electrodes were analyzed with photoacoustic infrared spectroscopy (PAS). Measurements were made using a Biorad FTS-6000 Fourier transform infrared (FTIR) spectrometer with a MTEC photoacoustic attachment (model 300). Microscope images were obtained using an Olympus BX30 optical microscope with Olympus DP25 microscope camera.

B.3 Results and Discussion

Optical micrographs of pure SWCNTs and the Bucky gel produced by grinding [BMIM][BF_4] and SWCNTs are shown in figure 41. Both films were cast on a glass slide from dispersions in DMF. An increase in surface area and porosity is clearly visible in the Bucky gel compared with the matted appearance of the pure SWCNTs. This porosity should be advantageous for gas sensing applications, where diffusion into the bulk limits the response time and increased surface area contributes to better sensitivity.

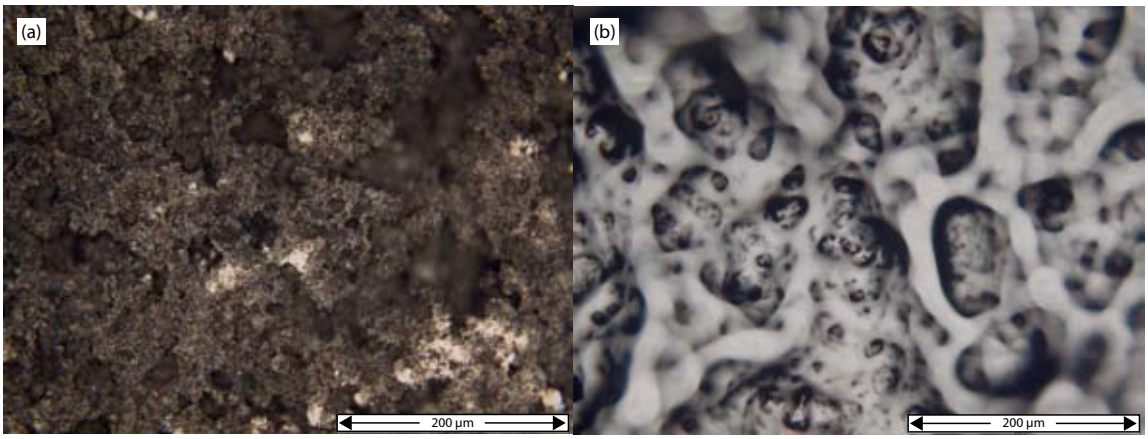

Figure 41: Optical micrographs of (a) SWCNT and (b) [BMIM][BF4] Bucky gel films

To test this hypothesis, the Bucky gel was cast on interdigitated electrodes and exposed 1, 3, and 5 ppm of chlorine gas (figure 42a). Chlorine gas was chosen because the poor (or lack of) reversibility of SWCNT-based chorine gas sensors at room temperature. Four films were cast to test the reproducibility. Figure 42 clearly shows the partial recovery of the base resistance for all four sensors after exposure to air. No recovery is seen for the pure SWCNTs (figure 42b).

The exposure and recovery steps of each of the curves could be fit with a single exponential function ($R^2 \geq 0.99$). For the exposure steps, the time constant was found to be 182.78 s ± 47 .71 s. The recovery steps were slower with a time constant of 485.73 s ± 45.33 s. The good exponential fit indicates that the response is kinetically controlled, at least at early times in the exposure/recovery steps. The tail of the response may not decay exponentially but from this data we were unable to confirm this. We speculate that a slower process dominates the tail.

A troubling feature of the response curves in figure 42 is the downward drift of the baseline resistance, which is partially responsible for the lack of full recovery. Drift

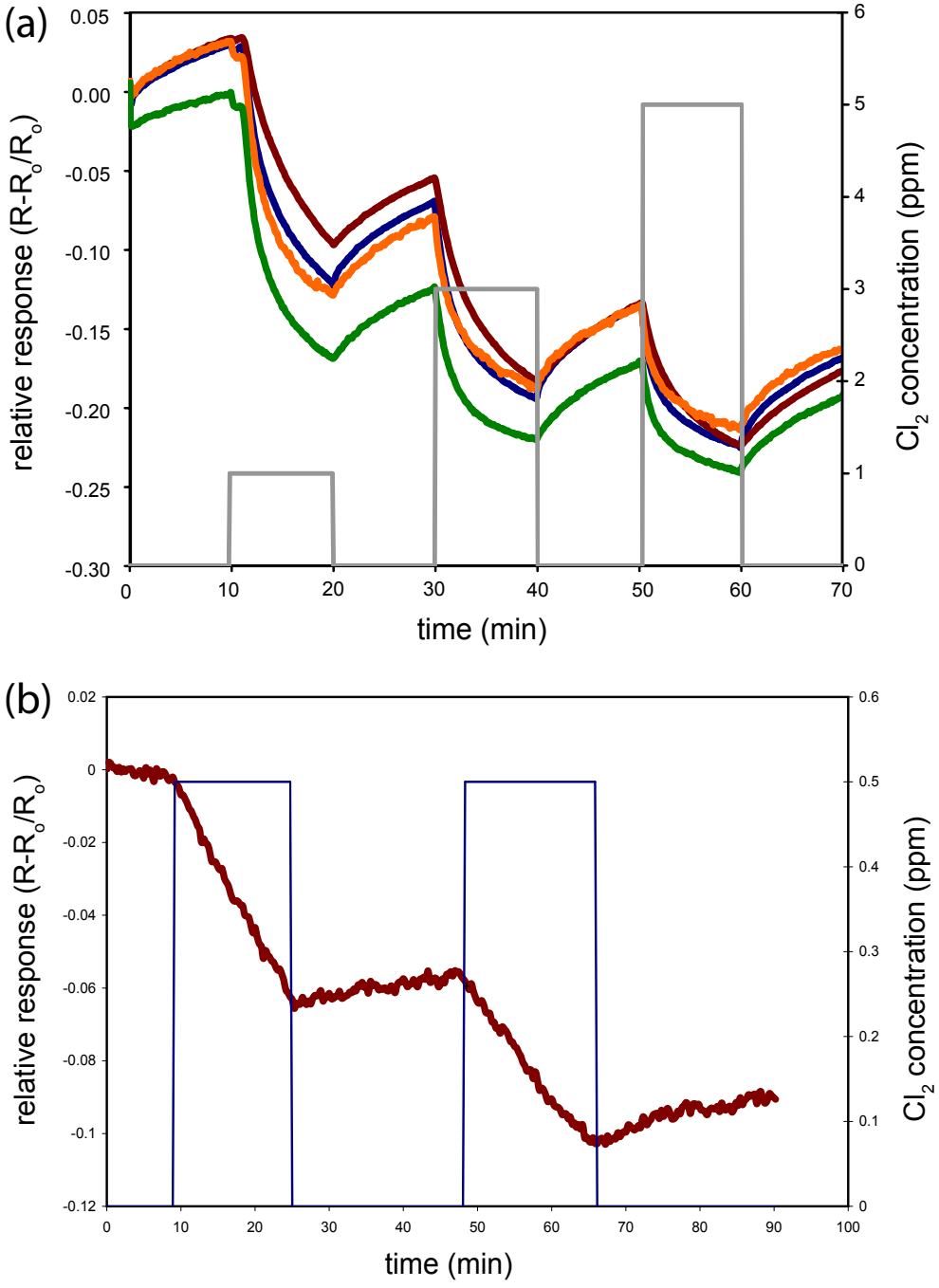

Figure 42: Response of (a) Bucky gel and (b) SWCNT chemiresistors to Cl_2

can severely hamper a sensor's applicability as a commercial device. Figure 43 shows typical response of the same sensors shown in figure 42, but exposed initially to 5 ppm of

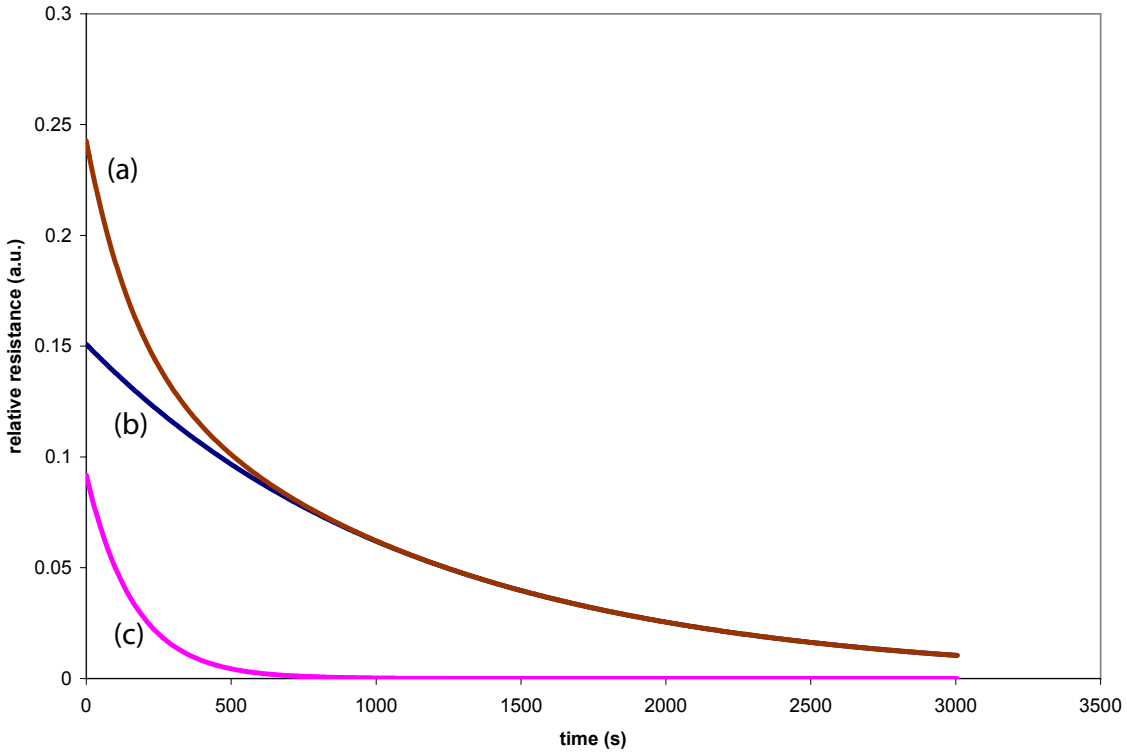

Figure 43: Response of Bucky gel chemiresistors to 5 ppm Cl_2 for 45 minutes showing the presence of two exponential processes

chlorine gas for 45 minutes. Note that the resistance still does not reach a limiting value after 45 minutes. This suggests the presence of a slow, possibly irreversible process competing with the reversible adsorption/desorption event. Indeed, this response curve cannot be fit satisfactorily with a single exponential decay. Instead two exponentials were used to fit the data. There is a fast process with a time constant of 164.543 s, which is comparable with the time constants found in figure 42. A second, slower exponential process with a time constant of 1124.026 s is responsible for the long-time drift. The responses in figure 49 could be fit with only one exponential because of the short exposure and purge times (only 10 minutes), whereas the slower process does not dominate the relaxation until after about 10 minutes as demonstrated in figure 43.

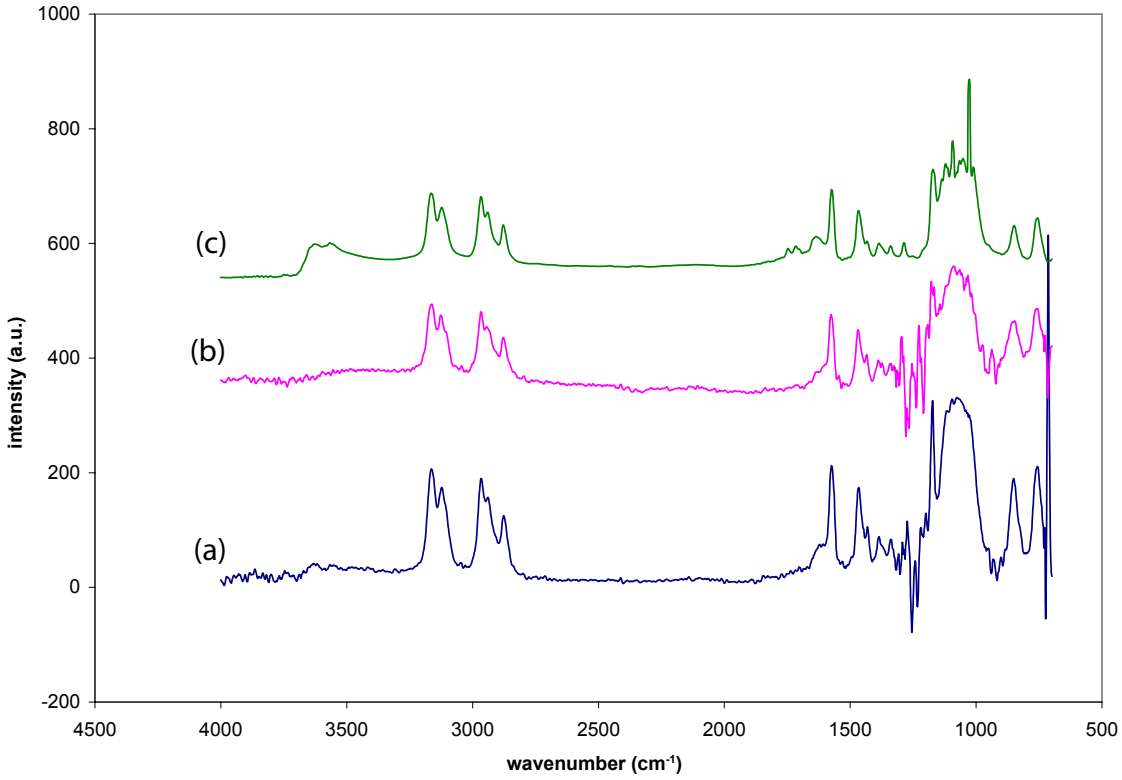

Figure 44: Figure 44: Photoacoustic spectroscopy (PAS) spectra of (a) pure [BMIM][BF_4], (b) Bucky gel before exposure to Cl_2 and (c) after gas exposure.

To investigate the origin of this process and the drift associated with it, FTIR spectra of the pure [BMIM][BF_4], and the Bucky gel before and after exposure to pure Cl_2 were measured (figure 44). The IR spectrum of pure SWCNTs was featureless and therefore not shown. It is also worth noting that the interaction of the IL with the SWCNT network does not alter the IR spectrum as seen in figure 51(a) and 51(b). Upon exposure to pure Cl_2 for 1 hour, two broad peaks around 3600 cm^{-1} and two sharper peaks around 1750 cm^{-1} appear. The latter peaks can be attributed to substitution of the hydrogens on the imidazolium rings with chlorine, resulting in HCl [49]. Further studies of the interaction of pure SWCNTs and Cl_2 as well as the interaction of pure [BMIM][BF_4]

and Cl_2 need to be performed to determine the origin of the peaks at ~3600 cm^{-1} and to determine whether or not this reaction is reversible.

B.4 Conclusions

We have demonstrated conductometric detection of chlorine gas with [BMIM][BF_4] "Bucky gel". The Bucky gel displays improved reversibility compared with the pure SWCNTs without adversely affecting the sensor response. In addition to the reversible adsorption and desorption of the gas molecules on the SWCNTs, the chlorine also undergoes a substitution reaction with the imidazolium cation of the RTIL. This relatively slow reaction results in a drifting base resistance if not allowed to go to completion. Pre-treatment of the RTIL to create a chlorine-substituted imidazolium cation may remove the baseline drift. Further studies are needed to confirm whether the sensor response would be adversely affected.

APPENDIX C

PORTABLE BETA SOLID STATE SCINTILLATION CALIBRATOR

The information contained in this appendix can be found in reference [50].

C.1 Introduction

In previous works, we have created custom novel radiation devices involving electrodeposited, beta-emitting Ni-63 (67 keV) [51]. Two of the critical devices that have been made are a microirradiator, which is a modified microelectrode deposited with Ni-63, and an ambient microionization device, involving Ni-63 custom electrodeposited onto a copper wire.

The main objective of these irradiators was to bring low activity levels (1-1000 Bq) of radiation into a laboratory safely, without the extensive regulatory procedures needed for safe deployment of open radiation sources over 100 mCi. In the field of radiobiology and other areas, there is a need for more such devices, but the majority of radioactive sources are limited to electron beams [52]. Additionally, live measurements are rare due to the fact that large radiation sources used in the field require extensive safety precautions. In most radiation research in radiobiological research utilizing large external sources the instantaneous radiation damage is difficult to visualize.

In vivo microirradiators were developed to bypass this need for large radiation flux and to focus the source onto a small (*e.g.* 25 μm) diameter probe, enabling the user

to have a device with low activity, while still providing a high flux (10^6 Bq/cm^2) to the biological sample, such as a cell [51b, 53].

For both of these devices, accurate measurements are required for determination of activity, flux, and dose rates as needed for the application. Typically, Ni-63 is only measured using a Liquid Scintillation Counter (LSC). LSC are very useful and accurate for compounds with low energy particles such as provided by Ni-63 [54]. Because they are expensive, they are usually shared. To increase accessibility for measurements of Ni-63 in a dry environment, here we report a novel, solid-state, bench-top instrument used for calibration of Ni-63 microirradiator activity.

C.2 Experimental

Working with radioactive materials requires proper adherence to safety guidelines set by the user's workplace. At Georgia Tech the applicable guidelines are Safety training for all radiological workers and daily surveys of workspace in which radiological materials have come into contact. Specific personal protective gear must be worn at all times as designated by the workplace.

The liquid scintillation cocktail (LS-275) was purchased from National Diagnostics, Inc. A standard luria broth (Tryptone 10 g/L, yeast extract 5 g/L, NaCl 10 g/L) was used in all cell culture medium experiments.

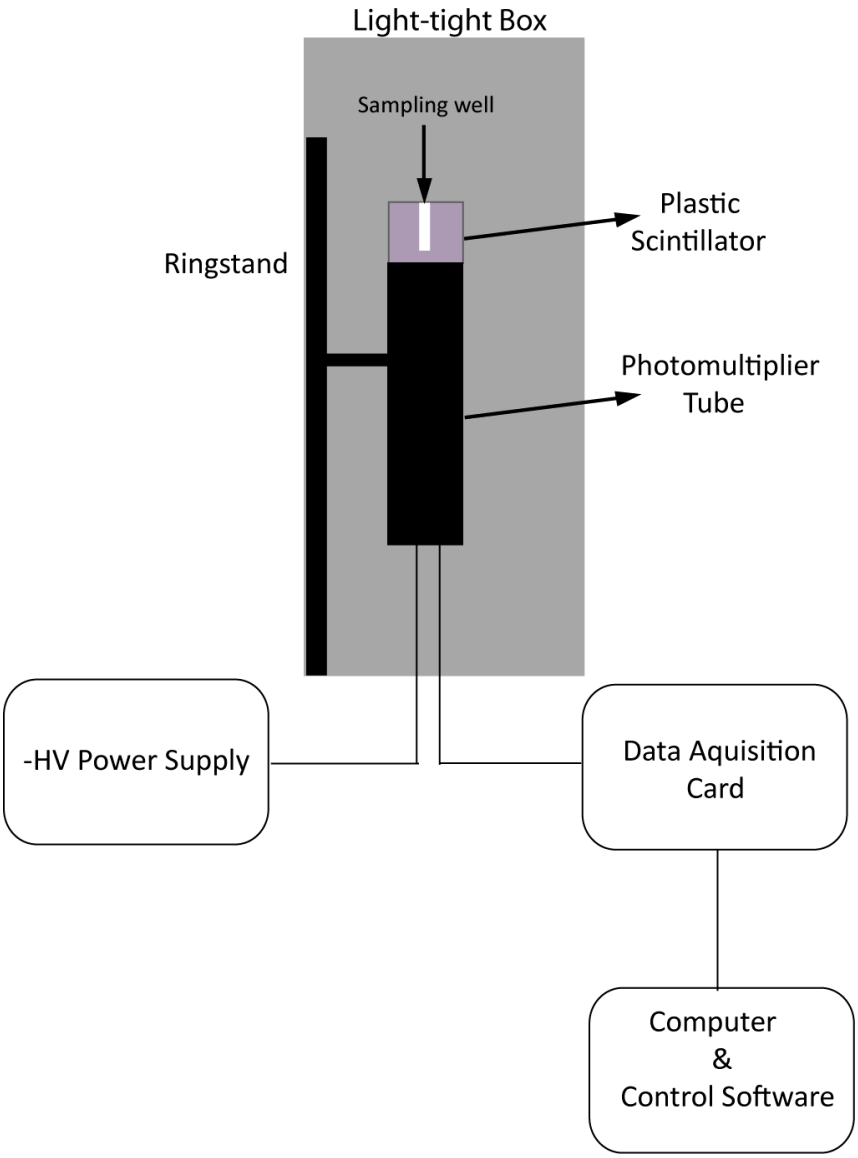

Figure 45: Schematic of calibrator, including external electronics

The calibrator consists of a power supply, a photomultiplier tube (PMT) with attached plastic scintillation, and data acquisition equipment (figure 45). A specialized PMT for plastic scintillation measurements, model H6410, was purchased from Hamamatsu Corporation. A Fluke 415B high voltage power supply was used in conjunction with the photomultiplier tube. A plastic scintillation crystal with a 2 in.

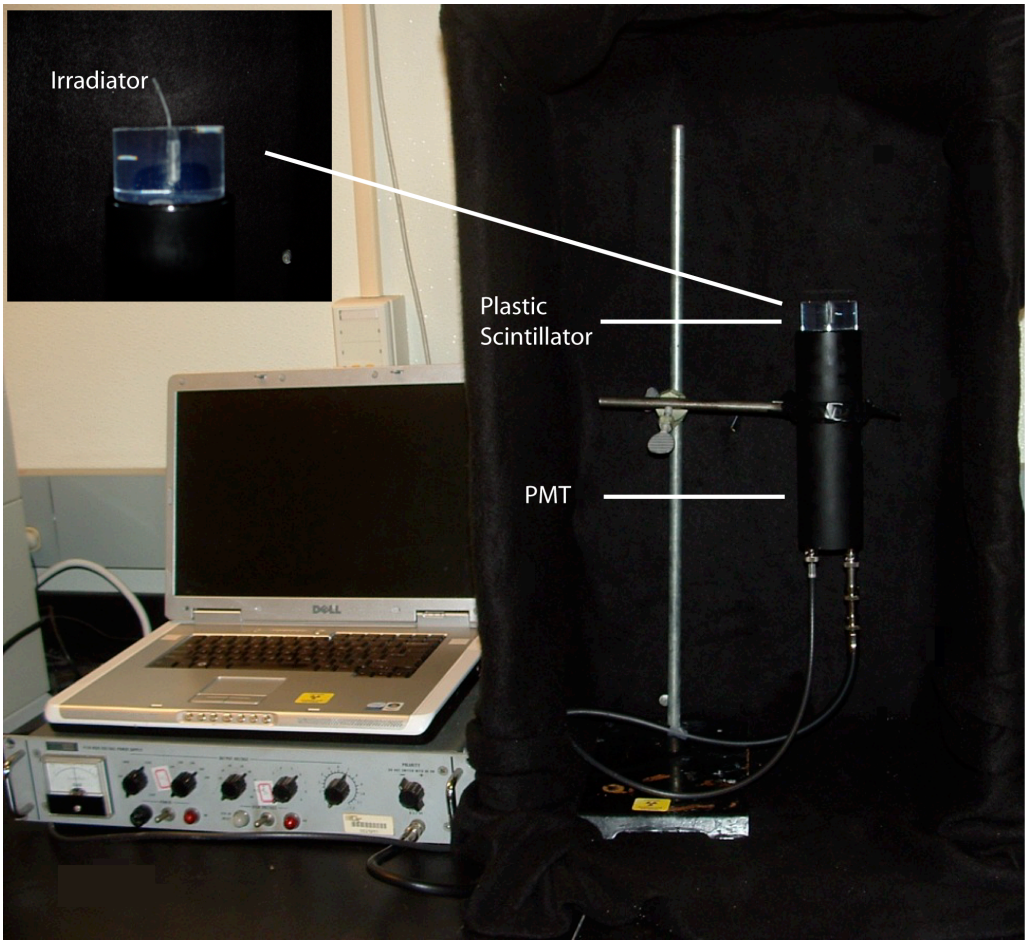

Figure 46: Photograph of the calibrator set-up

diameter and 1 in. height, EJ-212 (Eljen Technology, TX) was custom made to cover the entire window of the PMT (figure 46). A 1 mm diameter, 20 mm length hole was made in-house by hand drilling an opening into the center of the crystal for insertion of the microirradiator. It allowed for almost a "4π detection" of the beta particles emitted from the tool. To improve the light collection from the differing angles, indices of refraction of the glass of the PMT window and of the scintillation crystal were matched using silicone oil (Hach Company, CO) between the outer PMT window and the crystal. A shiny aluminum lined cup (not shown) was fitted over the scintillation crystal for additional

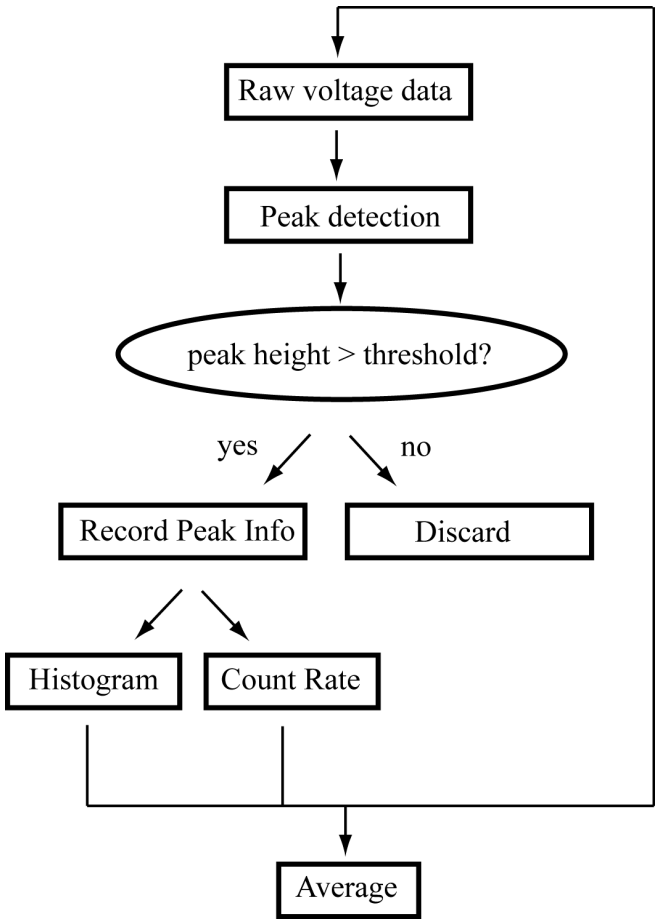

Figure 47: Data collection flow-chart

reflection and enhancement of light collection. Data acquisition devices and software will be discussed in more detail below. The photomultiplier tube was housed in a custom built light-tight box, with black felt lining the entire interior (figure 46). This enables the calibrator to be operated in a lit room without skewing data from inadvertent light interference.

Five microirradiators of varying activity and one copper wire based Ni-63 source were calibrated. Methods of fabrication and electrochemical deposition of Ni-63 onto these devices can be found elsewhere [51b]. For standardization, liquid scintillation measurements, performed on the LSC housed in the Office of Radiation Safety at the

Georgia Institute of Technology, were used to determine activity levels of each radioactive source. For the five individual microirradiators labeled 1-5, activity levels of 27, 85, 134, 59 and 58 Bq were measured, respectively. For the copper wire Ni-63 source, an activity of 3766 Bq was measured.

The voltage output from the PMT is amplified and digitized using a National Instruments USB-4431 dynamic signal acquisition module. The signal is DC-coupled in pseudo-differential mode and sampled at a rate of 100kS/s and a vertical resolution of 24-bit. The chassis of the USB-4431 is grounded to suppress electromagnetic interference. LabVIEW 8.5 code was written to obtain and process data from the USB-4431 (figure 47). For each measurement time, Δt, 100 kS/s $\times$ Δt data points are collected, and the peaks are identified by fitting a second order polynomial to the data points. Only peaks with heights greater than the selected threshold value are kept. The threshold value is determined before each experiment and is dependent upon the noise generated from the instrument. The number of peaks is then divided by Δt to give the photon count per second. Additionally, a histogram is created of the peak heights.

C.3 Results and Discussion.

To assess the accuracy and proper calibration of the setup, multiple trials were conducted at differing irradiation collection time lengths to determine accuracy and validity of counting statistics. Before each microirradiator was placed into the instrument, a background measurement of equal time length was recorded for each trial to ensure that the values were not skewed by fluctuating background. Two different times of dry

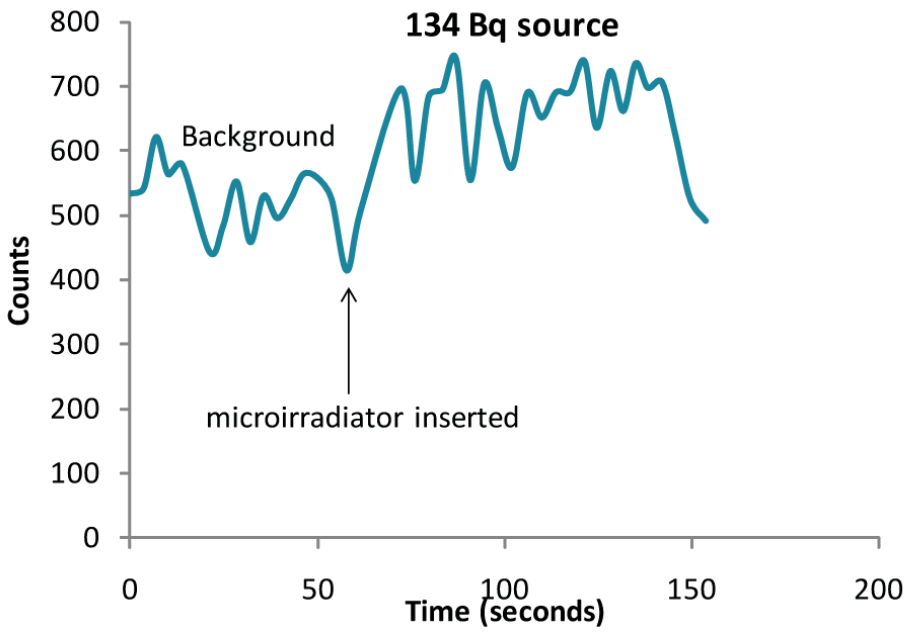

Figure 48: Time record of counts for one trial of microirradiator 1.

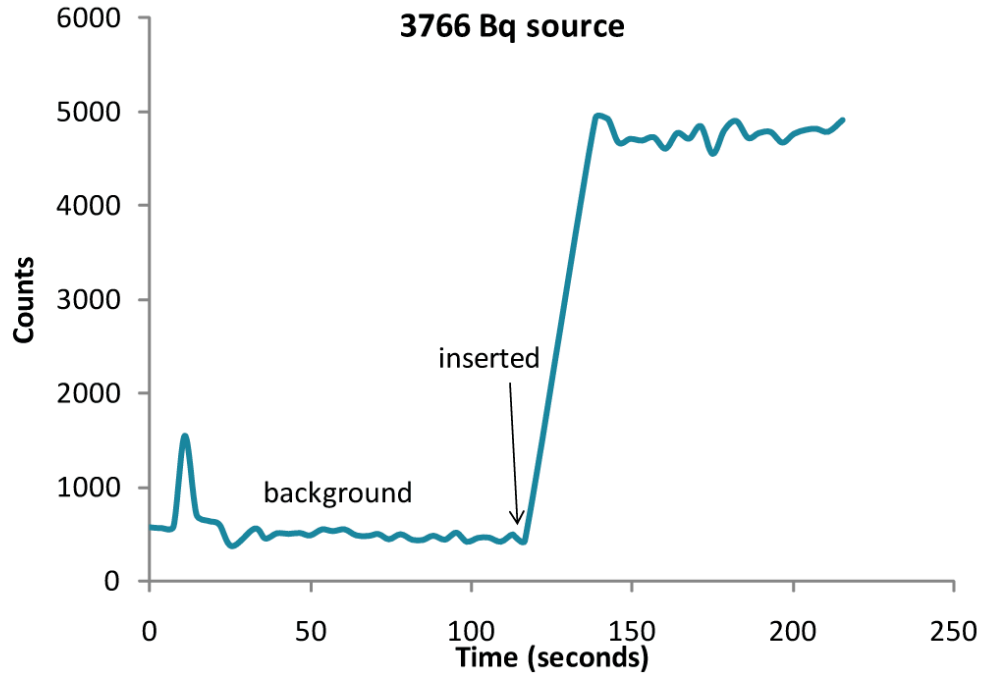

Figure 49: Time record of counts for one trial of a Ni-63 electroplated wire source.

scintillation measurements, approximately 100 and 600 seconds of background and direct measurement were taken for each of the sources (200 and 1200 seconds total). An example of the raw data produced from the background and irradiation measurements from a 134 Bq irradiator and 3766 Bq source are shown in figure 48 and 49, respectively. In figure 53a, the background is visibly fluctuating with an abrupt rise in count rate occurring immediately after insertion of the microirradiator into the calibrator. These fluctuations are caused by multiple factors, including cosmic radiation, natural random fluctuations of the source, and external electrical noise. With the larger source (figure 49), higher count rates are obtained due to the larger amounts of radioactivity. To determine total levels of activity, count rates are averaged for both the background and source. With the average background subtracted from the average irradiated value, an activity value is obtained for each trial.

Since radioactive decay is composed of randomized events with a binomial distribution, measurement time is critical in making an accurate determination of the true mean of the activity. The longer the measurement, the closer the experimental value, $\bar{x}_e$, approaches the true mean $\bar{x}$ [55]. Because of this, it is imperative to determine if the bench-top calibrator can provide accurate measurements within short and long time periods in comparison to liquid scintillation. To demonstrate, multiple trials of all sources mentioned above at both 100 and 600 seconds were conducted. After each trial's activity was recorded, a total average was taken for each source to determine the experimental mean. The experimental mean $\bar{x}_e$ within 95% confidence (+/- 1.96σ) for microirradiators 1 through 5 for the short measurements are 20.43 +/- 9.59, 36.29 +/- 9.10, 63.29 +/- 17.92, 33.60 +/- 13.04, and 43.0 +/- 3.98 Bq, respectively. For the plated Ni-63 source,

its value was determined to be 3821 +/- 127.88 Bq. For the 600 second intervals, the experimental mean $\bar{x}_e$ within 95% confidence for microirradiators 1 through 5 are 18.40 +/-10.88, 45.67 +/- 12.80, 71.83 +/- 34.00, 42.50 +/-14.81, and 46.60 +/- 17.28 Bq, respectively. The plated source measured 3731+/- 175.17 Bq.

When evaluating a radiation detection instrument, counting statistics are crucial in determination if the system is working correctly. One of the prime statistical measurements in evaluating the instrument is the "chi square test", defined as

$$X^2 = \frac{(N-1)s^2}{\bar{x}_e} \tag{43}$$

where N is the sample size, s is the sample variance, and $\bar{x}_e$ is the experimental mean. Since the sample variance should not differ greatly from the experimental mean, $s^2 / \bar{x}_e$ is a direct measurement of the sample variance deviating from the predicted variance. The amount to which X^2 deviates from (N-1) is a measurement of the departure from the predicted Poisson distributions [55]. To determine the probability, P, that each random sample fits a true Poisson distribution, the equation is defined as

$$P = \frac{\bar{x}^x e^{-x}}{x!} \tag{44}$$

where $\bar{x}$ is defined as the true mean and x the trial size. If P follows the Poisson distribution, $s^2 \approx \sigma^2$ and the assumption that $\bar{x} = \overline{x_e}$, values of P that are not too high (> .98) or low (< .02) are acceptable. Values of .98 and higher represent abnormally low fluctuations, where values of .02 and lower, represent abnormally large fluctuations. Taking into consideration the degrees of freedom (N-1) for each trial, all chi squared and subsequent probability values fell into acceptable ranges for this detection device for both the short and long measurements. It is interesting to note that statistically the probability

values for the longer measurements are moderately higher on a whole than the shorter measurements, indicating a smaller amount of fluctuations between measurements.

Statistics aside, the calibrator consistently measured lower values compared to the liquid scintillation counter. However, the plated Ni-63 source was well within 100 Bq of its LSC value. This result was anticipated due to the shape of the Ni-63 source within each microirradiator. The recessed disk microirradiator, before electrodeposition of Ni-63 has a recessed channel in glass, which is approximately 30 μm deep. With deposition of Ni-63 onto the electrode surface, the channel still has a depth of 20-29 microns. The glass effectively shields the radioactive source to about 70% of the total activity deposited [51b]. Within a liquid scintillation counter, it is plausible to assume that scintillation cocktail can seep into this channel, allowing passage of each photon through the glass of the microirradiator, whereas with plastic scintillation this would not be the case. However, the plated Ni-63 source was well within 100 Bq of its LSC value. Therefore, we speculate the lower results possibly due to the channel shielding interference with liquid scintillation cocktails.

C.5 Conclusions

We have successfully developed a Ni-63 bench-top solid-state calibrator for determination of activities of various custom-made sources. Using statistics, we have characterized and confirmed that measurements follow reasonably allowed fluctuations. In the future, other elements such as other low activity alpha and gamma emitting isotopes could be detected and evaluated using the same calibrator.

REFERENCES

[1] S. M. Sze, *Physics of Semiconductor Devices*, Wiley-Interscience, New York, **1981**, p.

[2] J. Janata, *Principles of Chemical Sensors*, Springer Science, New York, **2009**, p.

[3] D. R. Lide in *CRC Handbook of Chemistry and Physics*, *Vol.* CRC Press LLC, Washington D.C., **2000**.

[4] a) J. Park, D. Bang, K. Jang, S. Haam, J. Yang and S. Na, *Nanotechnology* **2012**, *23*; b) S. S. Pandey, S. C. K. Misra, B. D. Malhotra and S. Chandra, *Journal of Applied Polymer Science* **1992**, *44*, 911-915.

[5] K. D. O'Neil, B. Shaw and O. A. Semenikhin, *Journal of Physical Chemistry B* **2007**, *111*, 9253-9269.

[6] N. G. Van Kampen, *Stochastic Processes in Physics and Chemistry*, Elsevier Science Publishers, New York, **1981**, p.

[7] L. J. DeFelice, *Introduction to Membrane Noise*, Plenum Press, New York, **1981**, p.

[8] A. Bezegh and J. Janata, *Analytical Chemistry* **1987**, *59*, A494-&.

[9] a) A. Haemmerli, J. Janata and J. J. Brophy, *Journal of the Electrochemical Society* **1982**, *129*, 2306-2312; b) A. Bezegh and J. Janata, *Journal of the Electrochemical Society* **1986**, *133*, 2087-2092.

[10] J. L. Bredas and G. B. Street, *Accounts of Chemical Research* **1985**, *18*, 309-315.

[11] a) A. P. Kulkarni, C. J. Tonzola, A. Babel and S. A. Jenekhe, *Chemistry of Materials* **2004**, *16*, 4556-4573; b) S. Kola, J. Sinha and H. E. Katz, *Journal of Polymer Science Part B-Polymer Physics* **2012**, *50*, 1090-1120; c) A. Pron, P. Gawrys, M. Zagorska, D. Djurado and R. Demadrille, *Chemical Society Reviews* **2010**, *39*, 2577-2632; d) A. J. Heeger, *Chemical Society Reviews 39*, 2354-2371.

[12] a) J. Janata and M. Josowicz, *Journal of Solid State Electrochemistry* **2009**, *13*, 41-49; b) J. Janata and M. Josowicz, *Nature Materials* **2003**, *2*, 19-24; c) U. Lange, N. V. Roznyatouskaya and V. M. Mirsky, *Analytica Chimica Acta* **2008**, *614*, 1-26.

[13] T. F. Otero, J. G. Martinez and J. Arias-Pardilla, *Electrochimica Acta* **2012**, *84*, 112-128.

[14] P. M. McManus, R. J. Cushman and S. C. Yang, *Journal of Physical Chemistry* **1987**, *91*, 744-747.

[15] N. Tessler, Y. Preezant, N. Rappaport and Y. Roichman, *Advanced Materials* **2009**, *21*, 2741-2761.

[16] C. G. Wu and S. S. Chang, *Journal of Physical Chemistry B* **2005**, *109*, 825-832.

[17] Z. K. Li, J. M. Reijn and J. Janata, *Journal of the Electrochemical Society* **1985**, *132*, 563-566.

[18] M. Liess, D. Chinn, D. Petelenz and J. Janata, *Thin Solid Films* **1996**, *286*, 252-255.

[19] B. J. Polk, J. A. Smith, S. P. DeWeerth, Z. P. Zhou, J. Janata and K. Domansky, *Electroanalysis* **1999**, *11*, 707-711.

[20] S. Kogan, *Electronic Noise and Fluctuations in Solids*, Press Syndicate of the University of Cambridge, Cambridge, **1996**, p.

[21] R. B. Hallgren, *Solid-State Electronics* **1990**, *33*, 1071-1079.

[22] S. K. Sinha, *Introduction to Statistical Mechanics*, Alpha Science Internation Ltd., Oxford, **2005**, p.

[23] Chylewsk.C, *Angewandte Chemie-International Edition* **1971**, *10*, 195-&.

[24] A. B. Chwang and C. D. Frisbie, *Journal of Applied Physics* **2001**, *90*, 1342-1349.

[25] a) K. Potje-Kamloth, B. J. Polk, M. Josowicz and J. Janata, *Advanced Materials* **2001**, *13*, 1797-1800; b) K. Potje-Kamloth, B. J. Polk, M. Josowicz and J. Janata, *Chemistry of Materials* **2002**, *14*, 2782-2787.

[26] F. Zuo, M. Angelopoulos, A. G. Macdiarmid and A. J. Epstein, *Physical Review B* **1989**, *39*, 3570-3578.

[27] A. Papathanassiou, J. Grammatikakis, S. Sakkopoulos, E. Vitoratos and E. Dalas, *Journal of Physics and Chemistry of Solids* **2002**, *63*, 1771-1778.

[28] O. A. Semenikhin, *Annual Reports Section "C" (Physical Chemistry)* **2010**, *106*, 163-191.

[29] J. M. Ginder, A. F. Richter, A. G. Macdiarmid and A. J. Epstein, *Solid State Communications* **1987**, *63*, 97-101.

[30] a) S. S. Chang and C. G. Wu, *Journal of Physical Chemistry B* **2005**, *109*, 18275-18282; b) S. Y. Hong and S. M. Park, *Journal of Physical Chemistry B* **2005**, *109*, 9305-9310.

[31] S. T. Yau, J. N. Barisci and G. M. Spinks, *Applied Physics Letters* **1999**, *74*, 667-669.

[32] Z. Q. Li, G. M. Wang, N. Sai, D. Moses, M. C. Martin, M. Di Ventra, A. J. Heeger and D. N. Basov, *Nano Letters* **2006**, *6*, 224-228.

[33] J. Stejskal and R. G. Gilbert, *Pure and Applied Chemistry* **2002**, *74*, 857-867.

[34] W. V. G. Kortum, K. Andrussow, *Dissociation Constants of Organic Acids in Aqueous Solutions*, Butterworths, London, **1961**, p.

[35] C. D. S. Riccardi, C. Kranz, J. Kowalik, H. Yamanaka, B. Mizaikoff and M. Josowicz, *Analytical Chemistry* **2008**, *80*, 237-245.

[36] B. D. M. S. Freund, *Self-doped Conducting Polymers*, John Wiley & Sons Ltd, West Sussex, **2007**, p.

[37] a) M. Freund, L. Bodalbhai and A. Brajtertoth, *Talanta* **1991**, *38*, 95-99; b) Z. Q. Gao, M. X. Zi and B. S. Chen, *Journal of Electroanalytical Chemistry* **1994**, *373*, 141-148; c) C. C. Hsueh and A. Brajtertoth, *Analytical Chemistry* **1994**, *66*, 2458-2464; d) M. Sahin, Y. Sahin and A. Oezcan, *Sensors and Actuators B-Chemical* **2008**, *133*, 5-14; e) A. Witkowski and A. Brajtertoth, *Analytical Chemistry* **1992**, *64*, 635-641.

[38] R. West, M. Josowicz, J. Janata, I. Minet and L. Hevesi, *Journal of the Electrochemical Society* **2009**, *156*, F55-F59.

[39] S. Oberoi, E. Jahne, H. J. P. Adler and I. K. Varma, *Designed Monomers and Polymers* **2008**, *11*, 57-68.

[40] J. W. Grate, S. J. Martin and R. M. White, *Analytical Chemistry* **1993**, *65*, A940-A948.

[41] J. P. Soto, F. R. Diaz, M. A. del Valle, J. H. Velez and G. A. East, *Applied Surface Science* **2008**, *254*, 3489-3496.

[42] M. Pagels, J. Heinze, B. Geschke and V. Rang, *Electrochimica Acta* **2001**, *46*, 3943-3954.

[43] T. Tatsuma, M. Ozaki and N. Oyama, *Journal of Electroanalytical Chemistry* **1999**, *469*, 34-42.

[44] J. Li, Y. J. Lu, Q. Ye, M. Cinke, J. Han and M. Meyyappan, *Nano Letters* **2003**, *3*, 929-933.

[45] J. Li, Y. J. Lu and M. Meyyappan, *Ieee Sensors Journal* **2006**, *6*, 1047-1051.

[46] Y. J. Lu, C. Partridge, M. Meyyappan and J. Li, *Journal of Electroanalytical Chemistry* **2006**, *593*, 105-110.

[47] T. Fukushima, A. Kosaka, Y. Ishimura, T. Yamamoto, T. Takigawa, N. Ishii and T. Aida, *Science* **2003**, *300*, 2072-2074.

[48] J. Lee and T. Aida, *Chemical Communications 47*, 6757-6762.

[49] S.-W. Hu, Z.-X. Wang, F. Qu, T.-W. Chu and X.-Y. Wang, *The Journal of Physical Chemistry A 115*, 13452-13466.

[50] J. Steeb, R. West and J. Janata, *Radiochimica Acta 99*, 225-230.

[51] a) J. Steeb, A. S. Galhena, L. Nyadong, J. J. Facundo and M. Fernandez, *Chemical Communications* **2009**, 4699-4701; b) J. Steeb, M. Josowicz and J. Janata, *Analytical Chemistry* **2009**, *81*, 1976-1981.

[52] a) G. Randers-Pehrson, *Radiation Research* **2001**, *156*, 435-435; b) Z. W. Hu, L. J. Wu and Z. L. Yu, *Plasma Science & Technology* **2005**, *7*, 2789-2796.

[53] J. Summerour, Y. F. Chen, M. Josowicz, T. M. Orlando, J. Janata and A. Paulenova, *Radiation Physics and Chemistry* **2006**, *75*, 369-374.

[54] J. E. Martin, *Physics for Radiation Protection*, **2000**, p.

[55] G. F. Knoll, *Radiation Detection and Measurement*, John Wiley & Sons, Inc., **2000**, p.

VITA

Ryan M. West received his B.S. in Chemistry from the Georgia Institute of Technology in 2007. He is expected to receive his Ph.D. in Chemistry from the Georgia Institute of Technology in 2013. His graduate research is focused on measurement and analysis of polyaniline work function fluctuations.

PUBLICATIONS

Fluctuation Analysis of Organic Semiconductor – Insulator Interface R. West, M. Josowicz, J. Janata, PCCP, (accepted)

Fluctuation Analysis of Work Function of Organic Semiconductors R. West, C. Watts, M. Josowicz, J. Janata, Collection of Czechoslovak Chemical Communications, 76 (7), 843-858, 2012.

Portable Solid State Scintillation Calibrator for Beta Microirradiator J. Steeb, R. West, J. Janata, Radiochimica Acta, 99, 225-230, 2011.

Controlled Electropolymerization of 1-Pyrrolyl-10-decanephosphonic Acid: An Anion Barrier Layer R. West, M. Josowicz, J. Janata, I. Minet, L. Hevesi, Journal of the Electrochemical Society 156 (4) F55-F59 2009.

Electropolymerization of a Cation-Permeable Layer using 1-pyrrolyl-10-decanephosphonic Acid R. West, M. Josowicz, J. Janata, ECS Transactions San Francisco, CA Volume 19, 35 Years of Chemical Sensors, 2009.